PHD

Computer simulation studies of the metal-oxide support in automobile exhaust catalysis

Sayle, Thi Xuan Tran

Award date:
1993

Awarding institution:
University of Bath

Computer Simulation Studies of The Metal-Oxide Support in Automobile Exhaust Catalysis

Submitted by **Thi Xuan Tran Sayle** (*Lê Trân Xuân Thi*)
for the degree of PhD of the University of Bath
1993

Davy Faraday Laboratory
The Royal Institution of Great Britain

COPYRIGHT

ProQuest LLC
789 East Eisenhower Parkway
P.O. Box 1346
Ann Arbor, MI 48106-1346

ABSTRACT

The interactions between precious metal ions of palladium, platinum and rhodium with a secondary oxide, CeO_2 on an alumina support have been studied using atomistic simulation techniques. Existing potentials for ceria are compared and modified to provide a suitable model for this study, and a potential representing short range interactions between metal ions and the oxygens of ceria is derived. We show that the presence of noble metals modifies the ceria surfaces which may be correlated with the catalytic activity which is known to be enhanced as a consequence of the noble metal-ceria interactions (SMSI). Furthermore, we find that ceria is further modified when interfaced with an α-Al_2O_3 support as a direct result of the interface.

We examine pure ceria surfaces to identify active surfaces which provide an oxygen source for the oxidation of CO, which is an important reaction in removing toxic exhaust products. A new procedure (following Sayle 1992) has been developed to model routinely thin film interfaces between any two oxide materials with hexagonal symmetry. A study of defect formation of the interface has shown enhanced catalytic activity of ceria thin films.

ACKNOWLEDGEMENTS

I would like to thank my supervisors, Professor Richard Catlow and Dr. Stephen Parker for their help, advice, support and encouragement throughout the course of this work.

I would also like to thank Dr. Tim Truex and Mr. Alan Diwell for their helpful discussions.

I am grateful to Johnson Matthey Technology Centre for financial support, the Science and Engineering Council Research for the provision of computer time and Biosym technologies for the provision of the Insight II software.

I would like to acknowledge the help and contributions of all friends and colleagues from the Royal Institution and Bath University. I would like to thank Susan Hill for her friendship and advice, and Robin Grimes for his useful discussions.

Finally, a special acknowledgement to Dean Sayle, not only for the support, encouragement and understanding throughout my PhD. but also for the advice and proof reading of this thesis.

To

My Parents

CONTENTS

Chapter 3 Potential Models 40

CHAPTER 1

INTRODUCTION

1.1 Introduction

Catalytic processes are used in the modern chemical industry to limit the emission of polluting gases. Automobile exhaust catalysts are used to convert toxic polluting molecules emitted by internal combustion engines to harmless products. The main products of the combustion of gasoline (a mixture of hydrocarbons) are carbon dioxide and water which are non-toxic. However, the minority products including carbon monoxide, nitrogen oxides (NO, NO_2) are highly toxic and the uncombusted hydrocarbons are potential green house gases. One way to reduce these emissions is to use the three way catalytic converter to convert the three main classes of pollutants by the oxidation and reduction reactions summarised in table 1.1.

Table 1.1 Reactions in Automotive Exhaust Catalysts

CO	+	½ O_2	→	CO_2						(1)
Hydrocarbons	+	O_2	→	CO_2	+	H_2O				(2)
H_2	+	½ O_2	→	H_2O						(3)
CO	+	NO	→	½ N_2	+	CO_2				(4)
H_2	+	NO	→	½ N_2	+	H_2O				(5)
Hydrocarbons	+	NO	→	N_2	+	H_2O	+	CO_2		(6)
5/2 H_2	+	NO	→	NH_3	+	H_2O				(7)
CO	+	H_2O	→	CO_2	+	H_2				(8)
Hydrocarbons	+	H_2O	→	CO	+	CO_2	+	H_2		(9)

The three way catalyst is made of palladium, platinum and rhodium metals deposited on a ceramic support which is usually based on an alumina substrate with an additional oxide ceria. The role of ceria in catalytic activity enhancement is of crucial importance and is a major theme of the work described in this thesis.

1.2 Recent Developments

1.2.1 Experimental

The effect of ceria on the activity of a transition metal-ceria/alumina catalyst includes the promotion of the catalytic activity, the increase of the thermal stability of the support and the increase of the stabilisation of dispersed transition metals.

Ceria, when added to the alumina support, acts as an 'oxygen storage' component of the automobile catalyst due to its capacity to undergo a relatively rapid change in oxidation state upon changes in the redox potential of the exhaust gases. In the fuel rich condition, ceria promotes the oxidation activity by providing oxygen for carbon monoxide and hydrocarbon oxidation; and in the fuel lean condition, its reduced state removes oxygen from the gas phase to widen the air-fuel ratio thus promoting the conversion of nitrogen oxides; hence allowing the three major pollutants to be removed (Gandhi et al. 1976, Yao et al. 1977, Yao and Yu Yao 1984, Yao and Kummer 1987, and Shyu et al. 1988b). Ceria is also used to improve the dispersion of noble metals (Yao and Yu Yao 1984, Su et al. 1985, Su and Rosthschild 1986, Duplan and Praliaud 1991), and to stabilise the γ-Al_2O_3 oxide support (Harrison et al. 1988). The role of ceria in automobile exhaust catalysts is subject to the interaction between ceria and noble metals which is a function of the particular metal, ageing temperature and gaseous environment (Engler et al. 1989); the nature of which is proposed to be due to the formation metal-cerium alloy, in particular Pt_5Ce (Summers and Ausen 1979), the formation of anionic vacancies in ceria (Sanchez and Garquez 1987) and the reduction of cerium (Yao and Yu Yao 1984). Yao 1984 also showed that palladium, platinum and rhodium metals promote the reduction of Ce^{4+} to Ce^{3+} and thus facilitate the charge transfer from metal to cerium which results in the higher oxidation states of the metals, and hence increases the oxygen storage capacity of ceria.

The interaction between the metal atoms and the oxygen vacancies in reducible oxide supports has been proposed to be responsible for the strong surface metal-support interaction, SMSI (Sanchez and Gazquez 1987), in particular, the strong Pt-ceria interaction which may have a profound effect on the oxygen storage capacity of ceria. (Metcalf and Sundaresan 1986, Jin et al. 1987). The interaction of CeO_2 with noble metals greatly affects both the metal dispersion in alumina and the activity of the three way conversion catalyst (Summers and Ausen 1979).

The oxidation state of cerium in cerium based catalysts ($Ce/Pd/Al_2O_3$) has been investigated for both surface species by X-ray photoelectron spectroscopy (XPS) and in the bulk by X-ray absorption spectroscopy (XAS). Both techniques indicate that the reduction of ceria is more pronounced on the surface than in the bulk (Normand et al. 1988). The formation of lattice oxygen vacancies in ceria, which plays an important part in the oxidation of CO (Jin et al. 1987), is associated with the reduction of Ce (IV) to Ce (III). This may lead to the formation of a distinct Ce_2O_3 phase or in the presence of aluminium to cerium aluminate $CeAlO_3$ (Geller and Raccah 1970). The formation of the latter is catalysed by the oxidation of Pd to PdO (Shyu et al. 1988b and Hicks et al. 1990) and Pt to PtO (Shyu and Otto 1989).

Under moderate oxidising condition, the addition of ceria to a low loaded Rh/Al_2O_3 catalyst results in a modification of the kinetics of CO oxidation which is due to the suppression of CO inhibition effects (the negative first-order dependence of the reaction rate on CO concentration) and the decrease in the apparent activation energy for the CO oxidation reaction. The mechanism involves CO_2 formation and is via a surface three phase reaction, i.e. between adsorbed CO, Rh metal and lattice oxygen derived from the neighbouring ceria (Oh and Eickel 1988). Another mechanism such as the disproportionation reaction ($2CO \rightarrow C + CO_2$) has been demonstrated for the CO dissociation at room temperature which is activated by the partially reduced surface of CeO_2 by H_2 (Li et al. 1991). In addition to the enhancement of CO oxidation by Pd, Pt and Rh (Yu Yao 1984), by Pd (Shyu et al. 1988) and Pt (Summer and Ausen 1979); ceria was also found to influence strongly the reduction of NO by increasing the rate of NO dissociation and low temperature N_2 desorption which may be responsible for the CO-NO reaction kinetics, in particular the systems Rh/Al_2O_3 (Oh 1990) and Rh, Pt/Al_2O_3 (Lööf et al. 1991). The effects of ceria are associated with the interaction of highly dispersed metal with oxygen vacancies in the reduced ceria support. There is also evidence for oxygen migration from ceria to the precious metal Rh, this effect has been observed in a near room temperature study by Zafiris and Gorte (1993) who followed CO adsorption on Rh/CeO_2 by TPD. In the reduction of NO, Rh is believed to be partially oxidised and the dissociation of NO and N_2 desorption are modified.

Finally, we note that surface structures can be studied by the analysis of their LEED pattern which gives information about single and double steps present at the surface, while the intensity of the spectra gives information about bond lengths and angles. However, the interpretation of the data is often difficult, with multi-scattering being a major problem. Recently, very significant advances have been made to improve the analysis of LEED intensity spectra. These include the development of an automated tensor LEED program and developments towards direct inversion methods based on the principles of holograph to give three-dimensional structures (King 1993). Recent structural investigations include metal surface structures, adsorbate-induced restructuring (adsorption of CO, N on W). LEED has also been used by Cotter et al. (1988) to identify the arrangements of atoms of the overlaying material on the MgO substrate and XPS to quantify the coverage of the BaO overlayer. Experimental results such as these are valuable in ascertaining the interfacial structural configuration to enable comparisons to be made with the calculated interfacial structural configurations. On the other hand, simulation methods provide a powerful tool for studying the nature of the behaviour of defective materials at the atomic level, and at the same time they provide and predict information about favourable reactions between defects and metal oxides which sometime do not easily yield to conventional experimental studies. The next section gives a brief account of the lattice simulation study in relation to surfaces and interfaces together with some previous theoretical work on ceria.

1.2.2 Lattice Simulation

Over the last twenty years, computer simulation techniques have been extensively developed and continue to provide a powerful tool for studying the properties of a wide range of materials, especially at the atomic levels. Starting with the alkali halides, Boswarva and Lidiard (1967) showed that atomic simulation could be employed to study bulk lattice and defect properties. Now we can simulate both bulk and surface defect properties from simple structures to highly complex systems such as superconductors (Islam and Ananthamohan 1991). It is essential that simulation work reproduces the results available for known characterised systems, if we are to be confident of the predictions made from simulation work on systems or problems which have not been studied experimentally.

The modelling of surface properties of ceramic materials and the investigation of processes that occur at the surfaces and interfaces of ionic materials were undertaken first by Mackrodt and Stewart (1977), and Tasker (1979a). Another important development was the free energy minimisation technique for the calculations at elevated temperatures by Parker and Price (1988) which calculates solid state phase diagrams of minerals (Price et al. 1987). The inclusion of temperature effects in calculations later led, for example, to interesting observations on zeolites which are found to contract rather than expand on heating (Tschaufeser 1992).

Recently, modelling studies of the metal-metal oxide interface based on the image theory have been reported by Finnis (1991, 1992) and Duffy (1992). An alternative approach to investigate the electronic properties of the metal-metal oxide interface directly using local density approximation techniques have been described by Blochl et al. (1989), Freeman (1989), Schonberger et al. (1992). These techniques, which are still being developed and modified, will provide information about energies and bonding at the interfaces between metals and oxide materials which will be of great value in the study of many catalytic reactions.

Simulation work on cerium dioxide was first undertaken by Butler et al. (1983) who investigated the effects of the dopant ion radius on dopant-vacancy interactions in CeO_2. The results show that there is a strong dependence of the dopant-vacancy binding energies on the dopant radius, which is a general feature achieved in the ionic conductivity of various halides and oxide crystals. Later, Cormack et al. (1989) found that isolated Sc^{3+} substitutional ion in doped ceria is stabilised by the distortion of the surrounded cage of eight oxygen ions. Recently, the solution energy of Ce^{4+} in UO_{2-x} was studied in the stability of fission products in uranium-dioxide by Grimes and Catlow (1991).

The aims of this work are therefore first to understand the structure and properties of both bulk and surfaces of CeO_2, surface studies are, however, more important as they provide information directly related to catalytic reactions which normally take place on the surface. Next, we study the interaction between metal ions e.g. Rh^{3+}, Pd^{2+} and Pt^{2+} and oxygen vacancies both in the bulk and on the surfaces of the crystal; these defects are found (as described earlier) to improve activity of catalyst significantly. Processes such as migration and segregation of the defects will also be studied in order to investigate the mechanism of the enhancement of activity. The interaction between the pure and impurity containing surfaces of CeO_2 and small molecules is also considered for the case of CO oxidation and NO reduction. Finally, the work will be extended to study the interaction between ceria and alumina together with defect properties at the interface between the two materials. This will enable us to investigate the effect of the presence of an interface between two supported oxides on catalyst activity with special emphasis on the formation of interfacial oxygen vacancies.

CHAPTER 2

THEORETICAL METHODS

2.1 Introduction

In this chapter we describe the theoretical methods employed in the thesis to calculate the three dimensional bulk, two dimensional surface and interfacial energies. We also summarise in the appendix the crucial question of the procedure used in calculating the long range Coulomb summation.

2.2 Calculations of defect energies in the bulk of ionic crystal - CASCADE

The bulk defect calculations presented in this thesis are based on the Mott-Littleton method (Mott and Littleton 1938) developed originally by Lidiard and Norgett (1972) and implemented in the HADES (Harwell Automatic Defect Evaluation System) code (Norgett 1972, 1974) for cubic crystals. For the calculations in this work, its successor, the CASCADE (Cray Automatic System for the CAlculation of Defect Energies) code (Leslie 1982) was employed. In the latter program, the Mott-Littleton methodology has been generalised for systems of any symmetry (Catlow et al. 1982). The major problem associated with the calculation of the defect energy is the treatment of relaxation about the defect. This can be overcome by assuming that the relaxation is greatest in the immediate vicinity of the defect and then falls rapidly at distances away from the defect.

For the calculations of bulk defect energies, the crystal around the defect is divided into two regions: an inner region I centred on the defect, where all the ions around defect are allowed to relax explicitly; and an outer region II which is extended to infinity, and is treated by a quasi continuum approximation. Region

II is further subdivided into an inner region IIa and an outer region IIb (figure 2.1). The significance of which is discussed below. The total energy of the system E, can be written as:

$$\mathbf{E = E_1(x) + E_{1,2}(xy) + E_2(y)} \qquad (2.2.1)$$

Where $E_1(x)$: the energy of the inner region
$E_{1,2}(x,y)$: the interaction energy between regions I and II
$E_2(y)$: the energy of the outer region IIb
x : the independent coordinates of ion positions in region I
y : the ion displacements in region II

The energy of outer region, $E_2(y)$ cannot be calculated exactly because it contains an infinite number of displacements. We assume however that the distance between the defect and the innermost ions of region II is sufficiently large that we can describe the response of the outer region using the harmonic approximation for the ion displacements arising from the electric field generated by the defect. Therefore $E_2(y)$ can be represented by a quadratic function of y.

$$E_2\,(y) = \tfrac{1}{2}\,(y^T.A.y) \qquad (2.2.2)$$

where A is the force constant matrix and y^T is the displacement matrix. By substituting equation (2.2.2) to equation(2.2.1) and assuming ions in region II are in equilibrium positions, y' , i.e. the net forces acting on ions in region II is zero, then:

$$\left.\frac{\partial\, E_{1,2}\,(x\,,y)}{\partial y}\right|_{y\,=\,y'} + A.y \;=\; 0 \qquad (2.2.3)$$

Thus equation (2.1) becomes:

$$E \;=\; E_1\,(x) + E_{1,2}\,(x\,,y) - \frac{1}{2}\left.\frac{\partial\, E_{1,2}\,(x\,,y)}{\partial y}\right|_{y\,=\,y'} .\,y \qquad (2.2.4)$$

The total relaxed energy of the system, E, can be determined first by direct minimisation with respect to $\underline{x}$, (the displacements in region I), i.e. using the criterion $dE/d\underline{x} = 0$. This is possible in principle, but, it is difficult to apply in view of the complicated nature of the total energy E as a function of $\underline{x}$. An easier method is ensuring the <u>force</u> on each ion in region I is zero:

$$\left.\frac{\partial\, E}{\partial\, \underline{x}}\right|_{y\,=\,y'} \;=\; 0 \qquad (2.2.5)$$

We now calculate the energy of the defect by considering an explicit two-body representation for E, the energy of the **perfect** lattice;

$$E_L \;=\; \sum_{i>j} \Psi_{ij}\left(\left|\underline{R}_i - \underline{R}_j\right|\right) \qquad (2.2.6)$$

where Ψ_{ij} is a suitable pair potential (chapter 3) and $\underline{R}$ are the appropriate lattice coordinates. Similarly, the energy of the lattice containing the **defect** is given by;

$$E_D = \sum_{i>j} \Psi_{ij}\left(\left|\underline{r}_i - \underline{r}_j\right|\right) \tag{2.2.7}$$

where $\underline{r}$ are the displaced coordinates. The energy of the defect, therefore, is simply given as the difference in the lattice energy with and without the defect:

$$E = \sum_{i>j} \left[\Psi_{ij}\left(\left|\underline{r}_i - \underline{r}_j\right|\right) - \Psi_{ij}\left(\left|\underline{R}_i - \underline{R}_j\right|\right)\right] \tag{2.2.8}$$

As discussed by Catlow et al. (1982), the summation can be usefully rearranged to give the following:

$$\begin{aligned} E = & \sum_{\substack{i\in I\\ j\in I}} \left[\Psi_{ij}\left(\left|\underline{r}_i - \underline{r}_j\right|\right) - \Psi_{ij}\left(\left|\underline{R}_i - \underline{R}_j\right|\right)\right] + \sum_{\substack{i\in I\\ j\in II}} \left[\Psi_{ij}\left(\left|\underline{r}_i - \underline{r}_j\right|\right) - \Psi_{ij}\left(\left|\underline{R}_i - \underline{r}_j\right|\right)\right] \\ & - \frac{1}{2} \sum_{\substack{i\in II\\ j\in II}} \left[\frac{\partial}{\partial \underline{r}_j}\Psi_{ij}\left(\left|\underline{r}_i - \underline{r}_j\right|\right) - \frac{\partial}{\partial \underline{r}_j}\Psi_{ij}\left(\left|\underline{R}_i - \underline{r}_j\right|\right)\right] . \left(\underline{r}_j - \underline{R}_j\right) \end{aligned} \tag{2.2.9}$$

where the three terms can be identified with E_1, E_{12} and E_2 respectively.

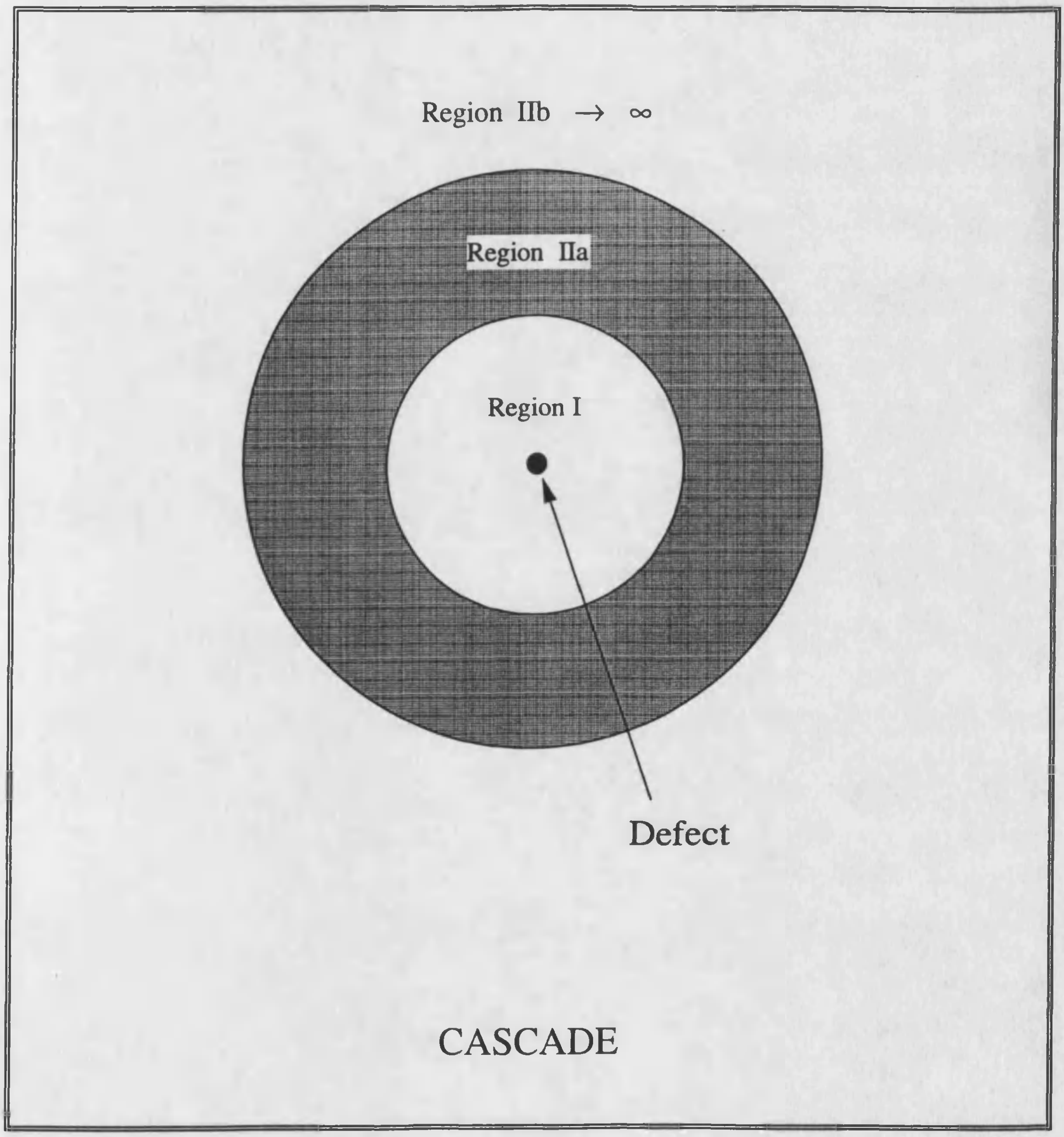

Figure 2.1 Two regions strategy used for the calculations of defects in the bulk of the crystal - CASCADE

2.2.1 Mott-Littleton approximation

The interactions in region I are purely local and are treated explicitly for the ionic crystal. In the neighbourhood of region I (i.e. in region IIa), the interactions between region I and region II comprise both short range and long range terms which can be calculated by direct summation. Away from the region I, region IIb is treated so that the displacement/interaction is due entirely to the Coulombic field of the defect. The treatment of this long range region I-region IIb interaction has been developed from the classical polarisation theory of Mott and Littleton (1938). This theory approximates the response of the lattice at a radius R from defect centre (in region I) of charge Q in terms of a polarisation P where:

$$P = Q\,\underline{r}\,(1-\varepsilon^{-1}) / 4\pi|r|^3 \qquad (2.2.10)$$

and ε is the dielectric constant of the lattice. The contribution to the total energy of the system from the region I / region IIb interaction is given by:

$$E^{b}_{1,2} = -\frac{Q^2}{2} \sum_{j \in IIb} q_j \frac{M_j}{|R_j|^4} \qquad (2.2.11)$$

Where M_j is the Mott-Littleton parameter for the sub lattice and is given for a dielectrically isotropic crystal by:

$$M_j = \left(\frac{\alpha_j}{\Sigma_k \alpha_k}\right)\left(1-\varepsilon^{-1}\right) \qquad (2.2.12)$$

Where α is the polarisability of the k^th^ sub-lattice. For the more general case of a dielectrically anisotropic crystal, $E^b_{1,2}$ can be written as:

$$E^b_{1,2} = -\frac{Q^2}{2}\sum_{j\in IIb}\left[\frac{\sum M_j^{\alpha\beta}.R_j^{\alpha}.R_j^{\beta}}{|R_j|^6}\right] \tag{2.2.13}$$

Where the sum over all j refers to ions in region II and α and β refer to Cartesian coordinates. This method is only valid when the sizes of region I and IIa are chosen to be large enough so that the defect energy no longer changes with increase in region size. In this work, the values of region I size and cut-off potential are set as 3.5 l.u. and 3.0 l.u. respectively for the calculation of defect energies. These values were chosen after performing calculations as a function of region size and cut-off potential which reveal that increasing these values only varies the oxygen vacancy energy very little (figure 2.2.a and b). They also allow the calculations to be performed with an acceptable amount of computer time.

We note that the calculation of point defect energies at surfaces and interfaces is based on the same principle but defects are now on the open surface of the material.

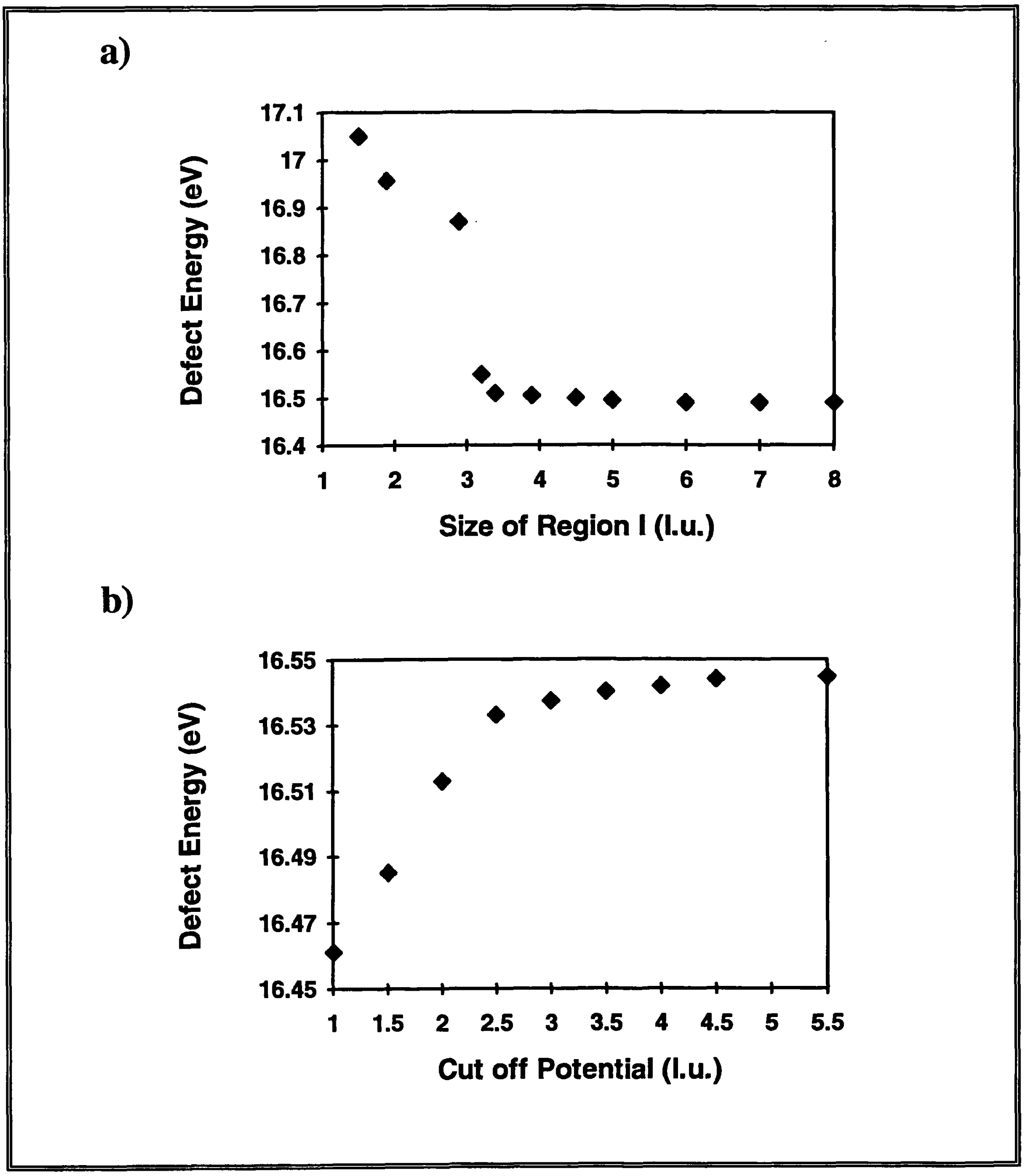

Figure 2.2 Variation of defect energy in the bulk of the crystal using CASCADE

a) Oxygen vacancy as a function of region I size

b) Oxygen vacancy as a function of cut-off potential

2.3 Calculations of extended pure and defect energies of surfaces
MIDAS

The ionic crystal structures near surfaces and heteroepitaxial interfaces are modelled using the computer code MIDAS (Tasker 1978) (**M**inimisation for **I**nterfacial **D**efects **A**nd **S**urfaces). Extended planar defects that maintain two dimensional periodicity can also be considered provided that the net charge on the crystal is zero. Energies calculated using this code are energies at constant surface area.

The program considers the crystal as a stack of planes periodic in two dimensions (figure 2.3). The stack is divided into two regions (using a scheme similar to that developed by Norgett in the HADES code), i.e. we employ a region I, where the ions are allowed to relax independently of each other, and a region II, where the ions are held fixed relative to each other. Region II is included to ensure the potential of an ion at the bottom of region I is correctly calculated. The top of region I is the free surface (figure 2.3.a) unless two such blocks are placed together enabling the lattice energy of the perfect crystal or a grain boundary to be calculated (figure 2.3.b). When modelling a perfect crystal or grain boundary, region II may however move as a whole, enabling the crystal to 'expand' or 'contract'. An interface can be created by a vector displacement or rotation of block I with respect to block II. If block I is displaced relative to block II by a vector within the interfacial plane, a stacking fault is produced and a vector displacement perpendicular to the interface results in the formation of a sheer plane. Rotations of block I with respect to block II about an axis perpendicular to the interfacial plane results in a twist grain boundary and parallel to the interfacial plane a tilt grain boundary is formed. The program also enables two dissimilar crystal structures to be placed together enabling a heteroepitaxial interface to be simulated (chapter 6). The vector displacements and rotations also apply to these systems enabling the modelling of epitaxial structure.

The surface energy E_S , per unit area can be defined as:

$$\gamma_s = \sum_{\lambda=1}^{n} \frac{E_s - \frac{1}{2} E_b}{\text{Area}} \quad , \qquad (2.3.1)$$

where the energy is summed over all ions in plane *n* and E_b is the bulk energy. This calculated value can be compared directly to the experimental determined surface energy when the latter are available.

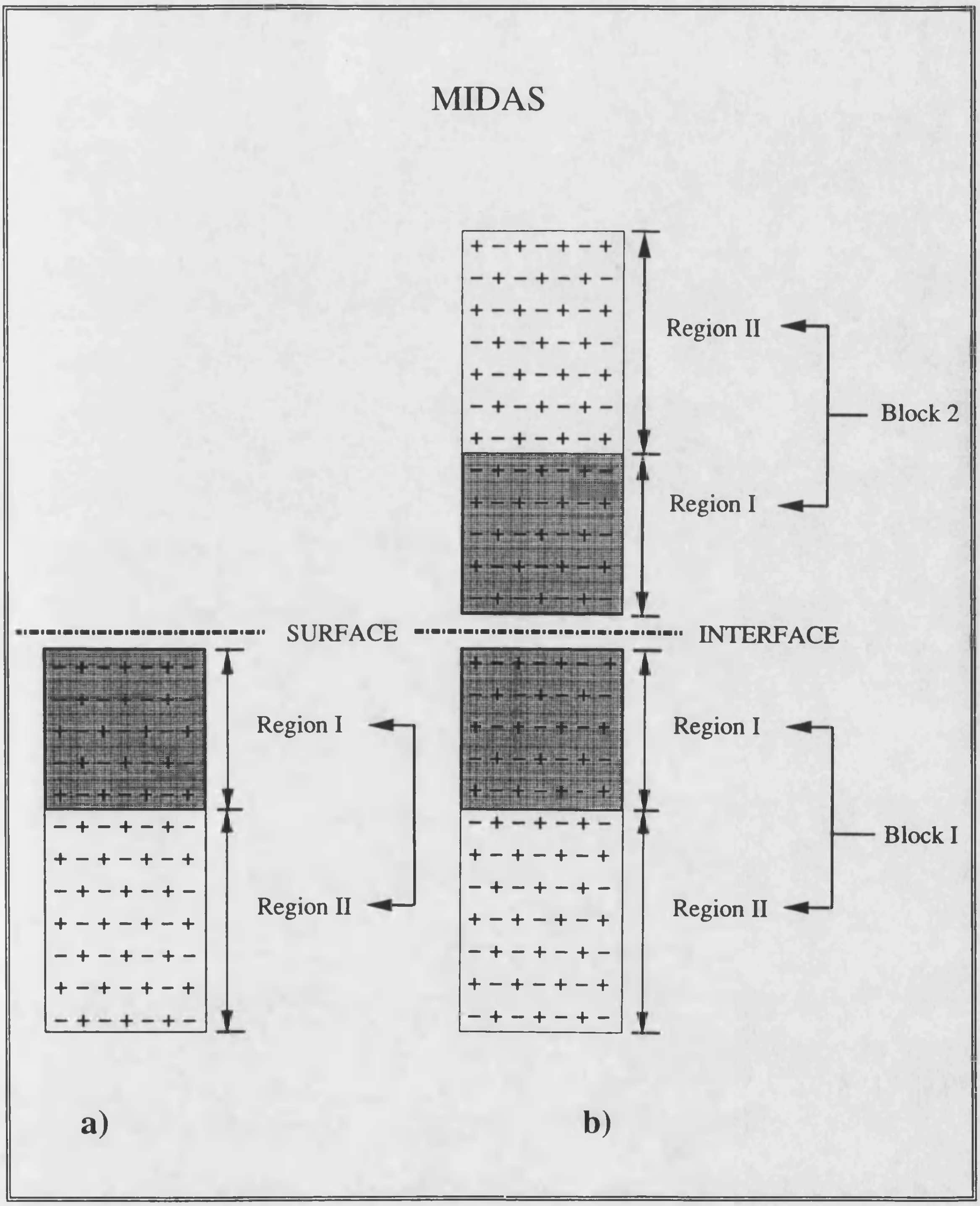

Figure 2.3 Schematic representation of the crystal regions for the calculations of defect energies at the a) surface and b) interface of materials.

2.4 Calculations of the point charge defect energies near the surface in ionic crystal - CHAOS

The calculation of point defect energies at surfaces or near interface regions of ionic crystals can be calculated using the computer code CHAOS (Computer simulation **HA**des **O**n **S**urfaces) (Duffy and Tasker 1983a). It is based on the HADES program (section 2.2) with necessary modifications (described below) to account for the existence of a surface or interface (figure 2.4). The defect energy is given as the difference in energy between the perfect crystal and that containing the point defect. The spherical crystal region is constructed as a series of circular discs lying parallel to the surface, with the radius decreasing with increasing distance from the centre of the hemisphere.

The relaxed structure of the perfect surface obtained from the MIDAS program (section 2.3) is used as the starting point for the calculation of point defect energies. The existence of the surface necessitates modifications relating to the two-dimensional periodicity of the reference configuration. In bulk crystal calculations, the Madelung energies are calculated using a three-dimensional Ewald Summation (Ewald 1921) which is inappropriate to surface calculations. In CHAOS, a two dimensional lattice summation method developed by Parry (1975a, 1975b) is employed. The Ewald method for calculating the Madelung energies in systems maintaining 3-dimensional periodicity is described in appendix A1.1 and the Parry method which addresses the calculation of the Madelung energies in systems maintaining 2-dimensional periodicity is discussed in appendix A1.2.

The calculation of the ionic displacements and energy of the continuum is also modified as a result of the surface or interface. For HADES, the energy of the continuum is calculated (assuming cubic symmetry) by a discrete $1/R^4$ summation (equation 2.2.11); but this assumes there is no structural deviation from the perfect crystal structure away from the defect (i.e. in region II). This is true for three dimensional lattices. However for surface or interface calculations, the modification of ionic positions or indeed interplanar spacings at the surface or interface regions must be addressed. In CHAOS, the energy is calculated by a combination of a discrete sum of planar integrals around the interface for all planes in regions I and II defined by the MIDAS code, and a volume integral over the remainder of the crystal. The planar integrals therefore take explicit account of the dilation of the crystal at the interface:

$$E_{IIb} = -Q^2/2\,(E_{Planar} + E_{Volume}) \qquad (2.4.1)$$

$$E_{Planar} = \sum_{\substack{p\in I \\ p\in IIa}} \Sigma_j q_j M_j \int_{\tau}^{\infty} \frac{1}{\left(\underline{R}^2 - \underline{R}_p^2\right)} 2\pi\underline{R}(d\underline{R}) \qquad (2.4.2)$$

$$E_{Volume} = \sum_j q_j M_j \int_{RIIb}^{\infty} \frac{1}{|\underline{R}|^4} 2\pi\underline{R}^2(d\underline{R}) \qquad (2.4.3)$$

where $\underline{R}_p$ is the perpendicular distance from the origin and plane p, M_j is the Mott-Littleton displacement factor for sublattice j, Q_j is the total defect charge, $\tau = (RIIb^2 - r_p^2)^{1/2}$ and R is cut-off radius.

The response of the interface or surface ions, to an electric field, is taken to be identical to that of the bulk ions (i.e. they have the same Mott-Littleton coefficients). This is clearly an approximation as the environment at the surface deviates from the bulk. For ionic materials with little surface relaxation such as CeO_2 (111) the effect is minimal. However, for materials with large surface relaxation such as dipolar surfaces and especially interfaces, this approximation may not be trivial. CHAOS has been extended to accommodate this effect by calculating the Mott-Littleton coefficients for the bulk and surface ions. The modified coefficients are then used to determine the displacements and polarisation energies of the ions close to the surface or interface. This necessarily increases the computational time and was not included in the work in this thesis, although its inclusion would provide a useful extension to this work.

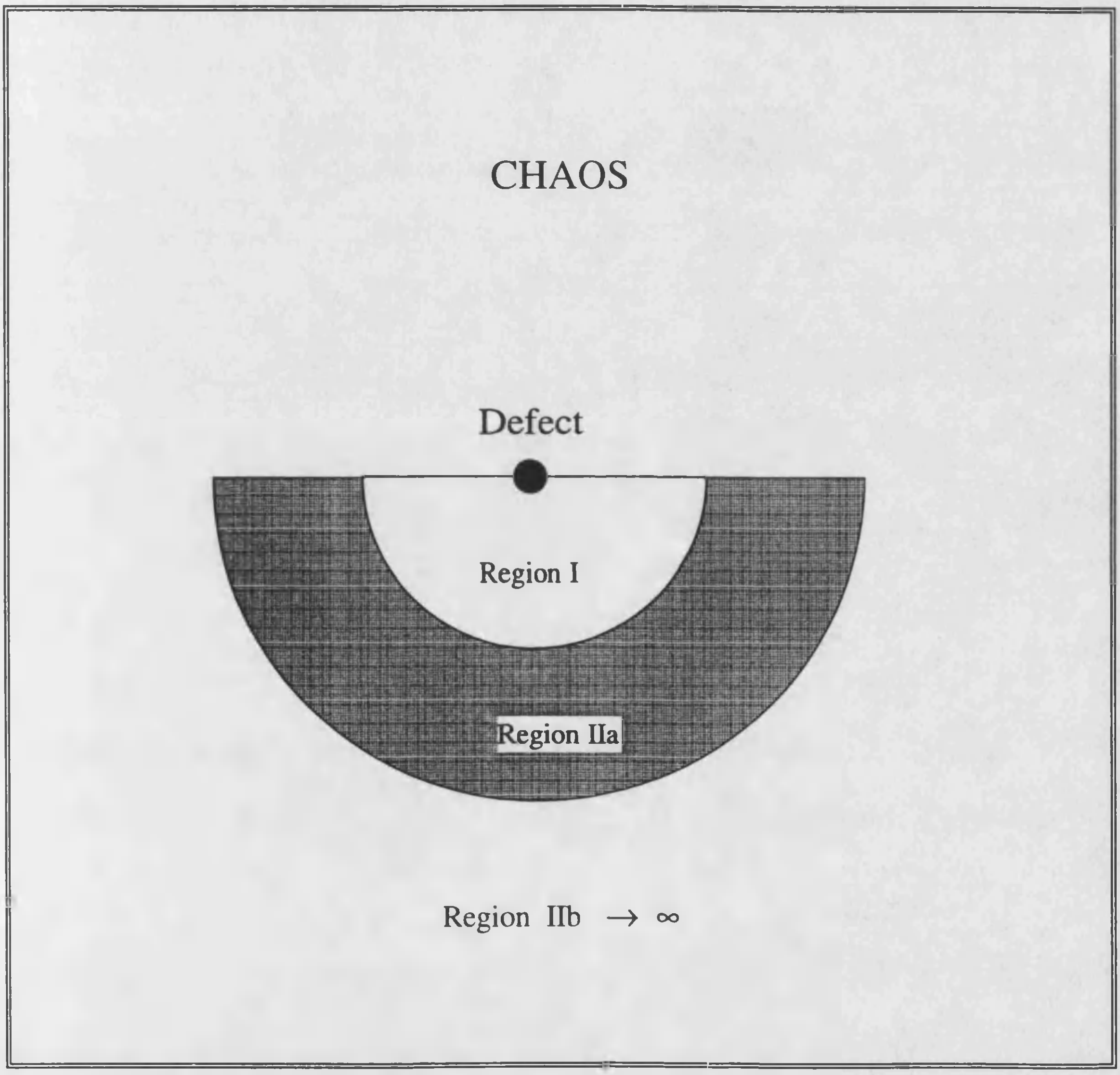

Figure 2.4 Two regions strategy used for the calculations of point charge defects at the surface of ionic crystal - CHAOS

2.4.1 Surface Madelung Potential

The relaxed perfect surface structure, generated by the MIDAS program (discussed in section 2.3), is used as a reference state for the calculation of point defect formation energies using the CHAOS program. The Madelung energies calculated by the MIDAS code for surfaces are significantly lower at the surface plane than in the interior of the crystal. This energy generally increases and reaches a constant value as going further into the bulk. However, this constant value will never reach the bulk equivalent value which is calculated by CASCADE, because of the different methods by which the boundary conditions are defined when considering three-dimensional bulk and two-dimensional surface.

For the bulk defect calculation, there are no effects due to the terminating surface or interface because the calculation refers to an infinite system. In contrast, in surface calculations, two-dimensional boundary condition apply; after relaxation, there will be a perturbation of the surface dipole layer which creates an electric potential which acts through out the bulk of the crystal. This leads to a shift in Madelung field near surface region (Duffy and Stoneham 1983).

The shift in Madelung field is a result of a dipole induced by ionic relaxation near surface and calculated as qV where V is the shift in potential by defect of full ionic charge, q. The magnitude of the shift V is dependent on the relaxation of ions on the surface and therefore will be different for different surfaces. In this work, the shift in Madelung potential of ceria is 1.73eV for the (310) surface, 1.35eV for the (110) surface, and 4.793eV for (111) surface. All calculations of charged defects at surfaces are adjusted for this term.

2.4.2 Image charge effect

A surface or interface implies a discontinuity in the dielectric constant and therefore the energy associated with the defect must also include a contribution from the image charge induced as a result of the defect. The dielectric discontinuity at the interface of two materials, will alter the polarisability of the oxide around the defect near the interface (Stoneham and Tasker 1987). From classical electrostatics, the energy of a charge near the dielectric interface is calculated as

$$E_{image} = \frac{Q^2}{4z\varepsilon_1}\left(\frac{\varepsilon_1 - \varepsilon_2}{\varepsilon_1 + \varepsilon_2}\right) \qquad (2.4.4)$$

Where

Q : the charge of defect

ε_1 : the dielectric constant of the oxide which bears the defect, ceria ($\varepsilon_1 = 20$)

ε_2 : the dielectric constant of the second material e.g. Al_2O_3 ($\varepsilon_2 = 11$)

vacuum ($\varepsilon_2 = 1$)

z : the distance of defect from the interface of surface

For defect calculations at ceria surfaces, because the value of (ε_1 - ε_2) is positive, the effect of the image charge at the oxide surface is to repel the charged defect from the boundary. This reduces the stability of the charged defect as it approaches the surface. This effect however is very small compared to ionic relaxation effects. When oppositely charged defects are brought towards the surface/interface as a neutral bound pair, the charge on one defect in oxide will interact with the image charge of the other and vice versa, hence, the pair will not be repelled from the surface.

When calculating the displacements of the ions in region IIa and the polarisation energy of region IIb, the image charge is induced via the defect at a distance d/2 (where d is the interplanar spacing) above the uppermost ion on the top plane of the material containing the defect. At present the CHAOS program adopts a dielectric constant of $\varepsilon_2 = 1$ for the second material and is therefore only strictly applicable to free surfaces.

2.5 Energy Minimisation Methods

In static simulations, the ion positions are adjusted so that the forces acting on each ion in region I are zero, i.e. to satisfy equilibrium condition in equation 2.2.5. Initially, a configuration is specified for the system; then the energy $E(\underline{x})$ is calculated, using the interatomic potentials, which are a function of all the structural variables, $\underline{x}$. The structure is then adjusted, using an iterative scheme until the system achieves a minimum energy configuration. This is achieved by a Newton-Raphson method which requires the first and second derivatives in the minimisation procedure.

The gradient $(dE/d\underline{x})$ alone may be used to direct the minimisation. This is the well known conjugate gradient technique, the values of variable $\underline{x}$ in the (n+1)th iteration are related to those in the nth iteration by:

$$\underline{x}^{(n+1)} = \underline{x}^{(n)} + C^{(n)}\underline{s}^{(n)} \quad , \qquad (2.5.1)$$

Where $C^{(n)}$ is a numerical constant chosen for each iteration to optimise the efficiency of the minimisation. The displacement vector $\underline{s}^{(n)}$ uses information on the previous values of the gradients to speed the convergence, therefore:

$$\underline{s}^{(n+1)} = -\underline{g}^{(n)} + \underline{\beta}^{(n+1)}\underline{s}^{(n)} , \qquad (2.5.2)$$

where $$\underline{\beta}^{(n+1)} = \frac{\underline{g}^{T(n)}.\underline{g}^{(n)}}{\underline{g}^{T(n-1)}.\underline{g}^{(n-1)}} \qquad (2.5.3)$$

and $g^{(n)}$ are vectors whose components are the derivatives with respect to individual coordinates and the superscript, T, indicates the transpose of the vector.

Much more rapid convergence is achieved if second derivatives are used to guide the minimisation, in which the successive values of the variables are calculated according to:

$$\underline{x}^{(n+1)} = \underline{x}^{(n)} - \underline{H}^{(n)}.\underline{g}^{(n)} , \qquad (2.5.4)$$

where the matrix $\underline{H} = \underline{W}^{-1}$, in which the elements $\underline{W}_{ij}$ are the second derivatives:

$$\underline{W}_{ij} = \frac{\partial^2 E}{\partial x_i \, \partial x_j} \qquad (2.5.5)$$

2.5.1 Updating Algorithm

The improved speed of convergence is easily lost in the extra computational cost required to calculate and invert the second derivative matrix for each iteration. However algorithms are available which enable the second derivative matrix to be updated without recalculation and inversion. The algorithms are approximate and it is therefore necessary to recalculate $\underline{H}$ every few iterations. The most widely used of these is the Davidon-Fletcher-Powell algorithm (Davidon 1959, Fletcher and Powell, 1963) in which the matrix, $\underline{H}$, is updated each iteration according to the formula:

$$\underline{H}^{(n+1)} = \underline{H}^{(n)} - \frac{\left(\underline{H}^{(n)}.\Delta\underline{g}^{(n)}\right).\left(\Delta\underline{g}^{T(n)}.\underline{H}^{(n)}\right)}{\left(\Delta\underline{g}^{T(n)}.\underline{H}^{(n)}.\Delta\underline{g}^{(n)}\right)} - \frac{\left(\Delta\underline{x}^{(n)}.\Delta\underline{x}^{T(n)}\right)}{\left(\Delta\underline{x}^{T(n)}.\Delta\underline{g}^{(n)}\right)} \qquad (2.5.6)$$

Where $\Delta\underline{g}^{(n)} = \underline{g}^{(n+1)} - \underline{g}^{(n)}$ (2.5.7)

$\Delta\underline{x}^{(n)} = \underline{x}^{(n+1)} - \underline{x}^{(n)}$ (2.5.8)

The number of iterations after which $\underline{H}$ is recalculated is also crucial to the speed of minimisation, calculations (chapters 4, 5 and 6) have shown that the optimum number of iterations after which $\underline{H}$ should be recalculated varies from 5 to 20 for the various systems considered, with the time for the minimisation being reduced considerably by making the optimum choice. There is however no method of determining the optimum number of iterations after which $\underline{H}$ should be recalculated without first performing the minimisation.

One major limitation with the Newton-Raphson method, is the enormous c.p.u. memory requirement for storing the inverse of the second derivative matrix, which may become prohibitive even with large memory computers for the structures with large number of atoms in the unit cell or for defects with very large sizes of region I.

In the appendix we address the calculation of the long range Coulombic terms by application of the Ewald method for systems with three-dimensional periodicity and the Parry method for systems with two-dimensional periodicity. These methods for calculating the Coulombic terms enable a substantial reduction in the computational time required for the calculations to be made and are inherent in all the static simulation codes.

2.6 Summary

The techniques described above allow atomistic simulation methods to address important problems including the structure and stability of pure and defect crystal and their surfaces and interfaces. The following chapter describes how the potentials are derived for implementation simulation.

CHAPTER 3

POTENTIAL MODELS

3.1 Introduction

All calculations in this work were undertaken using static lattice minimisation methods which employ interatomic potentials to describe the interactions between the ions in the crystals. The reliability of the results thus depends on the accuracy of the potentials used, all of which were based on the Born model of the ionic solid (Born 1954), which uses a classical description of the crystal, including a long range Coulombic interaction and a short range term to model the Pauli repulsions and van der Waals attractions between electron charge clouds. In this theory, the pair potential approximation is employed, as there is good evidence that the approximation is acceptable for strongly ionic materials, although we note that three-body potentials have been employed in modelling semi-ionic systems (Sanders et al. 1984 and Titiloye et al. 1989).

3.2 The Born model of the ionic crystal

The energy of a perfect crystal within the pair potential approximation can be written as follows:

$$U_{\text{Lattice}} = \sum_{i,j=1}^{N} \frac{q_i q_j}{r_{ij}} + \sum_{i,j=1}^{N} \Phi(r_{ij}) \ , \qquad (3.1)$$

where N is the total number of atoms in the crystal.

The first term describes the Coulombic interactions between a pair of atoms or ions with charges q_i and q_j separated by distance r_{ij}. This provides the attractive component of the crystals cohesive energy.

The second term, $\Phi(r_{ij})$, represents the short range interactions acting between the atoms, which includes contributions from many terms including covalency, non-bonded repulsion and dispersion. These short range interactions provide the repulsive forces which are very high at low values of r.

We have noted that only pair potentials are included in our model, as such interactions can reproduce the crystal properties with reasonable accuracy for strongly ionic materials. In chapter 6, however, we study the application of atomistic simulation to heteroepitaxial interface systems, where the misfit between the overlaying material and substrate will have to be accommodated by either an expansion or a contraction of the materials at the interfacial plane. The inclusion of three-body terms may have a larger effect on the relaxational behaviour and interfacial stability of such systems than is the case for surface relaxation or defect energy calculations. A useful extension to this work would therefore be to study the effect of the three-body and higher order terms on the interfacial energies and structures.

The calculation of the lattice energy as the sum of the total Coulombic and short range energies is difficult as the former converges slowly. This problem was solved by Ewald (1921) using a technique that partitioned the Coulomb sum into two parts: one converges quickly in real space and the other is rapidly convergent in reciprocal space. Further details will be given in chapter 2.

3.3 Short range interactions

3.3.1 Two-body bonded interactions

These are interactions which occur between open-shell atoms and normally involve covalent bonds. The simplest and most widely used function applied to a bonding pair of atoms is the **bond harmonic** function:

$$\Phi(\mathbf{r}_{ij}) = \tfrac{1}{2} \mathbf{K} [(|\mathbf{r}_i - \mathbf{r}_j| - \mathbf{r}_e]^2 \quad , \qquad (3.2)$$

where r_e is the equilibrium bond distance and K is the bond force constant. Functions of this type are quite adequate for small deviations from the equilibrium bond distance. However, the anharmonicity of real systems is not represented in this expression. Greater reliability over a wider range of separations can be achieved by using the **Morse** function, which has the form:

$$\Phi(\mathbf{r}_{ij}) = \mathbf{D}_e \{1 - \exp[-\beta (|\mathbf{r}_i - \mathbf{r}_j| - \mathbf{r}_e)]\}^2 - \mathbf{D}_e \quad , \qquad (3.3)$$

where D_e is the dissociation energy of the bond, r_e is the equilibrium bond length and β is a variable parameter, which can be determined from spectroscopic data (assuming the potential well is harmonic at r_e).

$$\beta = \omega_e \sqrt{(\mu / 2\,\mathbf{D}_e)} \quad , \qquad (3.4)$$

where ω_e is the vibrational frequency and μ is the reduced mass.

The Morse potential is employed to describe the bonding interactions between atoms of organic molecules when modelling the adsorption of gaseous molecules including NO and CO onto the surfaces of a solid material (chapter 5).

3.3.2 Two-body non-bonded interactions

These are interactions between closed-shell species such as inert gas atoms and ions in crystals. The most widely used function is the **Lennard-Jones** potential (employed almost exclusively for simulations of molecular systems) which is of the form:

$$\Phi\left(r_{ij}\right) = \frac{A}{\left|r_i - r_j\right|^{12}} - \frac{C}{\left|r_i - r_j\right|^{6}} \quad , \tag{3.5}$$

where the first term represents the Pauli repulsion and the second, the van der Waals attraction; A and C are variable parameters. C depends on the polarisability of the interacting ions as it represents the dispersive, induced dipole-dipole interactions between the ions.

The majority of the potential functions employed in this thesis employ the **Buckingham** potential, in which the r^{-12} term of the Lennard-Jones potential is replaced by an exponential repulsive term, giving:

$$\Phi\left(r_{ij}\right) = A \exp\left(-\frac{\left|r_i - r_j\right|}{\rho}\right) - \frac{C}{r^6} \quad , \tag{3.6}$$

A and ρ depend on respectively the size and hardness of ions (Busing 1970); the attractive C/r^6 term is included to take account of the van der Waals, dispersive and covalent interactions. When the C/r^6 term is omitted, the potential function is known as **Born-Mayer** potential.

3.4 Ionic polarisability

Although rigid ion models have be applied to defect studies (Gillan and Dixon 1980), accurate calculations of defect energies generally require the inclusion of polarisable ions. Omission of polarisability moreover limits the ability of the model to calculate accurately, for example, lattice dynamical properties (Woods et. al. 1960) and segregation energies (Colbourn and Mackrodt 1985). Furthermore, the rigid ion model implies the optic (high frequency) dielectric constant is unity and therefore is unable to reproduce this property of the crystal.

The most effective way of including of ionic polarisability is to use the shell model of Dick and Overhauser (1958), which treats an ion as a core of charge X in which all the mass is concentrated, surrounded by massless spherical shell of charge Y (which is nevertheless a point entity). The core positions represent the positions of the ionic nuclei, and the shell, those of the valence shell electrons, although little physical interpretation can often be assigned to the shell charge which may indeed sometimes be positive. The formal charge of the ion is (X+Y); core and shell are coupled by a harmonic spring of constant k. The free ion polarisability, α, of an ion of type i is given by:

$$\alpha_i = Y_i^2 / k_i \quad , \qquad (3.7)$$

and the core/shell self energy :

$$\Phi_i (r_i) = k_i r_i^2 \quad , \tag{3.8}$$

The parameters Y and k are obtained by empirical fitting to dielectric data, elastic constants or phonon dispersion curves. For defect and surface calculations, a quadratic k′ term may be added to the anion-anion core-shell self energy. This is necessary because during relaxation, some core-shell separations become excessive and physically unreasonable. The interaction between core and shell then becomes:

$$\Phi_i (r_i) = k_i r_i^2 + k_i' r_i^4 \quad , \tag{3.9}$$

The polarisability therefore varies non-linearly with the electrostatic field for high fields. The advantage of this added potential form is that the calculated structure, high frequency and static dielectric constants remain unchanged in near-equilibrium geometry while preventing large electric fields from separating cores and shells during the relaxation process.

Since polarisation is described in terms of the displacement of the shells relative to the core, and since the short-range repulsions are generally taken to act between the shells only, the model includes the required coupling between short range repulsion and polarisation. The Coulomb forces act between all cores and shells except for the cores and shells belonging to the same ion. The relative merits of the shell model description of polarisability in ionic solids are discussed in more detail by Catlow and Mackrodt (1982) and Catlow (1986).

3.5 Derivation of short range potential parameters

There are two main ways in which short range interatomic potentials are derived; the first is based on empirical fitting of the parameters so that the calculated physical properties are in agreement with the experimental data, while in the second, the parameters are obtained from quantum mechanical techniques which are used increasingly to calculate the short range interactions.

Empirical potentials rely on the validity of the analytical forms used for the potential when they are extrapolated to interatomic separations that differ substantially from those used in the parameterisation. Non-empirical potentials offer the promise of greater reliability in describing the short range potential energy terms for a wide range of interatomic separations, provided that theoretical methods of sufficient accuracy are available. They have therefore major potential advantages for systems which exhibit substantial deviations in interatomic separations, as in defect calculations where interatomic spacings in interstitial sites can be up to 1Å closer than the corresponding equilibrium separation. Empirical potentials do, however, perform well in comparison to their non-empirical counterparts as the deficiencies in the analytical form of the empirical methods may be compensated, in part, by the fitting procedure. Although an obvious disadvantage of these methods compared to non-empirical procedures is that if no experimental data exists, the procedure cannot be applied; furthermore the accuracy of the empirical potential can not exceed the accuracy of the experimental data. These two different approaches are now discussed in greater detail.

3.5.1 Empirical potentials

This is the simplest and most widely used way to obtain potentials. In this work, the analytical term employed to describe the short range potential energy between anion-anion is the Buckingham interaction (equation 3.6). The parameters A, ρ and C are determined by a least squares fitting routine to the available experimental crystal properties such as the lattice energy, lattice constant, dielectric and elastic properties and phonon frequencies. In practice, the procedures employed for calculation of properties are "run in reverse", with potential parameters being adjusted until the best agreement is achieved between calculated and experimental properties.

3.5.2 Electron gas potentials

The "electron gas" method is a simplified form of the local density functional theory and is based on methods developed by Wedepohl (1967) and subsequently applied by Gordon and Kim (1972). This method was applied to calculate the intermolecular forces between open-shell systems (Harrison and Sokel 1976), to closed-shell systems (Clugston 1978), and has been extensively applied to ionic systems by Mackrodt and Stewart (1979).

The advantage of this method is that it is computationally inexpensive as it is based on a formalism for treating electrons in an atom or ion as a degenerate Fermi gas. This density functional approach assumes we have a uniform electron gas which is spherically symmetrical with the electron distribution being the same for all inter-nuclear separations. Thus the electron density of a lattice of ions is assumed to be the sum of the electron densities of the individual isolated ions, which is a reasonable approximation only for closed shell atoms or ions, and as such might be expected to be acceptable for the potentials for classic ionic materials. In contrast, we would expect there to be distortions of the individual electron distributions for more covalent systems.

The electron densities of the component ions are commonly determined by calculating the wave functions for the ions in the electrostatic crystal environment, i.e. the wave function is centred at a Madelung well. This is important for anions especially for O^{2-} where the second negative charge is unbound (Grimes 1990), whereas cation electron densities are strongly bound and there is therefore very little effect on the wave function of the applied fields; hence the free ion densities are used.

The Madelung well used in calculating anionic wave functions is spherically symmetric and has the form:

$$V(r) = V_o \qquad \text{for } (r \leq r_x) \qquad (3.10)$$

$$V(r) = V_o\, r_x / r \qquad \text{for } (r > r_x) \quad , \qquad (3.11)$$

Where V_o is the well depth which will be negative for electrons of anion (and positive for those of a cation); r_x is the ionic radius.

In this work, the cation densities were calculated numerically (Herman and Skillman 1963) and incorporated a relativistic correction (Cowan and Griffin 1976). For the oxygen density, the radial function of the spherical harmonic wave function is defined as expansions in analytic Slater (Clementi and Roetti 1974) functions; the initial potential or electron density is estimated, and the atomic densities will be calculated using the Hartree-Fock exchange potential (Harker 1974).

Having calculated the electron density of the interacting ions, the total energy is written as:

$$\mathbf{E_{total} = E_{coul} + E_{kin} + E_{exch} + E_{corr} + E_{disp}} \qquad (3.12)$$

where the terms are defined as follows:

E_{coul} : the Coulomb energy which includes the electron repulsion energy, the nuclear repulsion energy and the electron - nuclear attraction energy.

E_{kin} : the kinetic energy calculated directly from the kinetic energy of a uniform electron gas which is proportional to the $^5/_3$ power of the electron density.

E_{exch} : the exchange energy of electrons in the overlap region of the interacting atoms/ions. This is a repulsive energy and is proportional to the $^4/_3$ power of the electron density.

E_{corr} : the short range correlation energy which is proportional to the $^1/_3$ power of the electron density

E_{disp} : the non-overlap long range part of the correlation or dispersive energy which includes the van der Waals interaction. This interaction arises from coupling between instantaneous electric multipole moments in participating atoms, and can be calculated using formulae of Slater and Kirkwood (1931).

Details of the calculation of the individual components of the energy together with the discussions of assumptions made in the derivation of interionic potentials based on using electron gas methods are given in Gordon and Kim (1972), Clugston (1978), and Harding and Harker (1982). Using potentials derived by the electron gas method, early studies of perfect lattice properties were reported by Kim and Gordon (1974), Cohen and Gorgon (1975 and 1976), Wedepohl (1977a, 1977b), and of defect properties by Keeton and Wilson (1973), Catlow and Norgett (1973), Catlow et al. (1977), and Mackrodt and Stewart (1977 and 1979).

In the present study, a program WEDEPOHL (Harding and Harker 1982), an interatomic potential generator which takes the numerical representation of the electron densities as input was used to calculate the interaction energies between ionic wave functions using the method outlined above (Wedepohl 1967). In the final stage of the procedure, the resulting potential is fitted to a Born-Mayer functional form by least square fitting over a wide range of interionic separations.

3.5.3 Modified (or empiricised) electron gas potentials

The short range potentials for dopant/anion interactions used in this thesis are derived initially by the electron gas method as in several cases there is an inadequate range of data for deriving an empirical model. Previous experience has indicated that poor results will be obtained if potentials from the electron gas methods are used in conjunction with empirical potentials (Butler et al. 1983). This problem can be solved first by evaluating using the electron gas method, the *difference* between a dopant-lattice and a reference lattice-lattice potentials, (e.g. dopant-oxygen and cerium-oxygen for the case of dopants in CeO_2). We then add this difference to the values obtained *empirically* for reference interactions (V^R_{Em}). These new values are finally fitted to the Buckingham form to yield an "empiricised" electron gas potentials (Grimes et al. 1989).

$$\mathbf{V^*_{empiricised}(r) = Fitted\,\{[V^R_{EG}(r) - V^*_{EG}(r)] + V^R_{Em}(r)\}} \qquad (3.13)$$

This is acceptable, as although the absolute values of electron gas potentials may be inconsistent with the empirical potentials, the difference between them are considered to be reliable. This method therefore provides a consistent set of potential parameters for the dopant-anion interactions which are used in defect calculations for precious metal ions interacting with the ceria support in chapter 5.

3.6 Comparison of different potentials for cerium dioxide

Three sets of potentials for CeO_2 are evaluated by reference to perfect lattice and defect properties of CeO_2. In particular, the following models were considered.

Potential 1 was derived by Butler (1983), and is a combination of empirically derived potentials for anion-anion interactions (Catlow 1977a) and electron gas potentials for the cation-oxygen interactions.

Potential 2 was derived by Grimes and Catlow (1991) for all interactions using the electron gas method.

Potential 3 is the same as potential (1) with an additional C/r^6 term for the cerium-oxygen interaction, which together with a change in values of the shell charge Y results in a slight modification to the ionic polarisabilities, i.e. an increase in polarisation of the oxygen and decrease in that of the cerium.

In all calculations using these three sets of potentials, the Ce^{4+}-Ce^{4+} short range potential is set to zero.

Table 3.1 Short range potential parameters for CeO_2

		A (eV)	ρ (Å)	C (eV/$Å^6$)	Y (|e|)	k (eV/$Å^2$)	α ($Å^3$)
(1)	**O**	22764.30	0.149	43.83	-2.83	257.89	0.45
	Ce	1986.83	0.35107	0.0	9.38	201.62	6.28
(2)	**O**	108.00	0.38	56.06	-4.4	296.80	0.94
	Ce	1984.20	0.3494	26.44	-7.3	1957.0	0.39
(3)	**O**	22764.30	0.149	43.83	-6.1	291.75	1.84
	Ce	1986.83	0.35107	20.40	7.7	419.874	2.03

Table 3.2 Physical properties

	Lattice Energy (eV)	**Dielectric constant**		C_{11}	C_{12}	C_{44}	Lattice constant (Å)
		High	Static	(10^{11}dyn cm^2)			
(1)	-104.602	5.412	22.578	49.022	14.042	13.227	2.7343
(2)	-106.303	1.934	17.112	53.472	13.746	7.371	2.6917
(3)	-105.635	3.996	19.548	50.471	14.294	1.603	2.7055
expt	-109.0**	4.0*	18.6-20*				2.7055*

Table 3.3 Intrinsic defect energies (eV)

	$V_O^{\cdot\cdot}$	V_{Ce}''''	O_i''	Schottky E_S	Anion Frenkel-E_F	(E_S-2 E_F)
(1)	15.642	83.601	-10.407	10.282	5.235	-0.188
(2)	16.023	85.461	- 9.636	11.204	6.387	-1.570
(3)	16.342	83.519	-10.432	10.568	5.624	-0.680

(* Samsonov 1982 and ** La 1980)

One of the most striking features of the potentials apparent from the parameters reported in table (3.1) is the variation of the oxygen polarisability. The polarisability of cerium is fourteen times that of oxygen in potential (1) and slightly higher that of oxygen in potential (3), whereas it is only half that of oxygen in potential (2) owing to a higher value of the cerium spring constant. Although there is no reported polarisability for cerium, it is expected to be lower than that of the highly polarisable oxygen; potential (2) would therefore be a better set if polarisability only is taken into account. However, the high frequency dielectric constant of potential (2) is only half that of the experimental value indicating the lattice is insufficiently polarisable, whereas it is 30% higher than the experimental value for potential (1) as a result of the very high Ce polarisability.

In this work, potential (3) was chosen as it yields the most accurate lattice parameter which is an important requirement especially for the study of the interfaces between ceria and alumina. In addition, the dielectric constants are in reasonable accord with experiment which is of considerable importance in modelling defect properties.

Lattice energies and intrinsic atomic defect formation energies vary very slightly for potentials considered. The values of (E_S - $2E_F$) reported in table 3.3 are of special significance and will be discussed later in the chapter.

The reliability of the potentials derived are usually assessed on the basis of the accuracy of the modelling of the perfect lattice properties, in particular the lattice energy, dielectric constants, elastic properties and lattice constant. Only dielectric and lattice constant data are available for CeO_2. It would be helpful if elastic data were available as we note that there are appreciable differences between the calculated values for the three potentials. In particular, a low value of C_{44} constant is calculated for potential (3) which it would be useful to verify experimentally.

Having chosen the potentials for the study of perfect lattice and intrinsic defects in ceria, the next step is to derive a suitable set of short range potentials for extrinsic defect-oxygen interactions. This is achieved by the electron gas method, by first choosing a suitable oxygen wave function to obtain the electron densities for the interacting species and subsequently suitable cerium-oxygen short range parameters which are then used as a reference for derivation of metal defect-oxygen short range parameters according to procedure described in section (3.5.3). Oxygen wave functions of four different well depths are considered (Harker 1974).

3.7 Derivation of the metal dopant-oxygen short range parameters

Four sets of short range potentials for cerium-oxygen interactions are calculated by the electron gas method employing four Madelung well depths in calculating the electron density for the O^{2-} ion. In particular, we have used well depths V_o equal to 0.5, 1.0, 1.5 and 2.0 atomic units (appendix 3). As noted earlier, the well has the form:

$$V(r) = - V_o \qquad r \leq r_x$$
$$V(r) = - V_o r_x / r \qquad r \geq r_x \quad ,$$

where r_x is the Born ionic radius (= 2.57 bohr). The 'free ion' electron density is used for all cations because the 'free ion' radial distribution functions do not change appreciably in the lattice.

Illustrated below is a comparison of the difference in physical properties and intrinsic defects in ceria using cerium-oxygen potentials calculated using the electron gas method with oxygen wave functions obtained using various oxygen well depths. Values of Y for both anion and cation are kept constant and the same as in potential (3); the oxygen-oxygen empirical potential is also that of potential (3).

Table 3.4 Physical properties of CeO_2

	Lattice Energy (eV)	**Dielectric** High	**Constant** Static	C_{11}	C_{12}	C_{44}	**Lattice Constant** (Å)
					10^{11}dyn/cm^2)		
(0.5)	-104.053	3.917	26.932	47.877	12.345	0.316	2.7277
(1.0)	-108.700	4.482	21.891	55.974	16.230	0.732	2.6298
(1.5)	-110.880	4.637	16.609	60.165	19.269	2.063	2.5987
(2.0)	-112.572	5.059	19.949	63.433	20.021	0.681	2.5527

Table 3.5 Intrinsic defect energies (eV)

	$V^{\cdot\cdot}_O$	V''''_{Ce}	O''_i	Schottky E_S	Anion Frenkel - E_F	**(E_S - 2E_F)**
(0.5)	15.116	81.494	- 10.093	7.673	5.023	- 2.373
(1.0)	16.547	85.168	- 11.139	9.562	5.408	- 1.254
(1.5)	17.626	87.632	- 11.662	12.004	5.964	0.076
(2.0)	17.653	87.950	- 12.133	10.684	5.520	- 0.356

From tables 3.4 and 3.5, we note that the discrepancy between the calculated and experimental lattice constant of ceria increases with increase in the well depth. However, another important criterion in assessing the suitability of potentials for ceria is the relationship between Schottky and Frenkel energies, where the Schottky defect is created in a perfect crystal by transferring atoms in stoichiometric proportions from lattice site in the bulk of the crystal to a surface site and a Frenkel defect is created when an atom is transferred from a lattice site to an interstitial site.

The defect reactions for these processes can be represented as follows:

Frenkel type : $O^{x}_{O} = V^{\cdot\cdot}_{O} + O''_{i}$

Schottky type : $Ce^{x}_{Ce} + 2\,O^{x}_{O} = V''''_{Ce} + 2\,V^{\cdot\cdot}_{O} + CeO_2$

where $V^{\cdot\cdot}_{O}$: Oxygen vacancy

O''_{i} : Oxygen interstitial

V''''_{Ce} : Cerium vacancy

CeO_2 : Mole of ceria

Ce^{x}_{Ce} : Cerium in lattice site

O^{x}_{O} : Oxygen in lattice site

On combining these two reactions, we can demonstrate the relationship

$$\therefore \quad (E_S - 2E_F) = E(V''''_{Ce}) - 2\,E(O''_{i}) + E(CeO_2) \quad , \qquad (3.14)$$

where the energies on the right hand side of this equation refer to the energies of the species in the brackets.

The importance of equation (3.14) can be shown as follows. First we consider the accommodation of excess oxygen in the lattice of CeO_2 ; a similar formalism would apply to doped system. In particular, we consider reactions:

$$O_2 \rightarrow 2\,O''_i + 4\text{ holes} \qquad (E_1)$$

$$CeO_2 + O_2 \rightarrow 2\,CeO_2 + V''''_{Ce} + 4\text{ holes} \qquad (E_2)$$

$$\therefore \quad E_2 - E_1 = CeO_2 + V''''_{Ce} - 2\,O''_i$$

(from equation 3.14)

$$E_2 - E_1 = E_S - 2E_F \qquad (3.15)$$

The equilibria governing the above equations are:

$$k_1 = \exp(-E_1/RT) = ([O''_i]^2\,[\text{hole}]^4) / P_{O2}$$

$$k_2 = \exp(-E_2/RT) = ([V''''_{Ce}]\,[\text{hole}]^4) / P_{O2}$$

$$(k_2 / k_1) = [V''''_{Ce}] / [O''_i]^2 = \exp\{-{}^1/_{RT}(E_2 - E_1)\}$$

and from (3.15), $(k_2 / k_1) = \exp\{-{}^1/_{RT}(E_S - 2E_F)\}$

$$\therefore \quad [V''''_{Ce}] = \exp\{-{}^1/_{RT}(E_S - 2E_F)\} \,.\, [O''_i]^2 \qquad (3.16)$$

From equation (3.16),

If $(E_S - 2E_F) > 0$ then $[V''''_{Ce}] << [O''_i]$

If $(E_S - 2E_F) < 0$ then $[V''''_{Ce}] >> [O''_i]$

Thus the significance of these expressions is that if (E_S - $2E_F$) is negative then cation vacancy disorder will dominate in doped or oxidised system; if positive, oxygen interstitials will be the major species. The latter is generally thought to apply, which is clearly of considerable significance if CeO_2 is to be used as an "oxygen reserve" in an environment operating under widely varying oxygen pressures.

An essential criterion in choosing the suitable potentials for CeO_2 is therefore the value of (E_S - $2E_F$) which should be ≥ 0. The small positive value of (E_S - $2E_F$) of potential with well depth 1.5 Hartrees shows that this potential is most suitable for our work related to catalyst activity.

In previous studies, the variation in Madelung well depth has been found to have very little effect on the potentials derived (Lawence 1988), the relaxations of five different surfaces of Cr_2O_3, {0001}, {1120}, {1010}, {1012} and {1011} are insensitive to the well depths used in calculating electron densities for O^{2-} ions which were used in the electron gas calculations of the potentials. Also, Fowler and Tole (1988) compared the electronic structures of the O^{2-} and F^- anions (in MgO and LiF) at unrelaxed surfaces, steps and corners with those from bulk calculations, and found that anion polarisabilities increase with decreasing coordination, the rate of increase was much greater for O^{2-} but partially reduced by surface relaxation . The increase freedom for the electron density of an ion at the surface due to lower coordination, which is equivalent to a shallower Madelung well depth, is balanced by an increase in the electrostatic field at the ion site pulling the electron back into the solid. The effective size and shape of anions at the surface sites are very little different from those in the bulk. A similar conclusion was drawn by Causa et al. (1986). The transferability of potentials was also demonstrated by Mackrodt and Tasker (1989) who found a good agreement between calculated and experimental segregation energies of Ca at the surface of MgO, and of Mg and Y at the surface of α-Al_2O_3. However, different results are obtained in this study which have appreciable variation of calculated bulk defect energies with the Madelung well depth employed.

No single set of potentials with the Madelung depths considered reproduces acceptable properties for ceria as compared to potentials (1), (2) and (3). This is not surprising considering the approximations made in the simple model. The use of a formalism appropriate to the uniform electron gas and the omission of any variation of the wave functions of the interacting species with the interatomic spacing are obvious sources of error. Also more subtle errors arise from effects such as the inclusion of interactions between orbitals that are in fact symmetry forbidden in a more detailed quantum mechanical treatment (Duffy et al. 1992, Wood and Pyper 1981). Nevertheless, for dopant-oxygen interactions, these methods provide the only viable approach and enable us to derive Pd^{2+}-O^{2-}, Pd^{2+}-O^{2-}, Rh^{3+}-O^{2-} and Ce^{3+}-O^{2-} potentials, employing an oxygen Madelung well depth of 1.5 Hartrees. The potentials were subsequently empiricised using the Ce^{4+}-O^{2-} electron gas potential obtained for the same well depth following the procedure described in section (3.5.3). The resulting parameters are reported in table (3.6).

Table 3.6 **a)** Short range potential parameters $V(r) = A\exp(-r/\rho) - C/r^6$

Interactions	A (eV)	ρ (Å)	C (eV/Å^6)
O^{2-} - O^{2-}	22764.3	0.149	43.83
Ce^{4+} - O^{2-}	1986.83	0.35107	20.4
Ce^{3+} - O^{2-}	1731.61808	0.36372	14.43256
Pd^{2+} - O^{2-}	1145.21168	0.38335	32.50181
Pt^{2+} - O^{2-}	1541.41055	0.37292	25.07525
Rh^{3+} - O^{2-}	1404.42826	0.36482	13.12242

b) Shell model parameters $V(r) = k_1r^2 + k_2r^4$

	Y (|e|)	k_1 (eV/Å^2)	k_2 (eV/Å^4)
Ce^{4+}	7.7	291.75	0.0
Ce^{3+}	7.7	291.75	0.0
O^{2-}	-6.1	419.874	10000.0

3.8 Summary

In this chapter we have reviewed the various analytical forms that have been employed to describe interatomic potentials in solids. We have concentrated on pairwise interactions which have been successfully employed to model ionic systems, although we note that for systems with a higher degree of covalency, higher order terms must be included. For ionic systems, polarisation terms must be included in the calculation, which is successfully achieved by implementing the shell model. Two methods - empirical and electron gas - of deriving short range potential parameters have been described. Two existing sets of potentials for ceria are compared and contrasted which leads to a slight modification of one set to produce a more suitable set of potentials for the calculations of extrinsic defects in ceria. Finally short range potentials for precious metal ion - oxygen interactions have been derived using the modified electron gas method from a selected Madelung well depth for O^{2-}.

CHAPTER 4

SURFACES OF CERIA

4.1 Introduction

In this chapter, we employ simulation techniques to model the surfaces of ceria, paying special attention to the effects of these properties on catalytic activity. The first stage in investigating the surface properties of ceria is to study surface structure and energies. Low energy surfaces are generally more significant and will dominate the morphology of the material. Intrinsic defects in ceria such as the oxygen vacancy, which is known to play an important role in catalytic reactions and to be responsible for the oxygen storage ability of ceria (Yao and Yao 1984), will be investigated together with the migration mechanism and activation energies of the oxygen vacancy. Finally, the role of lattice oxygen and the oxygen vacancy in ceria in the oxidation of carbon monoxide will also be studied.

Ceria (chemical formula CeO_2) is the binary solid oxide of cerium which possesses the fluorite structure with each Ce^{4+} cation surrounded by eight equivalent nearest O^{2-} anions forming corners of a cube and each O^{2-} anion is surrounded by a tetrahedron of four cerium ions. The lattice can be described as a simple cubic array of oxygen anions, where half the cube centres are occupied by cations which are connected by edge sharing with lattice parameter of 5.411 Å.

The formation of a stable surface will occur only if the Madelung sums converge with increasing crystal size. This convergence only occurs when the crystal is electrically neutral and has no dipole moment perpendicular to the surface (Tasker 1979). Indeed, Bertaut (1958) showed that a dipole moment perpendicular to the surface would lead to an infinite surface energy. Such surfaces which include rocksalt (111) and fluorite (100) are unstable and are not observed without substantial reconstruction or adsorption of foreign ions to remove the dipole.

The necessity of substantial reconstruction, can be illustrated by considering the continuum approximation of the interaction between charged planes. The electrostatic potential at any plane P (figure 4.1.a) due to two planar sub lattices, of charge density of ± q/A and at a perpendicular distance z and (z+δz) respectively, reduces to a simple form in the continuum approximation, when z is greater than a few interatomic spacings (δz):

$$V(z) = +\left[\frac{2\pi}{A}qz\right] - \left[\frac{2\pi}{A}q(z+\delta z)\right] = -\frac{2\pi}{A}q\,\delta z \qquad (4.1)$$

For N sets of planes, the electrostatic potential increases without limit and is given by:

$$V(z) = -\left[\frac{2\pi q\delta z}{A}\right]N \qquad (4.2)$$

These types of surfaces are, following Tasker (1979), designated Type 3 surfaces. An example is the (100) surface of ceria.

A second case exists where the crystal is constructed of a neutral block of planes (figure 4.1.b). The potential at any plane P is given by:

$$V(z) = +\left[\frac{2\pi}{A}2qz\right] - \left[\frac{2\pi}{A}q(z+\delta z)\right] - \left[\frac{2\pi}{A}q(z-\delta z)\right] = 0 \qquad (4.3)$$

Here the contributions to the potential from the planes cancel for each neutral repeat unit and the potential becomes zero at large distances. These are designated Type 2 surfaces which are composed of charged layers but they form a charge neutral repeating stacking sequence which has a mirror plane parallel to the surface as is observed by the (111) surface of ceria.

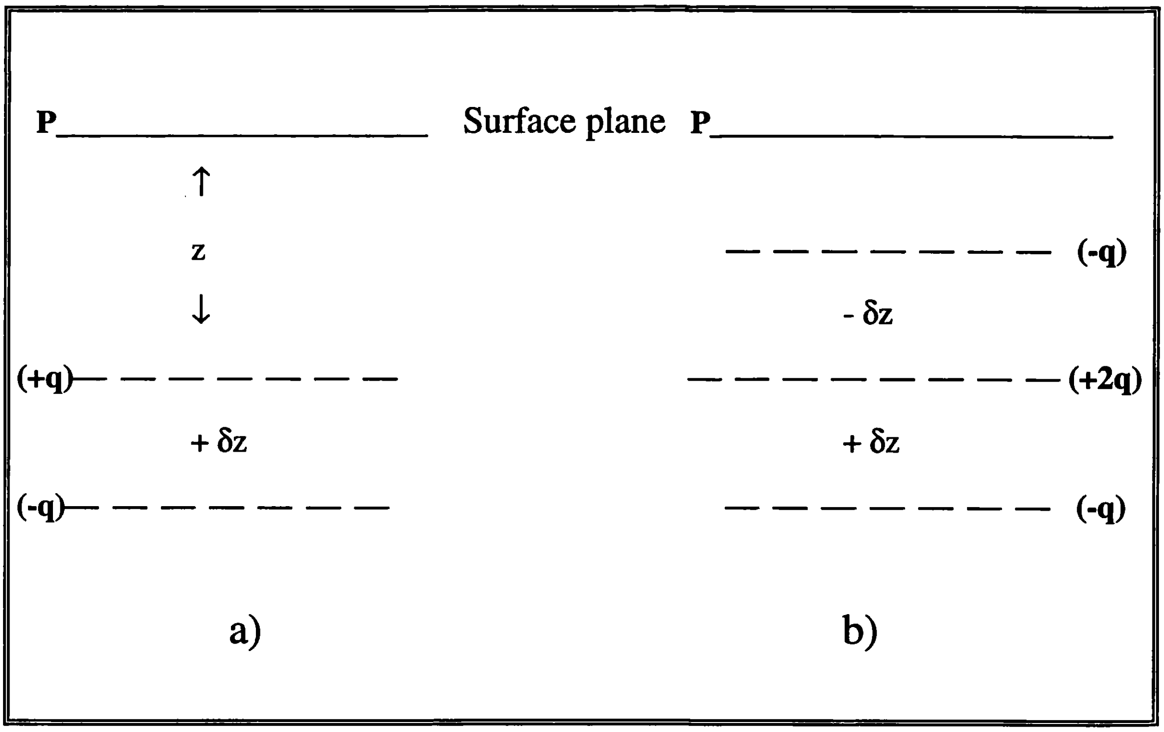

Figure 4.1 Schematic representation of two charged planes of **a)** type 3 and **b)** type 2 surfaces.

A final case exists where each individual plane maintains electroneutrality. These surfaces are designated Type 1 surfaces which are charge neutral with stoichiometric proportions of anions and cations in each plane (parallel to the surface). Examples include the (110) and (310) surfaces of ceria. For a type 1 surface, the potential for each plane is exactly zero due to the cancellation of the effects of the positive and negative charges.

We also note that the relaxation of a surface will result in the formation of a small dipole, the effect of which is independent of depth of the crystal; reliable interatomic potentials are crucial for the accurate calculation of the magnitude of this relaxation.

The above points are illustrated further in figure 4.2 showing three types of surfaces which are now discussed in more detail.

Type 1 is represented by the (110) and (310) surfaces of ceria; this type surface has an equal number of cations and anions on each plane. It has no dipole moment perpendicular to the surface and the potential (see equation 4.1) is zero for each plane. Additional neutral planes added to the surface, will make no contribution to the energy of the ions in the bulk of the crystal. The lattice sums required for the Madelung energy to converge at any ion site, require only a few planes either side of the site. Other examples of this surface include rocksalt (100) and (110) and the perovskite (100).

The type 2 surface is represented by the (111) surface of ceria. The surface terminates with a single anion plane and consists of a neutral three plane repeat unit and hence there is no dipole moment perpendicular to the surface. Each plane will contribute a term to the potential sum which cancels over the three plane repeat unit. Addition of further three plane repeat units to the surface will again make no contribution to the energy of the ions in the bulk of the crystal. This type of surface is similar to a type 1 surface, except that each repeat, has a finite thickness.

The type 3 surface is represented by the (100) surface of ceria. It consists of alternating charged planes which introduce a dipole moment perpendicular to the surface. These surfaces are unstable and are generally not observed in ionic crystals. CoO and UO_2 have been observed to accommodate type 3 structures. However, both these substances can support complex defect structures (Hall et al. 1985). Other example of this surface include the rocksalt (111).

Figure 4.2 Structural representation of four surfaces of CeO_2

Type 1 is illustrated by the (110) and (310) surfaces

Type 2 is illustrated by the (111) surface

Type 3 is illustrated by the (100) surface of ceria

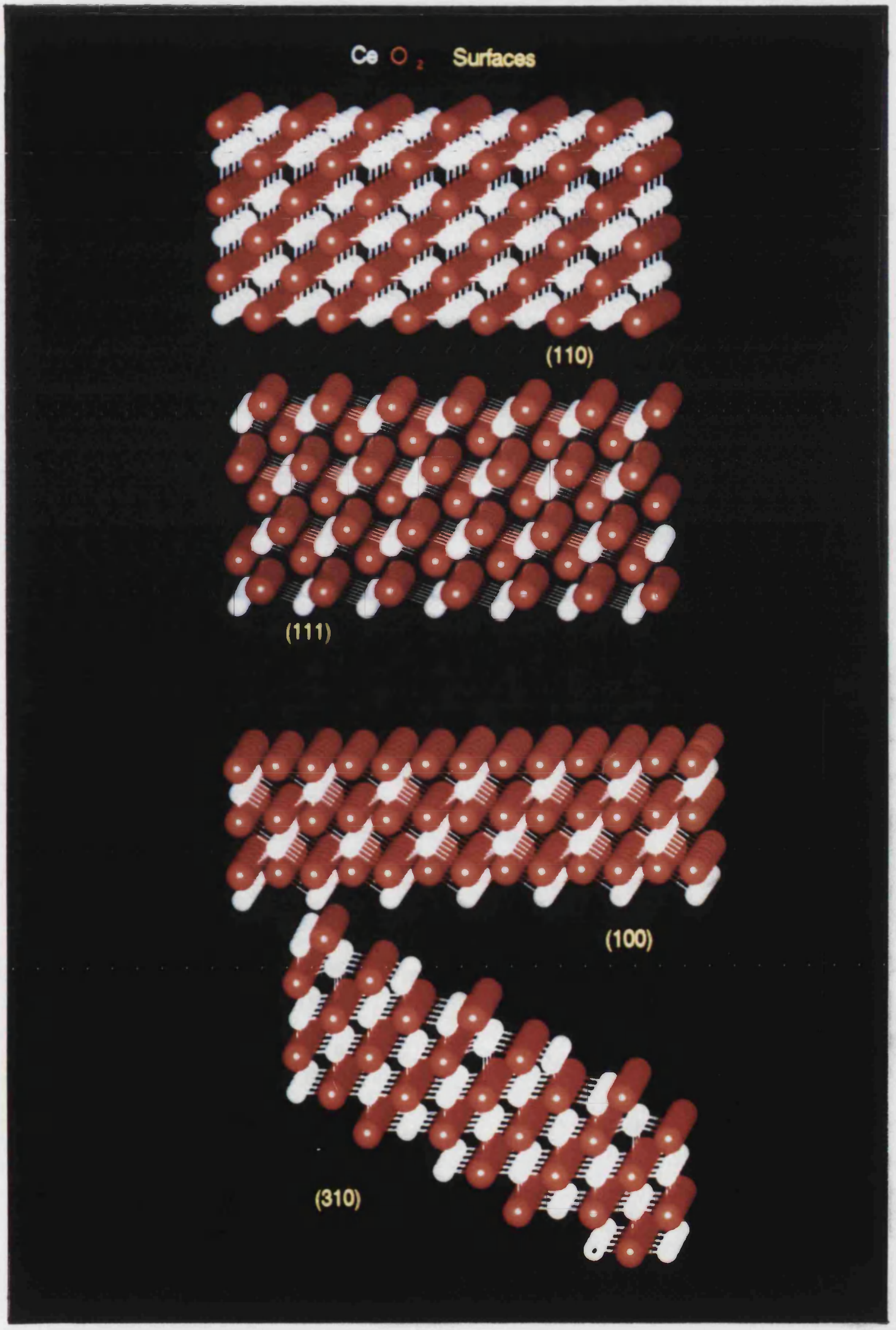

CeO₂ Surfaces
(110)
(111)
(100)
(310)

4.2 Pure surface energy calculations

The relative stability of surfaces described in figure 4.2 is studied by the use of the energy minimisation code MIDAS (greater details of which are given in chapter 2). MIDAS was used to model the (111), (110), (100) and (310) surfaces of CeO_2 with potentials (1) and (3) (chapter 3); their surface energies are subsequently calculated and compared. The (310) surface was chosen because it has distinct step sites which might be proposed as the active sites for dissociation or other reactions (figure 4.3). A very important feature of the techniques available in MIDAS is that ions are allowed to relax to their equilibrium energy configurations. (Mackrodt et al. 1987) has shown that the inclusion of lattice relaxation leads to modified surface energies and crystal mophologies in good agreement with experiment for $\alpha\text{-}Al_2O_3$ and $\alpha\text{-}Fe_2O_3$.

Surface energies of these surfaces are calculated by the following expression:

$$\gamma_s = \frac{E_s - \frac{1}{2}E_b}{A} \qquad (4.4)$$

where E_s = Energy of surface region (eV)

E_b = Energy of the perfect crystal (eV)

A = Surface area.

The calculation of the surface energy for the dipolar (type 3) surface (100) of CeO_2 is made possible by stabilising the surface with the inclusion of defects such as vacancies or addatoms. By transferring half the charge of the upper face of the block to the lower face, the electric field at the central plane is zero and hence the surface energy of the block is finite. This is illustrated in figure 4.4.

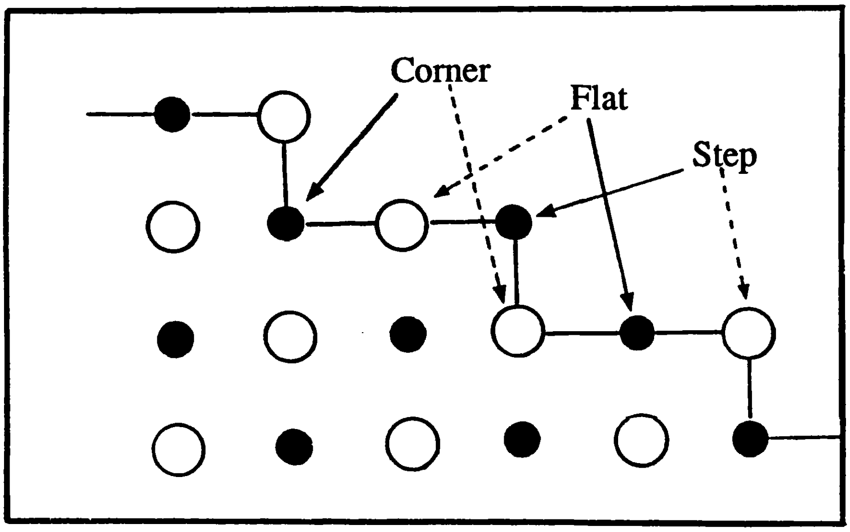

Figure 4.3 Diagrammatic representation of the (310) surface of ceria showing three distinct sites - step sites, flat sites and corner sites

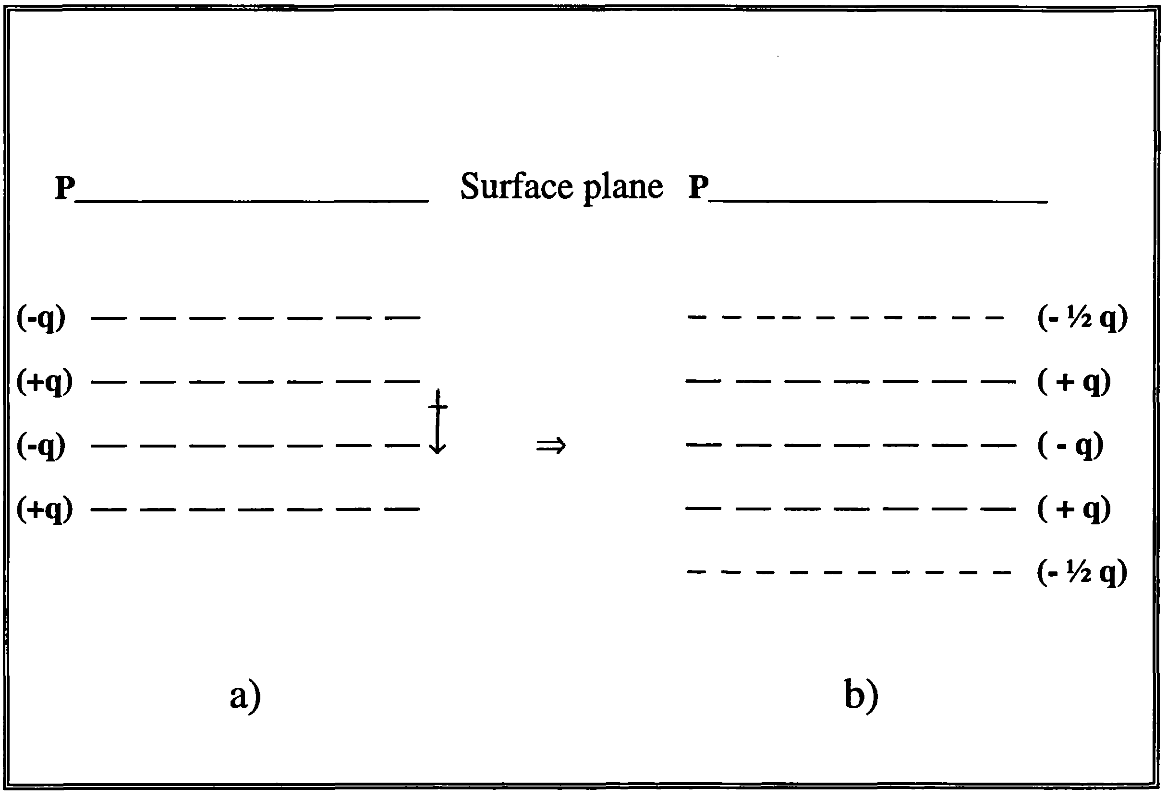

Figure 4.4 Schematic representation of stabilising a dipolar surface (a) by transferring charge from the surface to a lower plane (b)

It has been shown by Levine and Mark (1966) that charged surfaces of ionic crystals of general formula MX are less stable than the uncharged surfaces. For our CeO_2 surfaces, of general formula MX_2, the uncharged (111), (110) and (310) surfaces indeed are more stable than the charged (100) surface as shown by lower calculated surface energies after relaxation (table 4.1). The stability of surfaces follows the order: (111) > (110) > (310) > (100) which is applies both before and after relaxation. This order of stability remains the same for both potentials (1) and (3). However, there is a slight increase in the surface energies with potential (3) as a result of adding the C term to the short range potential of cerium which includes the interactions due to covalency, dispersion and van der Waals forces. These extra terms increase the attractive forces between cerium and oxygen atoms and therefore higher energies are required to form the surfaces. Potential (1) will be used throughout this thesis for the study of intrinsic defects in ceria such as oxygen and cerium vacancies whereas potential (3) will be used for the calculations involve extrinsic defects in ceria.

Table 4.1 Calculated surface energies of CeO_2 surfaces

Surface	Surface Energy (J/m^2)		
	Unrelaxed	Relaxed	
(111)	1.638	1.053	*Potential (1)
(110)	3.471	1.188	
(100)	6.226	3.109	
(111)	1.707	1.195	*Potential (3)
(110)	3.597	1.575	
(310)	11.577	2.475	

*Details of potential parameters are given in chapter 3

Table 4.1 shows that relaxation energies are substantial. The relaxed energies are ~30% lower than those for the unrelaxed (111) surface, ~60% lower for the (110) surface and ~80% lower for the (310) surface. Surface relaxation cannot therefore be omitted in any quantitative study of surface energies.

It is also observed that the more stable (111) surface exhibits smaller relaxation than the (110) surface as is clear from table 4.2 which compares the percentage ionic relaxations for the two lowest index neutral (111) and (110) surfaces of ceria as a function of distance (plane number) from the surface. Also, a comparison of ionic displacements at the surface planes only is illustrated in table 4.3 which includes the less stable (310) surface with the three distinct sites.

In table 4.2, a similar trend is observed for both surfaces. Cerium cations being smaller exhibit a greater relaxation compared to the more bulky oxygen anions. The relaxation of both cations and anions for both surfaces decreases with distance from the surface and approaches zero at the third repeat neutral layer for the (111) surface and at the 10th layer for the (110) surface. Clearly ions close to the (111) surface experience less strain than those for the (110) surface where both cations and anions are on the same plane, and where the relaxation extends further into the bulk than for the (111) surface.

The relaxation of ions on the surfaces can also be studied by comparing the displacement of ions on the surfaces of ceria.

Table 4.2 The percentage ion relaxations for ceria surfaces in the x direction (perpendicular to the surface). Negative values indicate that ions relax out of the surface whereas positive values indicate that the ions relax into the bulk of the crystal. The relaxations are calculated as percentage displacement relative to their interplanar spacing.

Plane Number	**Percentage Displacements**			
	(111)		(110)	
	Cerium	Oxygen	Cerium	Oxygen
1	3.9	-0.7	12.7	-2.5
2	-0.2	-2.7	-15.6	-0.6
3	0.0	1.0	7.2	-1.5
4		0.2	6.6	0.2
5		0.0	3.7	-0.7
6			- 3.1	0.1
7			1.8	-0.4
8			- 1.5	0.1
9			0.9	-0.2
10			- 0.8	0.0

Only very small displacements of ionic positions are observed for the (111) surface, due to lower strain on the surface plane where anions and cations are in separate planes. For the (110) and (310) surfaces where both cations and anions are in the same plane, higher ionic relaxations are observed resulting in a greater reduction on the surface energies. Again, in all cases, cerium cations experience more relaxation than oxygen anions. For the (310) stepped surface, ions on the surface include both cations and anions which are not closely packed; they therefore will relax in such as way to increase the surface ionic density. Thus, ions at the step sites which have low coordination show movements into the crystal whereas those at the corner sites show an outward movement, whereas ions on the flat sites on the surface show similar behaviour to the (111) and (110) surfaces - inwards for cations and outwards for anions.

Table 4.3 Percentage displacement of ions on the surfaces relative to interatomic distance. (Inward and outward movements refer to the movement of ions into the bulk and out of the surface respectively).

Surface	Ionic Relaxation				
	Cation		Anion		
(111)	4 %	Inward	0.7 %	Outward	
(110)	13 %	Inward	2.5 %	Outward	
(310)	45 %	Inward	0.1 %	Inward	**Step site**
	18 %	Inward	13 %	Outward	**Flat site**
	53 %	Outward	11 %	Outward	**Corner site**

On the surface energies after relaxation, we find that the (111) and the (110) have very similar energies, the difference between the energies of these two surfaces after relaxation being close to the limits of reliability of this method. We can not therefore say which surface is more stable. In contrast, the (310) step surface is unstable owing to a high surface energy which may result in it being more catalytically active. However, since it has lower stability we would expect that this surface will be present only in low proportions unless it is stabilised by defects. In the next section, we will investigate the effects of the defects on the surfaces and in the bulk of ceria.

4.3 Oxygen Vacancy Formation in Ceria

As discussed earlier, ceria is added to the automotive three-way catalyst as an 'oxygen storage' component in the automobile catalyst (Yao and Yao 1984, Gandhi et al. 1976, Yu Yao and Kummer 1987, Shyu et al. 1988). Thus ceria is able to provide oxygen for the oxidation of H_2, CO and hydrocarbons in the rich region of exhaust gas cycles, and to store oxygen in the lean region thus promoting conversion of nitrogen oxides. The reversible removal of oxygen from ceria is possibly due to the ease of changing oxidation states of cerium ions in ceria (i.e. the compound is non-stoichiometric) and to the mobility of oxygen in ceria.

To gain a more detailed understanding of this key effect, we need information on the formation energies of the oxygen vacancies in ceria. The calculated energies of formation for bulk defects in ceria are performed using the energy minimisation code CASCADE and for defects at and near surfaces using CHAOS (both codes being described in chapter 2).

4.3.1 Oxygen vacancy formation energy as a function of depth

Oxygen vacancies play a central role in the defect chemistry of CeO_{2-x}. However, oxygen vacancies in the bulk will not contribute directly to catalytic reactions which normally take place on the surface. We therefore need to study the stability of the oxygen vacancy at various distances from the surface.

The dependence of the oxygen vacancy formation energy on the distance from both the (111) and (110) surfaces is illustrated in figure 4.5 (and appendix 4). The formation energy of a vacancy in the bulk is included for comparison. All energies calculated by CHAOS are adjusted to account for the Madelung shift effect which as discussed in chapter 2 is required if we are to make proper comparison with the vacancy formation energies in the infinite bulk. The energies calculated for the oxygen anion vacancies refer to the first 10 planes for the (111) surface and the first 5 planes for the (110) surface.

As observed from figure 4.5, the energies of the oxygen vacancy increase with distance from both surfaces and converge to the bulk values at distances of ~ 22 Å into the bulk of the crystal. Oxygen vacancies are therefore more stable at the surfaces. We also observe that the formation energy of oxygen vacancies at the (111) surface which terminates with only oxygen anions is lower than that at the (110) surface, which is due to the extra energy required to overcome the attractive forces between anions and cations at the latter surface plane. The energies required to remove oxygen from the second plane of both surfaces are similar as ions now have the same coordination as those in the bulk; the surface effect is therefore reduced.

Clearly the formation of oxygen vacancies in ceria surfaces is thermodynamically more favourable than in the bulk. However, as ceria is used as an oxygen donor in catalytic processes, it is essential to examine not only the energy of oxygen vacancy formation but also the mobility of oxygen in the lattice, from which we may learn how easily oxygen ions from the lower layers may migrate to these surface vacancies - a vital process in catalytic reactions. Calculations of migration energies are reported next.

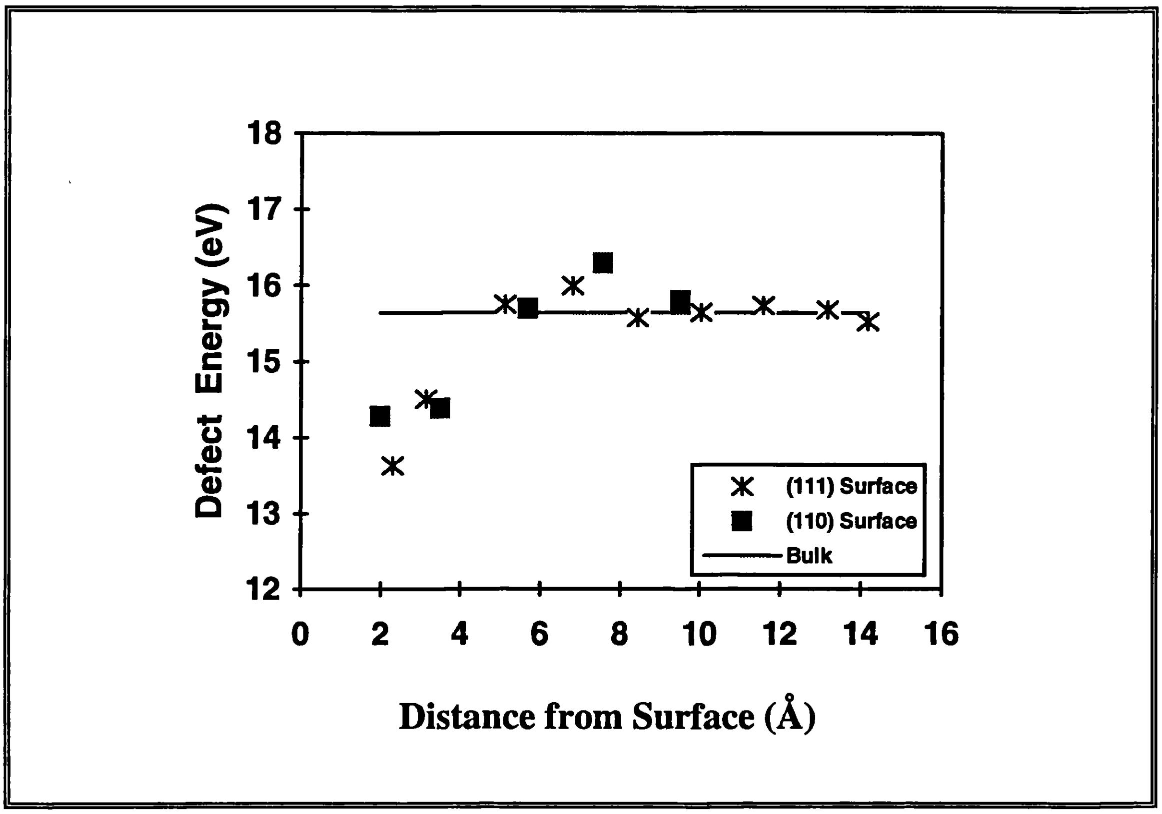

Figure 4.5 The variation of oxygen vacancy formation energy as a function of distance from the surfaces of ceria

4.3.2 Oxygen Vacancy Migration in the Lattice of Ceria

Figure 4.6 shows the migration of an oxygen vacancy in three different pathways from the (110) surface of ceria; all assume that the oxygen vacancy is following the shortest distance between its initial and final site. The mechanisms and calculated activation energies are summarised in table 4.4 and figure 4.6.

Table 4.4 Activation energy for different pathways of oxygen vacancy migration in the lattice of ceria.

	Pathway	Activation Energy (eV)
(a)	the nearest lattice site on the surface	1.00
(b)	the first nearest lattice site on the second layer	0.12
(c)	the second nearest lattice site on the second layer	0.21
(d)	oxygen vacancy migration in the bulk	0.36

The results summarised in table 4.4 and figure 4.6 show that oxygen migration across the surface (pathway a) requires the highest activation energy of 1.00 eV, and that the activation energy for a similar process in the bulk (d) is 0.36 eV; this refers to a <100> jump of the oxygen vacancy with a saddle point located where the migrating anion is equidistant from the two lattice sites involved in the jump, (points either side of the saddle point are also considered and proved to have lower energies). This indicates that it is more difficult for oxygen vacancy migration to occur on the surface compared with bulk of the crystal. Our result on the activation energy for the migration of the oxygen vacancy in the bulk of ceria is lower than the value of 0.53eV reported by Butler (1983). This could probably be due to the bigger region size used in our model, which is allowed by modern computer resources.

Migration of an oxygen vacancy from the surface into the bulk, however requires less energy than for both migration across the surface and into the bulk, as is illustrated by the calculated activation energies of pathways (b) and (c) where the oxygen vacancy is migrating from the surface layer to the lattice sites in the second layer. Notice that the migration of the oxygen vacancy to the first nearest neighbour site via pathway (b) does not have an activation barrier but an energy requirement of 0.12eV whereas pathway (c) necessitates overcoming a barrier of 0.21eV to the second nearest lattice site on the second layer. We note that the experimental activation energy of an oxygen vacancy hopping between trap sites at a second neighbour around Cd in CeO_2 is 0.55 eV (Su et al. 1990) in the temperature range of 77K to ~573K. This activation energy is expected to be higher than our result due to the contribution of extra attractive interactions with Cd which was not present in our calculated bulk value.

In summary, oxygen ions are less mobile in the bulk than at surfaces. Migration from the second layer to the surface layer is much easier and indeed requires very little activation energy (0.1 to 0.2 eV). The migration is expected to become more difficult on going from the third to the second layer and to increase further on going into the bulk until it reaches the bulk value.

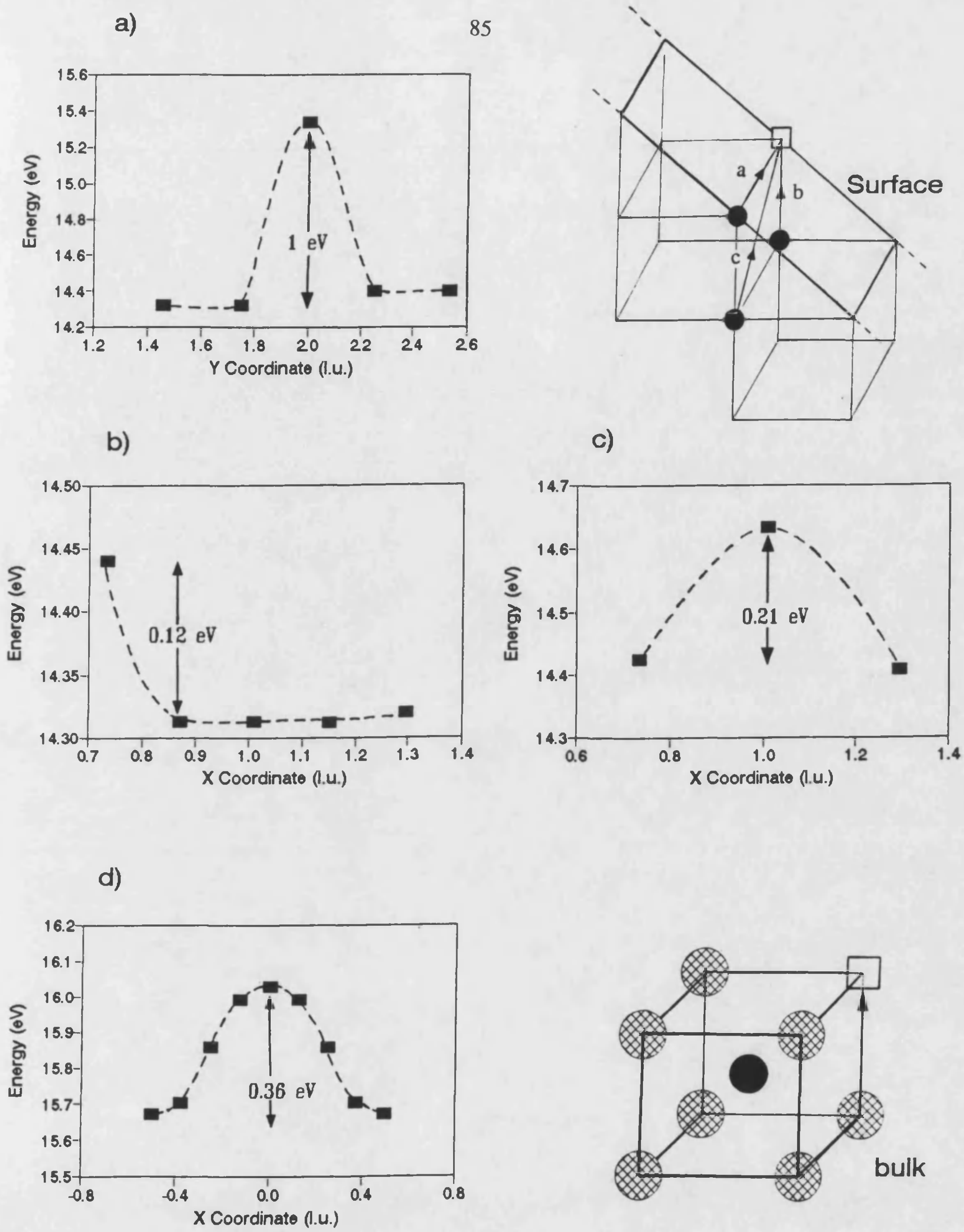

Figure 4.6 Activation energy of the migration of oxygen vacancy in three different pathways from the (110) surface of ceria, all assuming that oxygen vacancy follows the shortest distance to:

- **a)** the nearest lattice site on the surface
- **b)** the first nearest lattice site on the second layer
- **c)** the third nearest lattice site on the second layer
- **d)** the nearest lattice site in the bulk of ceria

4.4 Oxygen Vacancy Formation Energy and Its Role in the Oxidation of CO

We have noted that non-stoichiometry of ceria which arises from the fact that cerium can readily change its oxidation state enables the reversible addition and removal of oxygens which allows cerium dioxide to act as an oxygen storage material in oxidation reactions. We now therefore calculate the energy for carbon monoxide oxidation using oxygen donated from ceria, both from the bulk of the material and from the surface sites.

The relaxed structures of the three surfaces investigated earlier are used for the calculations of formation energies of the isolated defect including the oxygen vacancy and reduction of cerium species using CHAOS. The corresponding calculations were also performed for the bulk crystals using CASCADE. We next calculated the energies of the reduction for the reaction:

$$O^{x}_{O} + 2\,Ce^{x}_{Ce} \rightarrow V^{\bullet\bullet}_{O} + 2\,Ce'_{Ce} + \tfrac{1}{2}\,O_2 \qquad (4.5)$$

where, by Ce'_{Ce}, we represent the reduction form, Ce^{3+}. The results are presented in table 4.5.

Table 4.5 Defect equilibria for the carbon monoxide oxidation in ceria support

Defect Equilibria				Energy (eV)			
				Bulk	(111)	(110)	(310)
(a)	$2\ Ce^{4+}_L$	→	$2\ Ce^{3+}_L$	**73.91**	**70.45**	**68.36**	**63.55**
(b)	$2\ Ce^{4+}_\infty + 2\ e^-_\infty$	→	$2\ Ce^{3+}_\infty$	-73.52	-73.52	-73.52	-73.52
(c)	O^{2-}_L	→	$O^{2-}_\infty + V^{\cdot\cdot}_O$	**16.06**	**15.65**	**14.56**	**13.59**
(d)	O^{2-}	→	$O_\infty + 2\ e^-_\infty$	- 7.29	- 7.29	- 7.29	- 7.29
(e)	O_∞	→	$\frac{1}{2}\ O_{2(g)}$	-2.58	-2.58	-2.58	-2.58
(f)	**$O^x_O + 2\ Ce^x_{Ce}$**	→	**$\frac{1}{2}\ O_{2(g)}$ + $V^{\cdot\cdot}_O + 2Ce'_{Ce}$**	6.58	2.71	**- 0.47**	**- 6.25**
(g)	$CO_{(g)} + \frac{1}{2}\ O_{2(g)}$	→	$CO_{2(g)}$	- 2.93	- 2.93	- 2.93	- 2.93
(h)	**$CO_{(g)} + CeO_2$**	→	**$CO_{2(g)}$ + $V^{\cdot\cdot}_O + 2Ce'_{Ce}$**	3.65	**- 0.22**	**- 3.40**	**- 9.18**
	Binding Energy*			- 0.60	- 0.40	0.57	7.25
(h)	Cluster Effect**			3.05	**- 0.62**	**- 2.83**	**- 1.93**

* The difference between the formation energies of isolated defects and their corresponding neutral cluster

** Energy of reaction (h) with addition of binding energy

(a) Substitution energy of Ce^{4+} for Ce^{3+} in the lattice
(b) The fourth ionization energy of cerium
(c) Oxygen vacancy formation in the lattice
(d) 1st and 2nd electron affinity of oxygen
(e) Bond dissociation of oxygen
(f) Formation of oxygen molecule from cerium oxide
(g) Enthalpy of carbon monoxide oxidation
(h) Overall reaction

Three main points emerge from these calculations. First, the energies of the oxygen vacancy and the reduced Ce^{3+} are lower on the surface than in the bulk. Second, the energy of the formation of oxygen molecule from ceria (equation (f) in table 4.5) is more exothermic for both surfaces than for the bulk, showing that it is easier to abstract oxygen from the surface. In addition, the energies of reduction on the (110) and (310) surfaces are more exothermic owing to the lower oxygen vacancy formation energy and lower reduction energy. This behaviour may be correlated with the fact that the (110) and (310) surfaces are less stable and hence more active. While no direct comparison can be made with the calculated energies, a few experimental values for the relative partial molar enthalpy of bulk ceria oxygen atom have been reported to be 4.09eV at temperature, T = 1123K (Brauer et al. 1960), 4.467eV at T= (910-1440K) (Allas 1968), 4.77eV at T = 1353K (Campserveux and Gerdanian 1974, Tétot et al. 1987), and 4.98 ± 0.33eV at T = 1073 - 1273K (Chang and Blumenthal 1988) . The corresponding value at 0K would be expected to be higher and as such would be comparable to the bulk value of 6.58eV.

The inclusion of clustering brings the calculated values for the overall reaction of the (110) and (310) closer and more positive while those of the bulk and (111) surface become more negative. This is explained by the fact that ions in the bulk are closer and clusters are more closely bound whereas, on the surface, cluster binding decreases in order of decreasing stability, (111) > (110) > (310). With the inclusion of the cluster binding effect, the (110) surface has been shown to be the most active surface for the oxidation of carbon monoxide using oxygens donated from ceria.

The most important single result of this study is therefore the demonstration that the oxidation of carbon monoxide using oxygen from CeO_2 is favourable at the less stable (110) surface due to its high exothermic energy; the enthalpy for the reaction in the bulk is endothermic indicating an unfavourable reaction. Thus we predict that any processing conditions which favour the formation of the (110) surface will show this enhanced activity towards oxidation (figure 4.7).

Figure 4.7 Schematic representation of the oxidation CO using oxygen donated from the (110) surface of ceria

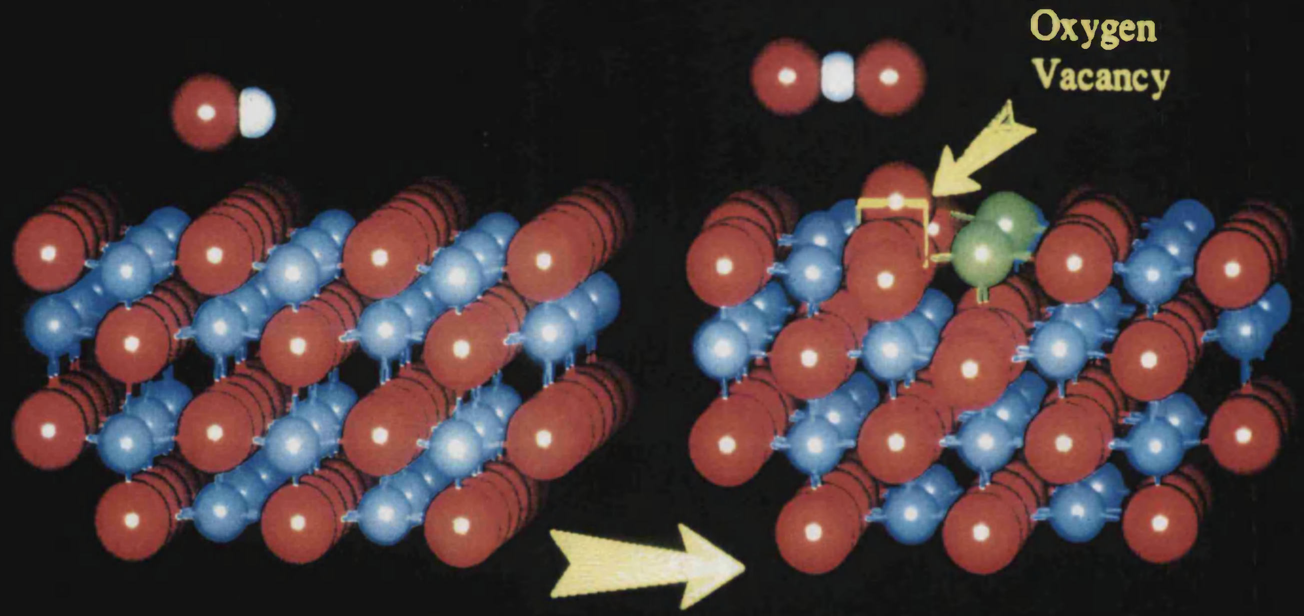

Oxygen
Vacancy

E = -3.4 eV

● Carbon

● Oxygen

● Cerium (IV)

● Cerium (III)

CHAPTER 5

THE INTERACTIONS BETWEEN PRECIOUS METAL IONS AND CERIA

5.1 Introduction

As discussed in chapter 1, the addition of ceria to ceramic supports of alumina and transition metals such as Pd, Pt and Rh has been shown to enhance the effectiveness of the three way catalyst reactions in automobile exhaust catalysis, whose importance lies in its ability to convert carbon monoxide, nitrogen oxides and hydrocarbons into non-toxic products. The role of ceria in the exhaust catalyst is complex and not yet clearly understood, although it is clear that variable valence plays an important role, which permits the reversible addition and removal of oxygens thus allowing cerium dioxide to act as an oxygen storage in oxidation reactions (Summers and Ausen 1979, Yu Yao 1984, Yao and Yao 1984, Gandhi et al. 1987, Oh and Eickel 1988, Shyu et al. 1988, Shyu et al. 1989). A comprehensive knowledge of the effects of impurity defect concentration on the behaviour of oxide material is therefore of critical importance in the design and the implementation of catalytic devices containing ceria.

The aim of this chapter is therefore to investigate the interaction of ceria with impurities, particularly rhodium, palladium and platinum. These precious metals have been shown to promote the reduction of Ce^{4+} to Ce^{3+} (Yao and Yao 1984). The presence of the metal on the ceria surface may facilitate a charge transfer from the metal to Ce which also results in a higher oxidation state of the precious metals. A study of the $Rh/CeO_2/Al_2O_3$ system by Oh and Eickel (1988) has shown that addition of CeO_2 decreases the apparent activation energy for CO oxidation and suppresses the inhibition effect of CO on the oxidation rate. They proposed a mechanism involving the reaction between adsorbed CO and lattice oxygen from the Rh/CeO_2 interface. Similar observations were made by Yu Yao (1984) for both CO and hydrocarbon oxidation.

The effects of adding CeO_2 to γ-alumina, studied by X-ray photoelectron spectroscopy (XPS), X-ray diffraction (XRD) and temperature programmed reduction (TPR) have shown that on heating in air at 800°C, Pt on both CeO_2 and CeO_2/Al_2O_3 yielded a platinum-ceria interacting species with an oxidation state of Pt^{2+}, attributed to PtO, which would be completely reduced to Pt metal by H_2 at 500°C (Shyu and Otto 1989). CeO_2 also promotes the oxidation of Pd to PdO at 800°C both with and without alumina. This lowers the rate of propane oxidation (Shyu et al 1988) and methane oxidation (Hicks et al. 1990). Thus when platinum and palladium are used under oxidising/fuel lean conditions, ceria promotes oxidation to the metal oxides that are poor catalysts for alkane oxidation. Hence, by adjusting the air/fuel ratio to the stoichiometric ratio we can ensure a high metal dispersion in alumina and maintain oxygen storage in automobile exhaust catalysis.

It is clear that the ceria stoichiometry and the oxidation state of the metals play an important role in the reactivity of the catalyst. However, the exact oxidation states of the precious metals when interacting with ceria is unknown. The energetics of the most common valence states for the metal atoms were therefore investigated in this simulation study. The variation of the energy with depth below the surface and the ability of defects to segregate to the surfaces of ceria were also studied. The simulation were carried out using standard procedures discussed in chapter 2, employing the energy minimisation codes CASCADE for the bulk, and the MIDAS and CHAOS codes for the surface simulations.

The reactivity of a surface depends on the defects and impurity species present. Impurity concentrations are strongly dependent on the segregation energies. The interactions of defects with these species may play an important role in determining surface active sites in processes such as oxidation and catalysis. Here, we consider the substitution energies of the aliovalent impurities Ce^{3+}, Rh^{3+}, Pd^{2+}, Pt^{2+} species and the formation energies of oxygen vacancies at both bulk and surface sites. Neutral clusters of these species were also considered.

The substitutions for aliovalent impurities Pd^{4+} and Pt^{4+} were also considered and shown to be unstable with respect to the Pd^{2+} and Pt^{2+} impurities. This can be demonstrated by considering the equilibrium reaction as follow:

For the (111) surface, the energy of the reaction in eV is illustrated below for palladium impurity,

$$\mathbf{E(Pd^{x}_{Ce}) + O^{x}_{L} \rightarrow E(Pd''_{Ce}) + E(V^{\bullet\bullet}_{O}) + \tfrac{1}{2}O_{2(g)}} - I_{Pd\,(II\text{-}III)} - I_{Pd\,(III\text{-}IV)} - E_{O\,(1st+2nd)} - \tfrac{1}{2}De_{\,(O\text{-}O)} \qquad (5.1)$$

$$-2.99 \rightarrow 58.94 + 15.65 - 32.93 - I_{Pd\,(III\text{-}IV)} - 7.29 - 2.58$$

$$-2.99 \rightarrow 58.94 + 15.65 - 32.93 - I_{Pd\,(III\text{-}IV)} - 7.29 - 2.58$$

$$-2.99 \rightarrow 31.79 - I_{Pd\,(III\text{-}IV)}$$

Where:

$E(Pd^{x}_{Ce})$: Substitution energy of Pd^{4+} for Ce^{4+} ion in ceria lattice
$E(Pd''_{Ce})$: Substitution energy of Pd^{2+} for Ce^{4+} ion in ceria lattice
$E(V^{\cdot\cdot}_{O})$: Formation of oxygen vacancy on surface of ceria
$I_{Pd\ (II\text{-}III)}$: The 3rd Ionisation energy of palladium
$I_{Pd\ (III\text{-}IV)}$: The 4th Ionisation energy of palladium
$E_{O\ (1st+2nd)}$: 1st and 2nd Electron affinity of oxygen
$De_{\ (O\text{-}O)}$: Bond dissociation energy of oxygen

As there is no reported value for the 4th ionisation energy of Pd, the energy of the above reaction can not be evaluated. However, by assuming this value to be at least 10eV greater than the 3rd ionisation energy for Pd, the total energy on the right hand side is more negative than that on the left hand side which indicates that Pd^{4+} substitution is unstable with respect to the Pd^{2+} substitution.

The energy for equation (5.1) for palladium at the (110) surface is $(-3.593 \rightarrow 12.8 - I_{Pd\ (III\text{-}IV)})$. Similar results were obtained for platinum at both surfaces.

5.2 Potential Model

Below are the short range potential parameters for the interactions between metal ions and oxygens (see chapter 3); the dopant-oxygen and cation-cation interactions are set to zero.

Table 5.1 a) Short range potential parameters $V(r) = A\exp(-r/\rho) - C/r^6$

Interactions	A (eV)	ρ (Å)	C (eV/Å^6)
O^{2-} - O^{2-}	22764.3	0.149	43.83
Ce^{4+} - O^{2-}	1986.83	0.35107	20.4
Ce^{3+} - O^{2-}	1731.61808	0.36372	14.43256
Pd^{2+} - O^{2-}	1145.21168	0.38335	32.50181
Pt^{2+} - O^{2-}	1541.41055	0.37292	25.07525
Rh^{3+} - O^{2-}	1404.42826	0.36482	13.12242
Pd^{4+} - O^{2-}	1639.70843	0.35011	0.0
Pt^{4+} - O^{2-}	2273.57111	0.34228	0.0

b) Shell model parameters $V(r) = k_1r^2 + k_2r^4$

	Y (|e|)	k_1 (eV/Å^2)	k_2 (eV/Å^4)
Ce^{4+}	7.7	291.75	0.0
Ce^{3+}	7.7	291.75	0.0
O^{2-}	-6.1	419.874	10000.0

5.3 Formation of Isolated Defects in Ceria

Table 5.2 presents a comparison of the formation energies of isolated defects in ceria including the substitution energies of Ce^{3+}, Rh^{3+}, Pd^{2+}, Pt^{2+} for the Ce^{4+} host cation. The energy of the oxygen vacancy (see also chapter 4) is also reported as it is the compensating defect. Both substitution and vacancy formation are less favourable in the bulk than at the surface. The substitution by divalent dopants requires, as expected, more energy than for the trivalent dopant cations. This is expected because of the mismatch in not only the difference in charge but also in the difference in ion size between host cerium ions (ionic radius = 0.92 Å) and substituting defects (0.80 Å for Pd^{2+} and Pt^{2+}, 1.034 Å for Ce^{3+} and 0.68 Å for Rh^{3+}).

Table 5.2 Formation energies (eV) of isolated defects in ceria

	Ce^{3+}	Rh^{3+}	Pd^{2+}	Pt^{2+}	$V_O^{\cdot\cdot}$	
Bulk	36.96	34.41	61.63	62.88	16.06	
(111)	35.22	33.59	58.94	59.25	15.65	
(110)	34.18	32.68	55.60	56.11	14.56	
(310)	**31.78**	**30.32**	**54.90**	**55.37**	13.59	Step
	36.68	34.63	61.06	60.86	**12.78**	Flat
	33.91	31.85	56.59	58.74		Corner

The surfaces show the same trend for all defects: the least stable stepped (310) surface which is likely to be the most active surface, requires the lowest energy for defect formation, whereas, the most stable (111) surface requires the highest energy. The oxygen vacancy formation energy for the surfaces studied decreases in the order of:

$$(111) > (110) > (310)$$

The results suggest that substitutions are easiest at the step sites which are also the most accessible. The Madelung energies calculated for the surface ions are significant lower than the value in the interior of the crystal. Illustrated below are the Madelung energies associated with the three different sites of the (310) surface (relaxed structure).

Table 5.3 Madelung energies associated with the three different sites of the (310) surface

Madelung energy (eV)		**Ce^{4+}**	**O^{2-}**
Bulk	site	-30.26	-8.14
Step	site	-21.55	-4.51
Flat	site	-26.46	-6.49
Corner	site	-33.28	-10.02

Sites with a more negative Madelung energy will result in a higher substitution energy for divalent or trivalent ions. For anions, the sites with the least negative Madelung energies are the easiest to be removed, i.e. those nearer to the surface.

5.4 Formation of Neutral Defect Clusters on the surfaces of Ceria

In this section, we will investigate the stability of neutral defect clusters in ceria. For cation substitutions, we use the step and corner sites which result in lower substitution energies (table 5.2) and for anion vacancies, the step and flat sites. On the (111) surface, the smallest neutral cluster is the one in which the defect impurities lie on the first plane of cations while the charge compensating oxygen vacancy is on the surface plane. In contrast, the atoms of the smallest cluster on the (110) surface all lie on the same surface plane. Three different clusters are investigated for the (310) surface based on the relative energies of the component isolated defects. Figure 5.1 shows the three combinations of sites: a) all defects come from step sites, b) cation defect substitutions are from step sites and the oxygen vacancy is from a flat site and finally, c) cation defect substitutions are from both step and corner sites and the oxygen vacancy is from a flat site.

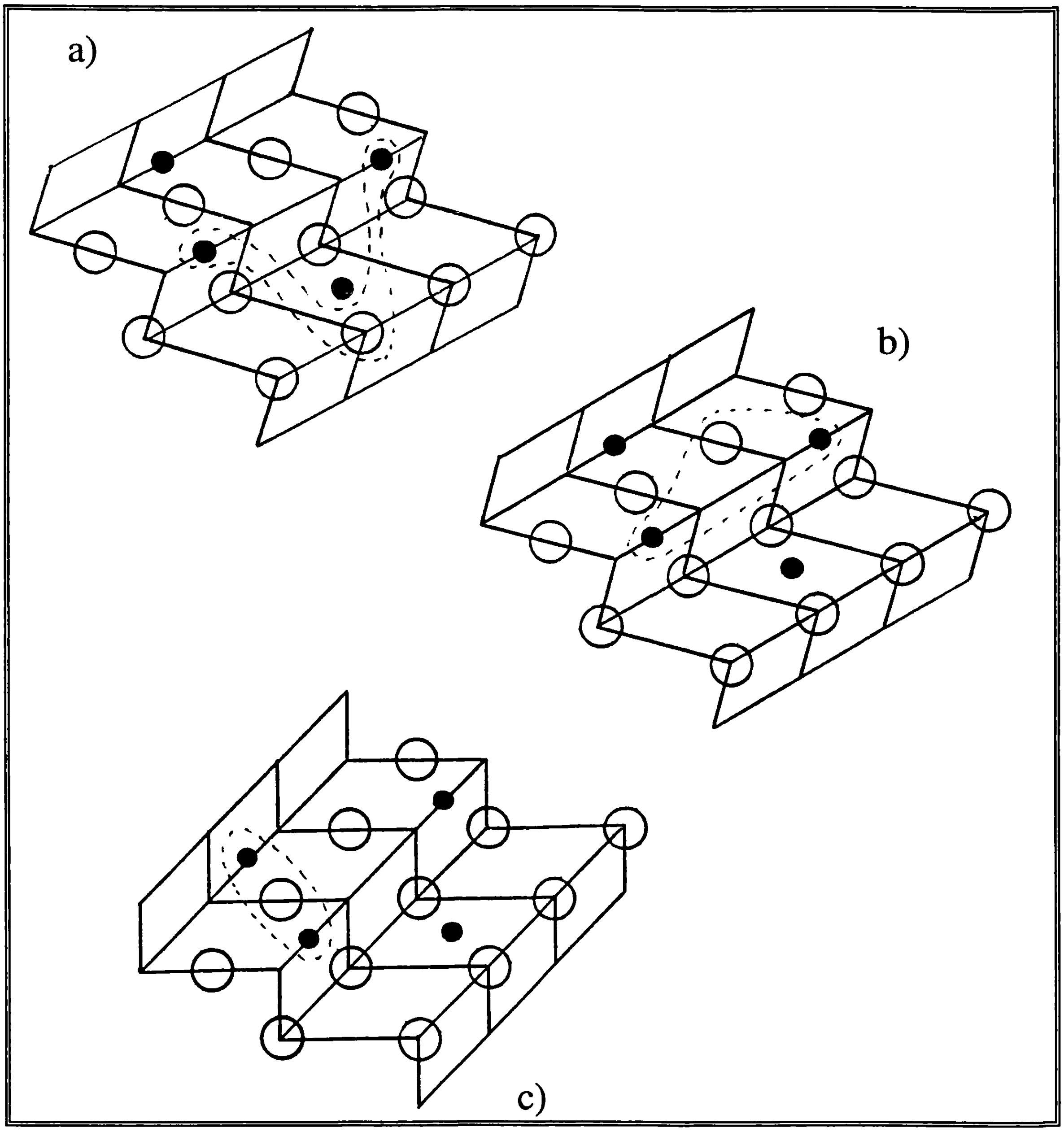

Figure 5.1 Schematic representation of three different combinations of sites in defect cluster calculation on the (310) surface of ceria:

a) all defects from step sites.

b) cation defect substitutions are from step sites and oxygen vacancy is from flat site.

c) cation defect substitutions are from both step and corner sites and oxygen vacancy is from flat site.

Table 5.4 gives the formation energies of the neutral defect cluster at the surface and in the bulk. Again, the formation energy of the clusters is lower at the surface than in the bulk. The table shows that the (110) surface is the most favourable for extrinsic defect cluster formations while the (310) is optimal for the reduction of cerium (IV) to cerium (III) - $[2Ce'_{Ce}\text{-}V^{\cdot\cdot}_{O}]^{x}$. Certain combinations of clusters in the (310) surface like the Rhodium cluster c), Palladium cluster a) and Platinum cluster b) show very similar energies to those at the (110) surface. This again supports the view that both (110) and (310) surfaces will be more catalytically active than the (111) surface, because the lower energy means that impurities will be concentrated at these sites. However, a further measure of their reactivity may be obtained by considering their binding energy, since if a cluster has a very high binding energy, the defect or impurity will be trapped preventing it from further chemical reactions.

Table 5.4 Formation energies (eV) of neutral defect clusters in ceria.

Cluster	$[2Ce'_{Ce}\text{-}V^{\cdot\cdot}_{O}]^{x}$	$[2Rh'_{Ce}\text{-}V^{\cdot\cdot}_{O}]^{x}$	$[Pd''_{Ce}\text{-}V^{\cdot\cdot}_{O}]^{x}$	$[Pt''_{Ce}\text{-}V^{\cdot\cdot}_{O}]^{x}$	
Bulk	89.36	84.23	76.48	77.71	
(111)	85.70	82.29	73.06	73.69	
(110)	83.48	**80.36**	**70.27**	**70.73**	
(310)	84.39	81.86	71.22	71.81	(a)
	80.11	82.12	71.35	**69.09**	(b)
	82.98	**79.72**			(c)

5.5 Binding Energy

The strength of the interactions between the components of a defect cluster is measured by its binding energy which is calculated as follows for the typical case of an oxygen vacancy binding to two Ce^{3+} substitutionals i.e.

$$\mathbf{2Ce'_{Ce} \quad + \quad V^{\cdot\cdot}_{O} \quad \rightarrow \quad [2Ce'_{Ce}\text{-}V^{\cdot\cdot}_{O}]^{x}}$$

$$\text{Binding Energy} \;=\; E\,[Ce'_{Ce}\text{-}V^{\cdot\cdot}_{O}]^{x} \;-\; 2E\,[Ce'_{Ce}] \;-\; E\,[V^{\cdot\cdot}_{O}]$$

The results of the calculations reported in table 5.2 for isolated defects and in table 5.4 for defect clusters are used therefore to calculate binding energies of the defect clusters with respect to their isolated components. Table 5.5 presents results for the defect clusters and for the binding energies of a cluster comprising an oxygen vacancy and reduced cerium ions in the bulk and at the two most stable low index surfaces of ceria. We note that the oxygen vacancy formation energy and the reduction of Ce^{4+} to Ce^{3+} take place most readily at the surface; the ions in the clusters are bound together at the (111) surface but not at the (110) surface. Aggregation is not therefore expected on the latter surface.

Table 5.5 Defect Formation Energy (eV)

	Bulk	**Surface**	
		(111)	**(110)**
$V_O^{\bullet\bullet}$	16.06	15.65	14.56
Ce'_{Ce}	36.96	35.22	34.18
$2Ce'_{Ce} + V_O^{\bullet\bullet}$	89.96	86.10	82.91
Cluster $[2Ce'_{Ce}\text{-}V_O^{\bullet\bullet}]^x$	89.36	85.70	83.48
Binding Energy	0.60	0.40	- 0.57

The binding energies for all clusters considered are summarised in table 5.6. We recall that a positive binding energy indicates a bound cluster and a negative energy indicates that the cluster is unstable with respect to the individual defects. Clusters in the bulk and at the (111) surface are therefore bound whereas those at the (110) surface are unbound. The (111) is a type 2 surface in which cations and anions are on two different planes; the cluster ions are therefore closer together compared to those at the (110) and (310) surface which are of type 1 in which ions are further apart in the same surface plane. For the step surface (310) which has three different types of sites, various combinations of the sites result in the cluster ions being closer together, but unbound cluster result owing to the high reduction in cluster relaxation.

Table 5.6 Binding Energy (eV)

	$[2Ce'_{Ce}\text{-}V^{\cdot\cdot}_{O}]^x$	$[2Rh'_{Ce}\text{-}V^{\cdot\cdot}_{O}]^x$	$[Pd''_{Ce}\text{-}V^{\cdot\cdot}_{O}]^x$	$[Pt''_{Ce}\text{-}V^{\cdot\cdot}_{O}]^x$	
Bulk	0.60	0.64	1.21	1.23	
(111)	0.40	0.54	1.53	1.21	
(110)	- 0.57	- 0.45	- 0.11	- 0.06	
(310)	- 7.25	- 7.63	- 2.73	- 2.86	(a)
	- 5.78	- 8.69	- 3.57	- 0.94	(b)
	- 4.52	- 4.76			(c)

The effects of surface relaxation energies also result in smaller clusters being more strongly bound than the bigger ones as a higher component of relaxation energy is lost in the latter. Indeed we note that the binding energies are twice or some cases five times higher for the di-ionic clusters, $[Pd''_{Ce}\text{-}V^{\cdot\cdot}_{O}]^x$ and $[Pt''_{Ce}\text{-}V^{\cdot\cdot}_{O}]^x$ than for tri-ionic clusters, $[2Ce'_{Ce}\text{-}V^{\cdot\cdot}_{O}]^x$ and $[2Rh'_{Ce}\text{-}V^{\cdot\cdot}_{O}]^x$.

The difference in surface and bulk binding energies is therefore controlled by a balance between steric strain due to the difference in ionic size (between defect impurity and host cations) and surface relaxation. A similar argument had been advanced by Mackrodt (1987) to account for the favourable segregation of Y^{3+} to the basal surface of $\alpha\text{-}Al_2O_3$.

5.6 Defect formation energy as a function of depth

Figure 5.2 shows the substitutional defect formation energies as a function of the distance from the (111) and (110) surfaces of CeO_2 for a) Ce^{3+}, b) Rh^{3+}, c) Pd^{2+} and d) Pt^{2+}. The horizontal lines in the graphs show the relative energies of the bulk defects for comparison.

We have already noted that for both surfaces, the substitutions are more favourable at the surface than in the bulk. All defects at both surfaces have the lowest energy on the surface which then increases monotonically towards bulk values. Thus all impurities and clusters will segregate to the surface under equilibrium condition.

The results on cluster binding energies in table 5.6 for defects of the neutral clusters $[2Ce'_{Ce}\text{-}V^{\cdot\cdot}_{O}]^{x}$, $[2Rh'_{Ce}\text{-}V^{\cdot\cdot}_{O}]^{x}$, $[Pd''_{Ce}\text{-}V^{\cdot\cdot}_{O}]^{x}$ and $[Pt''_{Ce}\text{-}V^{\cdot\cdot}_{O}]^{x}$ suggest that clusters need only be considered for the (111) surface while for the (110) and (310) surfaces, the highly negative binding energies indicate that defects will segregate to this surface as isolated ions (table 5.2).

In the next section, we will investigate the energies of defect segregation as a function of surface coverage.

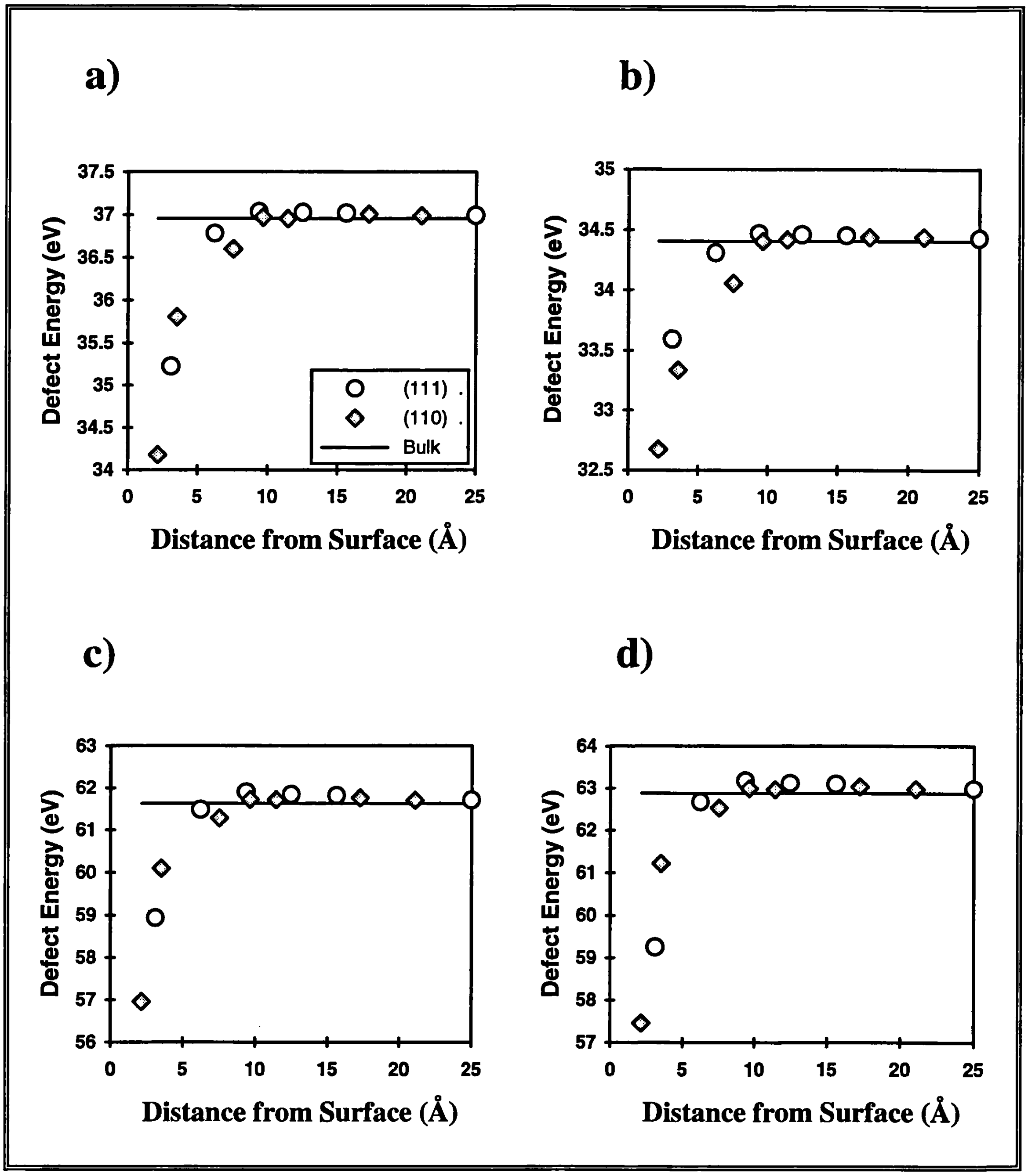

Figure 5.2 Defect formation energy as a function of distance from the (111) and (110) surfaces of ceria for **a)** Ce^{3+}, **b)** Rh^{3+}, **c)** Pd^{2+} and **d)** Pt^{2+}

5.7 Defect segregation to the surfaces of ceria

In this section, we will investigate the segregation of Ce^{3+}, Rh^{3+}, Pd^{2+} and Pt^{2+} to the (111) and (110) surfaces at five different coverages, 100 %, 75 %, 50 % 25 % and 0 %. All these defect substitutions are accompanied by oxygen vacancies to achieve charge neutrality on the surfaces. The cluster orientations are chosen so that all defect ions lie in the first cation plane and the oxygen vacancies are on the surface plane; this is to ensure the highest possible binding energy. The segregation of aliovalent defects posed a numbers of problems as the charge imbalance at the surface will cause interactions with the space charge layer. However, in all cases, neutral clusters are considered so that space charge effects do not directly influence the segregation. The segregation energies per defect are illustrated in figure 5.3 and tabulated in table A5.2 of appendix 5.

Several points can be drawn from these results for both surfaces:

The results not only reinforce our earlier conclusion concerning the strong segregation due to the negative segregation energies, but also show that the segregation does not exhibit Langmuir behaviour, where the segregation energy is independent of coverage. One exception is for the rhodium impurity at the (111) surface which shows a Langmuir-like segregation.

For the (110) surface, as the concentration of defects increases, the segregation energy decreases and reaches a minimum at 100% coverage. There is an decrease of 2.18eV for Ce^{3+}, 1.85eV for Rh^{3+}, 1.0eV for Pd^{2+} and 3.96eV for Pt^{2+}. From this we conclude that defects segregate at low concentration better than at high concentrations due to the rise in steric hindrance at the surface. This observation is in accord with the conclusions inferred from binding energy calculations in section 5.5.

The energies of segregation to the (110) surface are slightly more exothermic than those for the (111) surface. This can be explained by the fact that as the (110) surface is more dense than the (111), removal of oxygen vacancies may have a larger effect in reducing the elastic strain at the surface.

Also, as observed from the figure, the segregation energies for the M^{2+} cations are larger than for the M^{3+} cations as the total number of vacancies which accompanies the substitutions of M^{2+} is twice that for M^{3+} substitutions, which again helps to reduce the strain on the surface. In addition the binding energies of divalent clusters are higher than for trivalent clusters. As Rh^{3+} (ionic radius of 0.68Å) is smaller than cerium (0.92Å), and results in a lower segregation energy than Ce^{3+} (1.034Å), the main driving force is probably the reduction in elastic strain. The larger the defect the higher the tendency to migrate to the surface as the segregation is driven by the release of strain obtained by incorporating large ions at the surface rather in the bulk.

a) (111) Surface

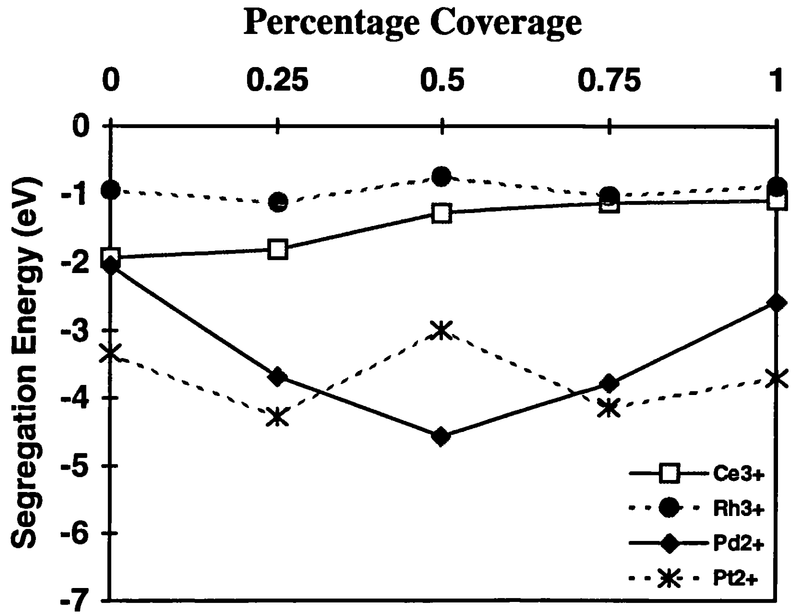

b) (110) Surface

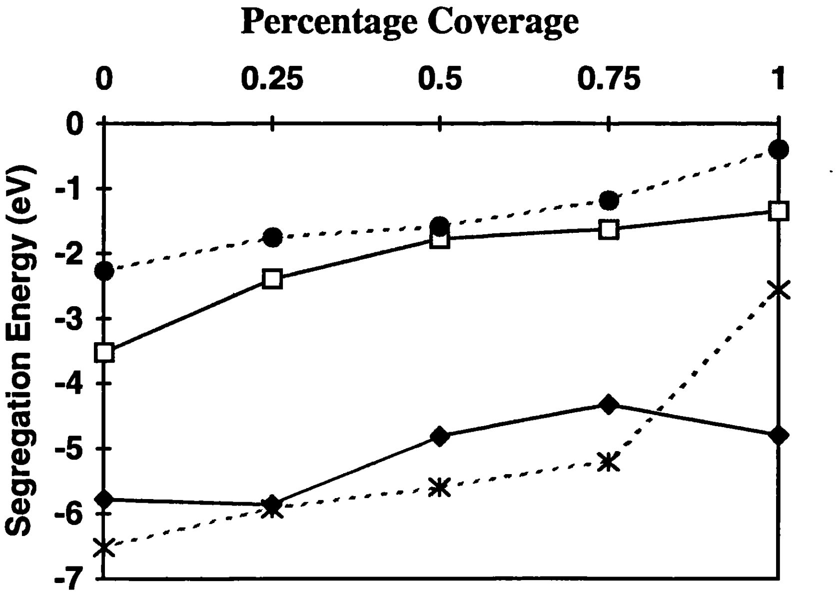

Figure 5.3 The calculated energies of segregation as a function of coverage for Ce^{3+}, Rh^{3+}, Pd^{2+} and Pt^{2+} at **a)** the (111) and **b)** the (110) surfaces of ceria.

Rather different results are obtained for the (111) surface where the energy of segregation of tri-valent defects does not vary much with coverage, and for di-valent cations, Pd^{2+} appears to have a minimum in the heat of segregation at approximately 50 % of a monolayer coverage; Pt^{2+} shows two minima at 25 % and 75 % monolayer.

Figure 5.4 illustrates the ionic relaxation at the (111) surface of ceria where half of the Ce^{4+} monolayer is replaced by Pd^{2+}. At the surface region, there is a substantial relaxation of ions resulting in an expansion of the surface structure. Both Pd^{2+} and oxygen ions relax outwards to form partial PdO clusters on the surface; there is also a smaller amplitude relaxation in the second layer of oxygens. As cerium ions are replaced by smaller Pd^{2+} ions, neighbouring lattice ions move from their original positions in order to release the lattice strain introduced by the ion size mismatch. The results shows that surface relaxation stabilises defect segregation.

To date, there is no experimental data with which we can compare our results, but the calculations reported above can be interpreted in terms of the formation of a stable coherent ordered second phase of the form $CePdO_3$ for palladium; and Ce_3PtO_7 and $CePt_3O_5$ for platinum. It is important to note that further calculations need to be done at more coverages before the exact coverage at which the minimum occurs can be located and hence an accurate composition for this second phase can be predicted. A similar case was observed for calcium segregation to the (111) surface of cubic ZrO_2. which reveal the presence of a stable phase $CaZrO_3$ (Dwivedi and Cormack 1989, Kenway et al. 1992).

Figure 5.4 Structural representation of ion relaxation for 50% coverage of $(\mathrm{Pd}''_{\mathrm{Ce}}\ \mathrm{V}^{\bullet\bullet}_{\mathrm{O}})$ segregation to the (111) surface of ceria.

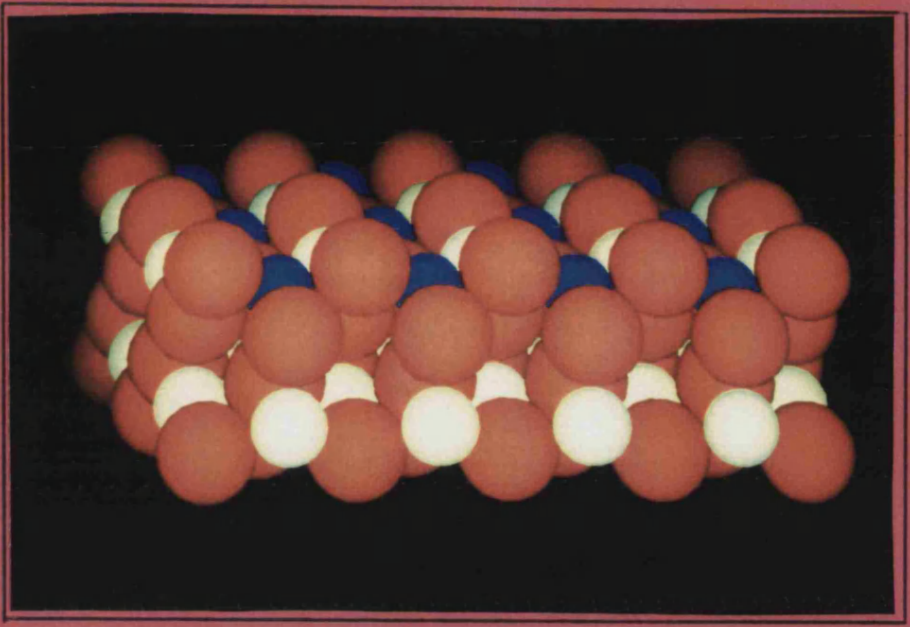

Before relaxation

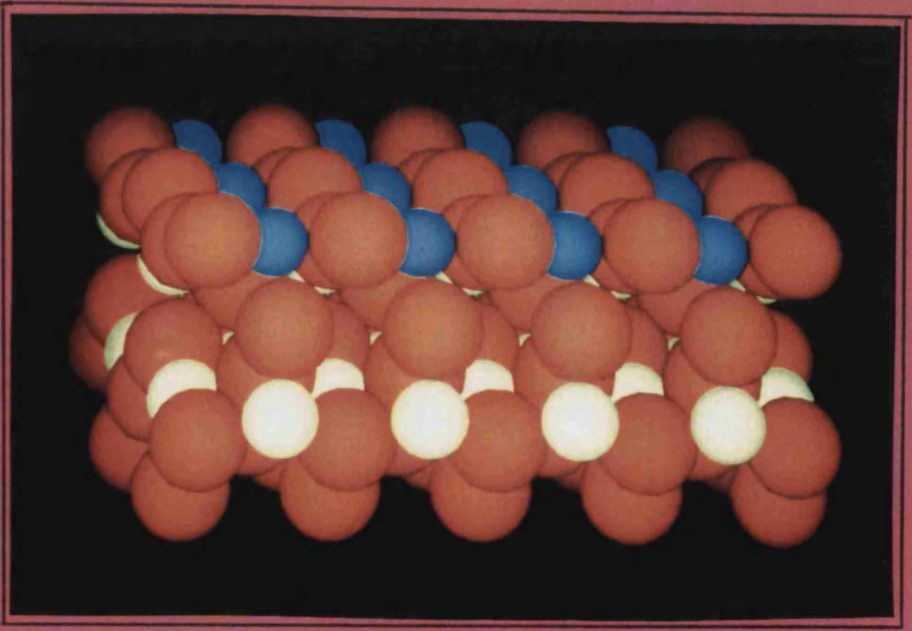

After relaxation

As ceria is used at low concentrations as a secondary oxide together with alumina in automobile exhaust catalysis, it is important to consider aluminium ion impurity in ceria. The segregation of equal proportions of Al^{3+} and Ce^{3+} defects to the (111) and (110) surface of ceria is illustrated in figure 5.5 and tabulated in table A5.2 of appendix 5. The charge on the surfaces is again balanced by the formation of an oxygen vacancy.

Unlike the observations in figure 5.3, figure 5.5 shows that higher concentrations of defects tend to segregate better than low concentrations on the (111) surface of CeO_2. Indeed the results for this surface indicate the favourable formation of a stable phase of the form $CeAlO_3$ at the (111) surface. The formation of $CeAlO_3$ has been observed as the results of the interaction between dispersed CeO_2 and γ-Al_2O_3 either reduced in H_2 at 800°C or under vacuum at elevated temperatures by Shyu et al. (1988), Geller and Racal (1970). Shyu et al. found that upon H_2 reduction, partial conversion of CeO_2 to surface $CeAlO_3$ occurs at 600°C and bulk $CeAlO_3$ at 800°. $CeAlO_3$ has a perovskite-like structure that is distorted from simple cubic perovskite form (Wyckoff 1967).

Some care should be taken when comparing the calculated results reported here with experiment, due to the approximations made in the model used. First, we assume that impurities segregate at planar and non-defective surfaces and second, we impose ordered arrangement of defects at all coverages. These assumptions may be an inaccurate representation of real systems. Nevertheless, the main conclusions regarding the segregation of impurities and the formation of surface phase are valid.

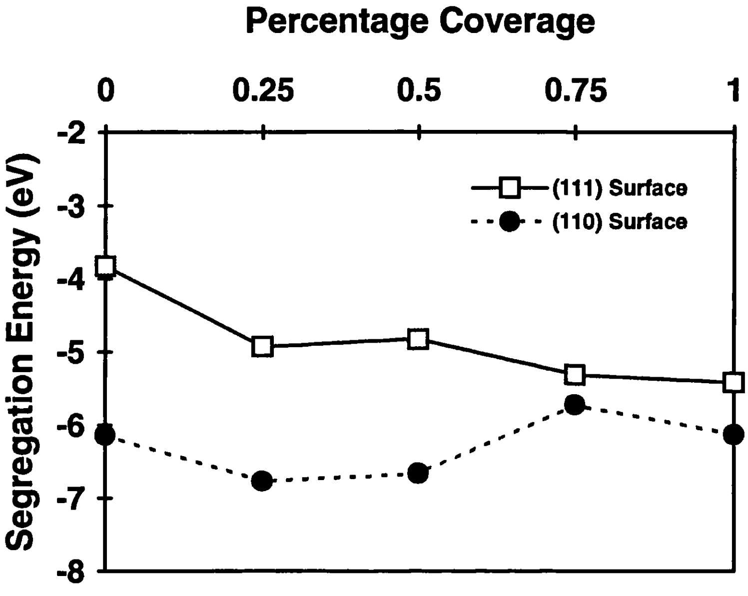

Figure 5.5 The calculated energies of segregation as a function of coverage for $[\mathrm{Ce}'_{\mathrm{Ce}}\text{-}\mathrm{V}^{\cdot\cdot}_{\mathrm{O}}\text{-}\mathrm{Ce}'_{\mathrm{Al}}]^{\mathrm{x}}$ at the (111) and (110) surfaces of ceria.

Most experimental techniques measure the temperature dependence of the surface concentrations that are assumed to be in equilibrium with the bulk. Heats or enthalpies of segregation are extracted from the plots of the log of surface concentration against reciprocal temperature. These are usually assumed to follow Langmuir behaviour:

$$\mathbf{C_s \propto C_b \exp(-\Delta h' / k_B T)} \qquad (5.1)$$

Where:

C_s : surface concentration
C_b : bulk concentration
k_B : Boltzman's constant
T : temperature
$\Delta h'$: coverage independent heat of segregation

Equation 5.1 is true for low concentrations of impurities, but as the concentration of impurity increases, there is an increase in defect-defect interactions which also plays an important rôle in determining the segregation enthalpies; thus non-Langmuir behaviour is expected. The results in figure 5.3 which gives segregation energy versus coverage show that the variation of segregation energy with dopant concentration is non-linear. This has also been confirmed by atomistic simulation work on isovalent and aliovalent impurity segregation in α-Al_2O_3 (Mackrodt and Tasker 1986, Mackrodt 1987 and Kenway 1989).

Mackrodt and Tasker (1986) have derived a coverage dependent segregation isotherm of the form:

$$x_s = x_b\, A \exp\left[-\frac{\Delta h + x_s(x_s+1)}{k_B\, T}\left(\frac{d\Delta h}{dx_s}\right)\right] \qquad (5.2)$$

x_s : surface atomic ratio, $x_s = n^s{}_1 / (n^s{}_1 + n^s{}_2)$, where $n^s{}_1$ and $n^s{}_2$ are the number of surface ions of type 1 and 2 respectively. This assumes there are 2 types of site in the crystal, surface and bulk.

x_b : bulk atomic ratio.

A : pre-exponential factor incorporating the entropy of segregation

$$A = \exp\left[-\frac{\Delta S + x_s(x_s+1)}{k_B}\left(\frac{d\Delta S}{dx_s}\right)\right] \qquad (5.3)$$

$d\Delta h/dx_s$ accounts for the change in the driving force for segregation as the surface defect concentration increases.

Using equation 5.2, the value of the surface coverage dependent heat of segregation Δh can be calculated from the slope of $\ln(x_s)$ against $^1/_T$ when experimental data are available.

This simple statistical model allows us to study the variation of segregation enthalpy with surface coverage for an impurity or defect monolayer. The model only applies to systems where the number of bulk sites are very much larger than surface sites and the bulk concentration of impurities is low thus satisfying the dilute solution limit, i.e. isolated non-interacting bulk impurity atoms.

In order to investigate the variation of surface coverage with temperature, the pre-exponential factor, A, for impurity segregation which corresponds to the vibrational entropy of segregation is taken to be unity; this assumes the segregation entropy is zero. The vibrational entropy of segregation is generally small and was shown to be small for the case of 50% coverage of Ca^{2+} at the (100) surface of MgO by Masri et al.(1986). It should also be noted that where experimental values of A are available, the agreement between experimental and calculated isotherm is excellent (Mackrodt and Tasker 1989).

The equilibrium surface coverages of Pd^{2+} are plotted against the reciprocal temperature at the (111) surface of CeO_2 in figure (5.6.a). The bulk concentration is taken as X_b = 200ppm which is equivalent to [0.02 $^{w}/_{w}$ % Pd, and 13 $^{w}/_{w}$ % Ce] (Summers and Ausen 1979). For Rh^{3+}, the bulk concentration of 145ppm (0.014 $^{w}/_{w}$ % Rh and 15 $^{w}/_{w}$ % Ce) is used (Oh and Eickel 1988) for the study of surface coverage as a function of temperature at the (111) and (110) surfaces of CeO_2 (figure 5.6.b).

Figure 5.6.a) shows that as the temperature increases from 900K the surface coverage of Pd^{2+} varies from ~70% to 64% of the (111) surface at 2500K. For Rh^{3+}, figure 5.6.b) predicts that in the temperature ranges from 500K to 2500K, the equilibrium coverage varies from 86% to 68 % of the (111) surface and from 63% to 17% of the (110) surface.

We have also investigated the calculated surface coverage as a function of temperature of the (111) and (110) surfaces of CeO_2 by $[\mathrm{Al}'_{Ce}\text{-}\mathrm{V}^{\cdot\cdot}_{O}\text{-}\mathrm{Ce}'_{Ce}]^{x}$ for a bulk concentration of 500ppm. We find that the surface layers are stable with 100% defect concentration, i.e. $AlCeO_3$ formation is favourable at all temperatures.

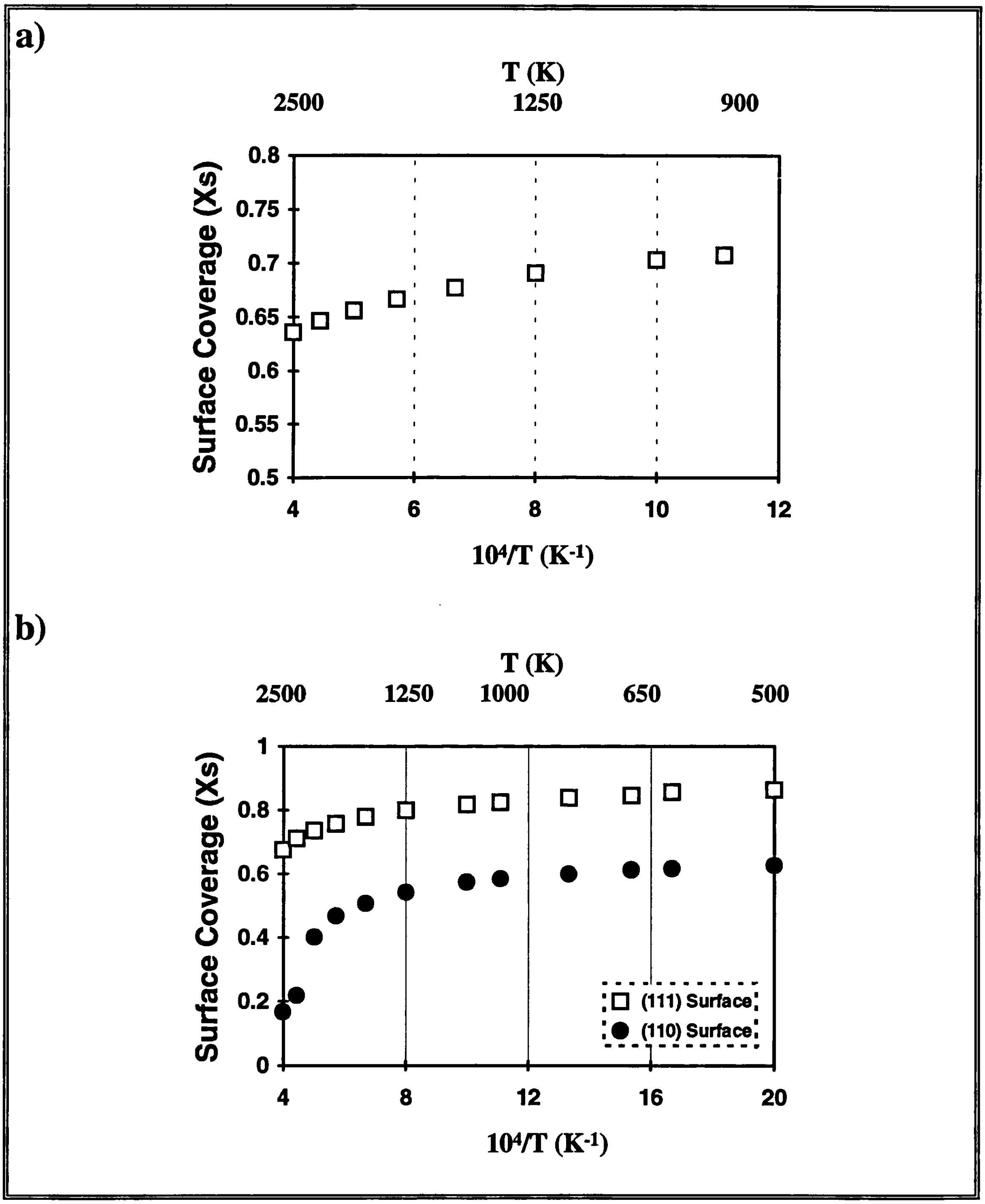

Figure 5.6 Calculated equilibrium surface coverage as a function of temperature of

a) Pd^{2+} at the (111) surface of CeO_2 for bulk concentration of 200ppm

b) Rh^{3+} at the (111) and (110) surfaces of CeO_2 for bulk concentration of 145ppm

Having demonstrated the effects of defect inclusion in ceria, the next step is to study the adsorption of gaseous molecules in particular CO and NO on the surface of ceria.

5.8 The adsorption of small gaseous molecules at ceria surfaces

5.8.1 Introduction

When an interface exists between metal catalyst and support oxide material, there may be a transfer of electrons and oxygen between the metal and oxide support which modifies the properties of the metal as a catalyst. This phenomenon together with the migration of the support onto the metal and stabilisation of metal dispersion against sintering are called the strong metal support interaction (SMSI). The effects of SMSI on chemisorption and catalytic properties have been investigated for several metals and supports such as Pt/TiO_2 (Herrmann 1984 and Horsely 1979), Pd/TiO_2 (Wang et al. 1981), Rh/TiO_2 (Resasco and Haller 1983), Pt/yttria-stabilised zirconia and Pt/Al_2O_3 (Metcalfe and Sundaresan 1986), and of course Pd, Pt, Rh/CeO_2. CeO_2 interacts with noble metals and greatly affects both the metal dispersion in alumina and the three-way conversion activities (Summers and Ausen 1979, Yao and Yao 1984, Binet et al. 1992). The mechanism of oxygen storage of ceria is believed to occur at the gas/noble metal/ceria interface, although the reaction of metals on the ceria surface and the roles of ceria in the catalytic chemistry are not well understood.

As discussed earlier, ceria enhances the rate of CO and hydrocarbon oxidation in fuel rich conditions by providing lattice oxygens (Yao and Yao 1984, Oh and Eickel 1988). However, under fuel lean conditions, it decreases the rate of CO oxidation over platinum and is relatively unaffected by Palladium and Rhodium (Summers and Ausen 1979). In this thesis, we only investigate the interactions of metals and the ceria promoter in conditions corresponding to a rich fuel where the oxygen vacancy formation in ceria plays an important role in catalytic reactions.

The addition of ceria has been found to affect significantly the kinetics of CO oxidation and NO reduction. The enhancement of CO oxidation can be explained on the basis of a mechanism involving CO_2 formation via a reaction between CO adsorbed on the metal and surface oxygen derived from the neighbouring ceria whereas the NO reduction is via the enhancement of NO dissociation and low temperature N_2 desorption due to the interaction between Ce and the metal. Several mechanisms have been suggested for the oxidation of CO, reduction of NO and CO-NO reaction under effects of ceria addition on an alumina-supported Rh catalyst (Zafiris and Gorte 1993, Oh 1990, Se H. Oh and Eickel 1988); Pt and Rh catalysts (Lööf et al. 1991); Pd and Pt catalysts (Summers and Ausen 1979); Pd catalyst (Shyu et al. 1988b); Pd, Pt and Rh catalysts (Yu Yao 1984). Jin et al. (1987) found that the reaction between absorbed CO on Pt in ceria with lattice oxygen to produce CO_2 (via an oxygen isotope exchange experiment) occurs readily at 400K.

In this work, we only consider the adsorption of CO and NO molecules on the (110) surface of ceria. The molecules are considered initially as vertically adsorbed with the negatively charged end of the molecule pointing to the oxygen vacancies formed on surfaces of ceria.

5.8.2 Potential model

In order to study these reactions, the interatomic potentials are required for the interactions between the absorbed molecules - C, N and O with CeO_2. The method of atom-atom potentials is used (Kieselev et al. 1985). The Lennard-Jones potentials are refitted to a Buckingham form before using in the simulations as the MIDAS code does not presently accept the former type of potential. Thus in the potential,

$$\Phi(r_{ij}) = \frac{B}{|r_i - r_j|^{12}} - \frac{C}{|r_i - r_j|^{6}} , \qquad (5.2)$$

where r : distance between centres of interacting atoms
C : constant of dispersion attraction
B : constant of repulsion,

the constant B was calculated from the equilibrium condition assuming that the equilibrium interatomic separation corresponds to the sum of the van der Waals radii (r_i and r_j).

$$B = \tfrac{1}{2}\ C\ (r_i + r_j)^6 \qquad (5.3)$$

The dispersion constant C in the Lennard-Jones potential is calculated using the formula below which is obtained from the Slater-Kirkwood relation (Hirshfelder et al. 1954).

$$C = \frac{3}{2} e^2 \sqrt{a_o} \frac{\alpha_i \alpha_j}{\sqrt{\frac{\alpha_i}{n_i}} + \sqrt{\frac{\alpha_j}{n_j}}} \tag{5.4}$$

Where α_i, α_j : the static polarisabilities of the interacting species

n_i, n_j : the number of electron in the atoms

a_o : Bohr radius (= 0.53 Å)

e : electron charge

The resulting parameters are reported in tables 5.7 and 5.8

The main assumption in deriving these potentials is that both oxygen and cerium ions in the ceria crystal which interact with the molecules are assumed to be in the gaseous state.

Table 5.7

Parameters for calculation of potentials of absorbate molecules and ceria

Atom	α (Å)	r (Å)	n	Y (lel)	Mass (a.m.u)
C(sp^1)	1.42*	1.80**	6	-0.0185	12.011
N	0.97*	1.55**	7	0.0278	14.0067
O	0.85*	1.52**	8		15.9994
Ce	2.93	0.92	7.9***	7.7	140.115

* Pauling 1958 and Vereshtshagin 1980

** Bondi 1964,

*** The effective number of electrons in cerium IV ion is taken as that of the nearest inert gas Xenon (Fowler et al. 1985) which was calculated by $16(C)^2/9\alpha^3$.

Table 5.8 Short range potential parameters $V(r) = A\exp(-r/\rho\ (\text{Å}) - C/r^6$

Interaction	A (eV)	ρ (Å)	C (eV/Å^6)
C - O^{2-}	23626.04511	0.2197	23.359
N - O^{2-}	11738.79587	0.2197	18.567
O - O^{2-}	10390.1782	0.2197	17.426
C - Ce^{4+}	23048.74728	0.2155	59.7188
N - Ce^{4+}	10313.12391	0.2197	60.1358
O - Ce^{4+}	7613.86527	0.2174	41.8846

For the intramolecular interactions (between the molecule themselves), the Morse potentials are adopted:

$$\Phi(r_{ij}) = D_e \{1 - \exp[-\beta (|r_i - r_j| - r_e)]\}^2 - D_e \qquad (3.3)$$

where D_e: the dissociation energy of the bond,

r_e : the equilibrium bond length

β : a variable parameter = $\omega_e[\mu\sqrt{(2D_e)}]$

μ : the reduced mass

The relevant parameters are reported in table (5.9)

Table 5.9

	D_e (eV)	r_e (Å)	μ (gmol^{-1})	ω_e (cm^{-1})
CO	11.108	1.1281	6.85841	2133.0
NO	5.290	1.0661	7.46881	2373.6

Herzberg (1950)

Ionic polarisability is needed for the calculation of the interionic van der Waals dipole-dipole dispersion coefficients of the short range interaction between interacting species. This yields the attractive part of the potential which plays an important role in large separations and thus contributes significantly to the total energy of the interaction. Although many potentials are approximately harmonic when close to the equilibrium configuration, there is no guarantee that they will remain so for larger distortions. The extreme is when the bond breaks.

5.8.3 Results and discussions

Table 5.10 illustrates the calculated energies of the adsorption of CO and NO molecules on to the oxygen vacancies of the (110) surface of ceria. We give separately the interaction energies, the difference between the energy of the molecule/defect ceria system and the sum of the energies of the two subsystems separately (tables 4.5, 5.2, and 5.9). and the bond length of the adsorbed molecules after relaxation.

Table 5.10 Energies of defect-molecule interactions

	Interaction	Energy (eV)	Interaction Energy (eV)	Bond length (Å)
(a)	$[V^{\cdot\cdot}_O\text{-CO}]^{2+}$	14.279	1.519	1.35
(b)	$[V^{\cdot\cdot}_O\text{-NO}]^{2+}$	14.418	**-4.438**	1.44

In general, the adsorption of NO at this surface results in negative interaction energies whereas the adsorption of CO are positive, indicating that NO adsorption is more favourable than CO adsorption using our model.

If we consider the bond length of the molecules after relaxation, in processes (a) and (b) where the molecules NO and CO are adsorbed on to a positively charged surface (resulting from the formation of oxygen vacancies), both NO and CO move vertically out of the surface and their bond distance increases to the cut-off value, i.e. 1.35Å for CO and 1.44Å for NO. This conclusion has been confirmed by repeating the calculations with the cut-off increased to 1.7Å, the results showed that bond length of both molecules increased to the increased cut-off value, i.e. the molecule is dissociating.

5.9 Summary

This chapter has demonstrated that by modelling impurity/defect formation and segregation to different surfaces of ceria, we can identify the ability of defects to stabilise the less stable surfaces such as (110) and (310). We have also shown that the noble metal cations - Rh^{3+}, $Pd^{2+}$and Pt^{2+} extensively segregate to the surfaces, a result which is clearly of significance for the catalytic activity of these materials.

The study of $[Ce^{3+}\text{-}V_0\text{-}Al^{3+}]^x$ segregation to the surfaces of ceria has shown that segregation is most favoured at 100% coverage of a monolayer of the (111) surface; this indicates the formation of $CeAlO_3$ which is compatible with the experimental results.

If the results are to be compared to experimental data, care must be taken with the assumptions and approximations made here. With regard to our surface model, we have assumed a planar surface and an ordered segregated structure which neglects the presence of irregularities (such as kinks, ledges and terraces), which would affect the heat of segregation. We also assumed that there are only two types of site, surface and bulk sites which in turn assumes that all segregated impurities resides solely on the surface plane. Nevertheless, despite these limitations, the main qualitative conclusions regarding the segregation of impurities and the formation of surface phases are valid.

The study of the adsorption of small gaseous molecules like CO and NO on the (110) surface of ceria has shown that NO adsorption is more favourable than the CO adsorption, the results illustrate the tendency for bond breaking between the NO molecule which is an important and possibly rate determine step in the dissociation of NO which leads to the its reduction.

CHAPTER 6

THE EFFECT OF DEFECT FORMATION AT THE INTERFACE BETWEEN CeO_2 (111) THIN FILM AND α-Al_2O_3 (0001) SUBSTRATE

6.1 Introduction

As described earlier in chapter 5, the 'three-way' automotive catalysts comprises of noble metals in conjunction with a support oxide which is constructed of an alumina substrate and an additional oxide ceria. Previous chapters concentrated on the effects of metal ions on cerium dioxide. We now continue with an investigation of the interactions between α-alumina and the most stable (111) surface of cerium dioxide. We note that γ-alumina in practice used as the catalyst support. However, owing to its complex surface structure, which has a disordered arrangement of aluminium cations surrounded both by tetrahedral and octahedral oxygens, it is difficult to model the surfaces. Work on the α phase provides method available primary study which will allow us subsequently to examine more complex systems.

In this chapter, we use the methodology that has been developed by Sayle (1992) for modelling ceramic heteroepitaxial interfaces at the atomic levels. This method was tested for a simple cubic system, BaO thin films on MgO substrate, and more complicated systems such as thin film superconductors. Many factors such as epitaxial constraints imposed on interfaces with high associated misfits, defects and dislocations, ionic interactions across the interface and relaxation have been found to contribute to the stability of the interface. The methodology developed by Sayle is modified in this work to study interfaces which accommodate hexagonal symmetry. We also calculate interfacial oxygen vacancy formation energies to investigate whether the effects of defect inclusion at the interfaces promotes the catalytic activity of ceria.

6.2 Surface Crystal Structure

Both $CeO_2(111)$ and α-$Al_2O_3(0001)$ surfaces exhibit a hexagonal surface structure, and CeO_2 (111) has been calculated to be the most stable low index surface (chapter 4). We note that α-$Al_2O_3(0001)$ has the corundum structure which consists of hexagonal close packed oxygen anions with aluminium cations in two-thirds of the octahedral sites, leading to six coordinate aluminium and four coordinate oxygen.

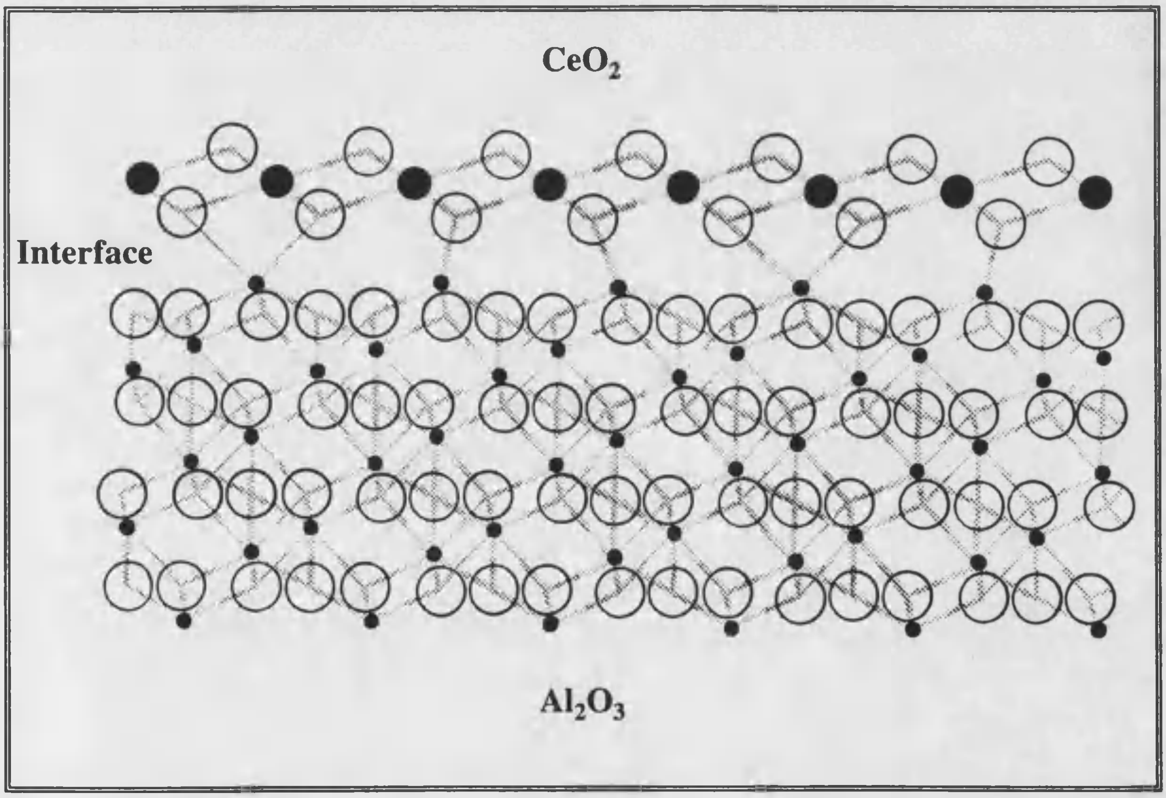

Figure 6.1 Schematic representation of an interface between the CeO_2 (111) surface and the α-Al_2O_3 (0001) substrate. Oxygen anions are big open circles, cerium cations are big closed circles and aluminium cations are small closed circles.

Figure 6.1 shows that both CeO_2 (111) and the basal structure of α-Al_2O_3 are of type 2 neutral surface (see chapter 4). While CeO_2 terminates with an anion plane, Al_2O_3 terminates at the cation plane. This arrangement of unlike charged planes of ions from the two materials at the interface may promote the formation or stability of the interface. For Al_2O_3, only one-third of the available surface cation sites are filled, and the ionic relaxation leads to a dramatic contraction of the free surface (Kenway 1989 and Mackrodt et al. 1987). An interface with ceria may reduce this contraction owing to the attractive interactions between the surface oxygen anions of ceria and the surface aluminium cations.

The lattice parameters of ceria and alumina are 2.7055Å and 5.128Å respectively. In CeO_2, the anions are roughly one and half the size of the cations, whereas in α-Al_2O_3 the anions are almost three times bigger.

6.3 Potential model

The potentials employed for modelling ceria are described in chapter 3 and those for alumina were derived by Lewis and Catlow (1985). Table 7.1 a) and b) give the potentials used for the calculations of energy associated with interfaces between ceria and alumina. The calculations of interfacial energies employed a rigid ion model together with short range potentials illustrated in table 6.1. The use of rigid ions is a consequence of the large number of ions in the primitive unit cell for some of the interfaces between hexagonal symmetry systems; even then not all the interfaces can be suitably accommodated within the available computational resources. For our studies of defect formation at the interfaces, the shell model potentials were employed to allow comparison with the calculations of defect formations at ceria surfaces of ceria. We note that polarisation is a major term in the defect energy and is therefore necessary in the latter calculations, whereas for the studies of the perfect interface, the polarisation is not expected to contribute significantly to the energy as the symmetry of the system is very high for CeO_2 and α-Al_2O_3.

Table 6.1

a) Short Range Potential Parameters $V(r) = A\exp(-r/\rho) - C/r^6$

Interactions			A (eV)	ρ (Å)	C (eV/Å^6)
O^{2-}	-	O^{2-}	22764.3	0.149	43.83
O^{*2-}	-	O^{*2-}	22764.3	0.149	27.88
O^{2-}	-	O^{*2-}	22764.3	0.149	43.83
Al^{3+}	-	O^{2-}/O^{*2-}	1474.4	0.3006	0.00
Ce^{4+}	-	O^{2-}/O^{*2-}	1986.83	0.35107	20.4
Ce^{3+}	-	O^{2-}/O^{*2-}	1731.61808	0.36372	14.43256
Rh^{3+}	-	O^{2-}/O^{*2-}	1404.42826	0.36482	13.12242

where O^{*2-} is the oxygen anion of alumina

b) Shell model parameters $V(r) = k_1r^2 + k_2r^4$

	Y_- (|e|)	**k_1** (eV/Å^2)	**k_2** (eV/Å^4)	Mass (a.m.u.)
Ce^{4+}	7.7	291.75	0.0	140.115
Ce^{3+}	7.7	291.75	0.0	140.115
O^{2-}	-6.1	419.874	10000.0	15.9994
Al^{3+}	1.458	1732.0	0.0	26.98
O^{*2-}	-3.0	60.78	10000.0	15.9994

6.4 The Near Coincidence Site Lattice theory

In this chapter we use a near coincidence site lattice theory (NCSL) to identify and construct interfaces with lower associated misfits. In conjunction with the energy minimisation technique available in the MIDAS code (chapter 2), the relative stabilities of these interfaces can be calculated explicitly. As noted the effects of defects such as oxygen vacancies and metal ion substitutions will also be studied.

Due to the mismatch in lattice constants that exists between any two materials, one material must be either contracted or expanded to match exactly to the other, i.e. to achieve a_0(overlayer) = a_0 (substrate). The resulting interfacial stability was found to be heavily dependent on the magnitude of this mismatch (Sayle 1992). The formation of a heteroepitaxial interface with configurations necessitating lower mismatches can be constructed using a near coincident site lattice theory which is a special case of coincidence site lattice theory (Bollmann 1970, Smith 1976, Grimmer 1974, Balluffi 1982, Sutton 1987, Mykura et al. 1980 and Gao 1988). This theory, based on purely geometrical criteria, has also been applied with success to explain the existence of many experimentally observed interfaces (Mykura et al. 1980, Gao 1988 and Hwang 1990). Recently the NCSL theory was applied to the cubic BaO(100)/MgO(100) system to investigate the variation of interfacial stability with percent misfit using energy minimisation methods (Sayle et al. 1993). This system is relatively simple and is a representative of a heteroepitaxial interface with an incommensurate relationship between the lattice parameters of BaO and MgO; furthermore the system has been investigated experimentally by Cotter et al. (1988) and therefore useful comparisons with experimental were made by Sayle et al. (1993).

The formation of coincident site lattice structures have been shown to be compatible with the observed experimental results. Mykura et al. (1980) showed that the preferred orientations for CdO/MgO interfaces correlates well with the Coincidence Site Lattice (CSL) model. Gao et al. (1988) studied the comparison between experimentally and observed low energy solid-solid interfaces and the special orientations predicted by CSL for MgO(001)/Ni(001) surface system. The [001] twist boundaries in MgO were investigated theoretically (Sayle 1992) and experimentally (Sun and Balluffi 1982). The results appeared to be consistent with the CSL model for grain boundaries which suggests that this model holds for grain boundaries in ionic solids.

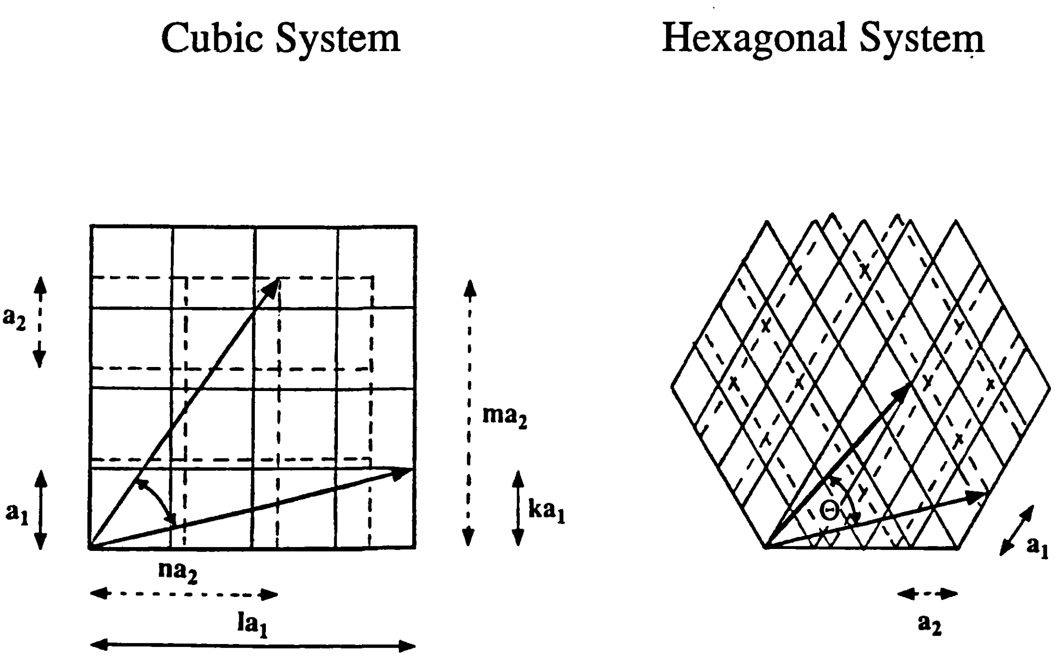

Figure 6.2 Schematic representations of the inter-phase boundaries of two materials with lattice parameters a_1 and a_2 for cubic and hexagonal systems. k, l, m and n are integers and θ is the rotational angle of one material with respect to the other.

6.4.1 The NCSL theory

The NCSL theory is a special case of the coincidence site lattice theory (CSL). The full three dimensional CSL theory for cubic crystals is given by Grimmer et al. (1974). In this section, we shall be concerned with the heteroepitaxial interfaces $CeO_2(111)/\alpha\text{-}Al_2O_3(0001)$. The theory will be first outlined for both simple cubic and hexagonal systems and then applied to construct interfaces with low associated misfits.

The inter-phase boundaries of two materials with lattice parameters a_1 and a_2 can be considered as two-dimensional square lattices for cubic systems and two dimensional hexagonal lattices for hexagonal systems. A two-dimensional coincidence site lattice is produced by rotating one lattice with respect to the other about the axis normal to the interface (figure 6.2) until three lattice sites of the two materials are in common. Exact coincidence occurs when

$$\left(\frac{a_1}{a_2}\right)^2 = \frac{m^2+n^2}{k^2+l^2} \qquad \text{cubic} \qquad (6.1.a)$$

$$\left(\frac{a_1}{a_2}\right)^2 = \frac{m^2+n^2+mn}{k^2+l^2+kl} \qquad \text{hexagonal} \; (6.1.b)$$

Where k, l, m and n are integers. The rotational angle associated with this coincidence site lattice to bring the two crystals into exact coincidence is:

$$\Theta = \tan^{-1}\left(\frac{n}{m}\right) \pm \tan^{-1}\left(\frac{l}{k}\right) \qquad \text{cubic} \qquad (6.2.a)$$

$$\Theta = \sin^{-1}\left(\frac{\sqrt{3}}{2}\frac{k}{\sqrt{k^2+l^2+kl}}\right) \pm \sin^{-1}\left(\frac{\sqrt{3}}{2}\frac{m}{\sqrt{m^2+n^2+mn}}\right) \qquad \text{hexagonal (6.2.b)}$$

The four fold symmetry of the square lattices and three fold symmetry of the hexagonal lattice ensure both positive and negative values of θ give equivalent interfaces and therefore only values between 0° and 45° need to be considered for cubic, and between 0° and 60° for hexagonal systems.

The density of planar coincidence sites Γ is defined as $(1/\Sigma_1{}^p)$ where $\Sigma_1{}^p$ is the planar reciprocal coincidence density of material 1 at the interface and is given by:

$$\Sigma_1{}^p = (m^2 + n^2) \qquad \text{cubic} \quad (6.3.a)$$

$$\Sigma_1{}^p = (m^2 + n^2 + mn) \qquad \text{hexagonal (6.3.b)}$$

$$\Sigma_2{}^p = (k^2 + l^2) \qquad \text{cubic} \quad (6.4.a)$$

$$\Sigma_2{}^p = (k^2 + l^2 + kl) \qquad \text{hexagonal (6.4.b)}$$

The superscript p is used to denote a planar two dimensional coincidence (Gao 1988). Exact coincidence only occurs when equation (6.1) is satisfied exactly (i.e. a_1=a_2). However, this relationship can never be satisfied exactly for heteroepitaxial systems. The incommensurate relationship between the lattice parameters (for all known lattice parameters) ensures that the left hand side of the equation (6.1) is irrational whilst the right hand side is always rational. Equation (6.1) can then be satisfied exactly if either one or both of the lattice parameters are changed i.e. if the crystals are expanded or contracted with respect to their optimum lattice parameter. This may be facilitated by matching the two materials at a particular temperature where the differences in the coefficients of linear expansion enable a particular NCSL to be in exact coincidence.

The misfit, F, which must therefore be accommodated by the expansion or contraction of the crystals is defined as the deviation from the exact coincidence condition, and designated a near coincidence site lattice. This misfit is given by:

$$F = \frac{2\left|a_1\sqrt{\Sigma_1^p} - a_2\sqrt{\Sigma_2^p}\right|}{\left(a_1\sqrt{\Sigma_1^p} + a_2\sqrt{\Sigma_2^p}\right)} \qquad (6.5)$$

A low value for the misfit resulting in a small loss in strain energy can always be achieved by increasing the size of Σ^p. However, this increase may cause the size of the resulting primitive unit cell to become too large even for modern computers to accommodate, and the density of planar coincidence sites, Γ, low. A low value of Γ is undesirable, since it has been suggested by Brandan et al. (1964) that low values of Γ are conducive to lower interfacial stability.

The size of the unit cell which we are able to accommodate within the present simulation work is limited and therefore we are compelled to ensure the primitive cell size is suitably small ($\Sigma^p < 20$). This would result in a high value of Γ but it is also likely to result in a high value for the misfit, F . A compromise between the value of the misfit and primitive unit cell size must therefore be sought.

6.4.2 Constructing interfaces using NCLS theory

We now apply a near coincidence site lattice theory to construct various $CeO_2(111)/\alpha\text{-}Al_2O_3(0001)$ interfaces, following which we calculate the relative interfacial stabilities based on the relaxed structures using minimisation techniques.

First it is necessary to calculate the lattice parameters of one to six layers of the overlayers of CeO_2. These values were then used to calculate the misfit using the NCSL theory. Such calculations are necessary as the thin films of overlaying material will exhibit a smaller lattice parameter than the bulk value. This is illustrated in figure 6.3 showing the variation of surface formation energies with lattice parameter for ceria. We find that the equilibrium lattice parameter for an isolated ceria monolayer is reduced by ~ 4.8% compared with the bulk value. This reduction decreases to 0.7% for six ceria layers, and if the number of layers is sufficiently high, the lattice parameter will reach the bulk value (table 6.2).

Table 6.2 Lattice parameters of ceria as a function of number of neutral layers

Number of Layers	**r** (Å)	% Reduction
1	2.5770	4.8
2	2.6480	2.1
3	2.6683	1.4
6	2.6875	0.7
Bulk (r_o)	2.7055	0.0

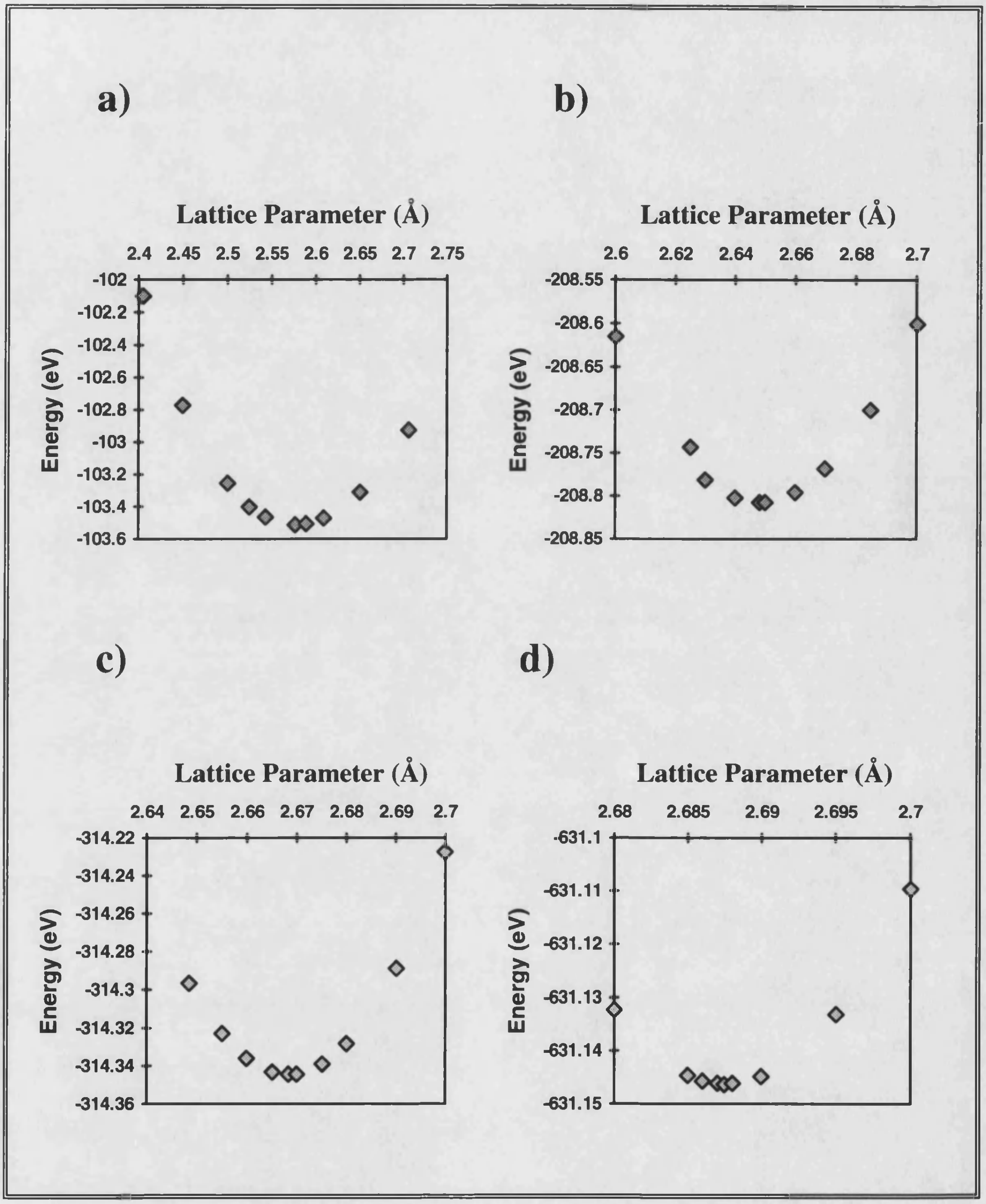

Figure 6.3 The variation of Surface formation energy with lattice parameter for **a)** monolayer, **b)** bilayer, **c)** three layers and **d)** six layers of ceria.

For monatomic square lattices, all the solutions of equations (6.1) and (6.2) are coincidence site solutions. Whereas for diatomic square lattices with the NaCl (100) planar structure (type 1 surfaces), certain values of h, j, k and l will also give a coincidence between two positive or two negative ions. From Mykura et al. (1980), these are designated 'anti-coincidence orientations' and they occur when one of Σ_1p, Σ_2p is odd and the other is even. The NCSL primitive unit cell with anti-coincidence orientations will be assigned 'β' in this work. Mykura also suggested that these systems do not give minima in the interfacial energy, as they have either two positive or two negative ions in close proximity, which will be expected to destabilise the interface. However, in this work Coulombic forces are fully included which will enable the like charged ions to relax away from each other and may result in stable β-type interfaces. Exact coincidence site orientations occur when both Σ_1p and Σ_2p are odd and therefore will have one positive ion site and one negative ion site in coincidence per primitive unit cell; these will be assigned 'α'. For the hexagonal system, $CeO_2/\alpha\text{-}Al_2O_3$, because each layer on either side of the interface contains only one type of ion, either anions or cations (type 2 surfaces - figure 6.1), there is no like charge repulsion between them within a close proximity; α therefore designates orientations when Σ_1p and Σ_2p are both odd or even, and β when one of them is odd and the other is even.

The interfaces predicted using the NCSL theory for $CeO_2(111)$ on α-$Al_2O_3(0001)$ are given in table 6.3; interfaces are identified by the nomenclature Σ_1p (overlayer) / Σ_2p (substrate). We note that positive values of F indicate that the overlayer must be expanded to accommodate the mismatch and negative values indicate that the overlayer must be compressed to accommodate the mismatch. Only interfaces with the misfit lower then 6% are considered, because interfaces with high misfits are found to be unstable (Sayle 1993) and therefore unlikely to exist.

Three common points emerge from these results. Firstly, when the overlayers must be expanded to accommodate the mismatch, the misfit decreases as the number of overlayers increases and when the overlayer must be compressed to accommodate the mismatch, the reverse applies. Secondly, we can see from table 6.3 that the misfit values start from high positive value (for expansion) then decreases until it changes to negative value (for compression), after which it increases again. This pattern is observed for all the of overlayers. Finally, as we increase the number of overlayers, the point of which there is a change from positive misfit to negative misfit also increases until n = 6 it is the same as the bulk value.

Table 6.3 Coincidence interfaces predicted for CeO_2 (111) on α-Al_2O_3 (0001) using a near coincidence site lattice theory.

$\Sigma^p CeO_2/\Sigma^p Al_2O_3$								% Misfit for n Layers of CeO_2 (10^2 F)				
		k	**l**	**m**	**n**	**θ /°**		**n = 1**	**n = 2**	**n = 3**	**n = 6**	**Bulk**
19/12	β	3	2	2	2	6.587		4.9	2.2	1.5	0.7	0.06
21/13	α	4	1	3	1	3.005,	35.209	3.9	1.2	0.5	**-0.3**	**-0.9**
31/19	α	5	1	3	2	14.465,	27.639	3.4	0.7	**-0.04**	**-0.8**	**-1.4**
61/37	α	4	5	3	4	1.045,	8.386	2.9	0.2	**-0.6**	**-1.3**	**-2.0**
61/36	β	4	5	0	6	26.330		1.6	**-1.2**	**-1.9**	**-2.7**	**-3.3**
12/ 7	β	2	2	1	2	10.893		1.0	**-1.8**	**-2.5**	**-3.2**	**-3.9**
7 / 4	β	1	2	0	2	19.107		**-0.06**	**-2.8**	**-3.6**	**-4.3**	**-5.0**
37/21	α	3	4	1	4	14.392,	23.822	**-0.4**	**-3.1**	**-3.9**	**-4.6**	**-5.3**
16/ 9	β	0	4	0	3	0.0		**-0.9**	**-3.6**	**-4.3**	**-5.05**	**-5.7**

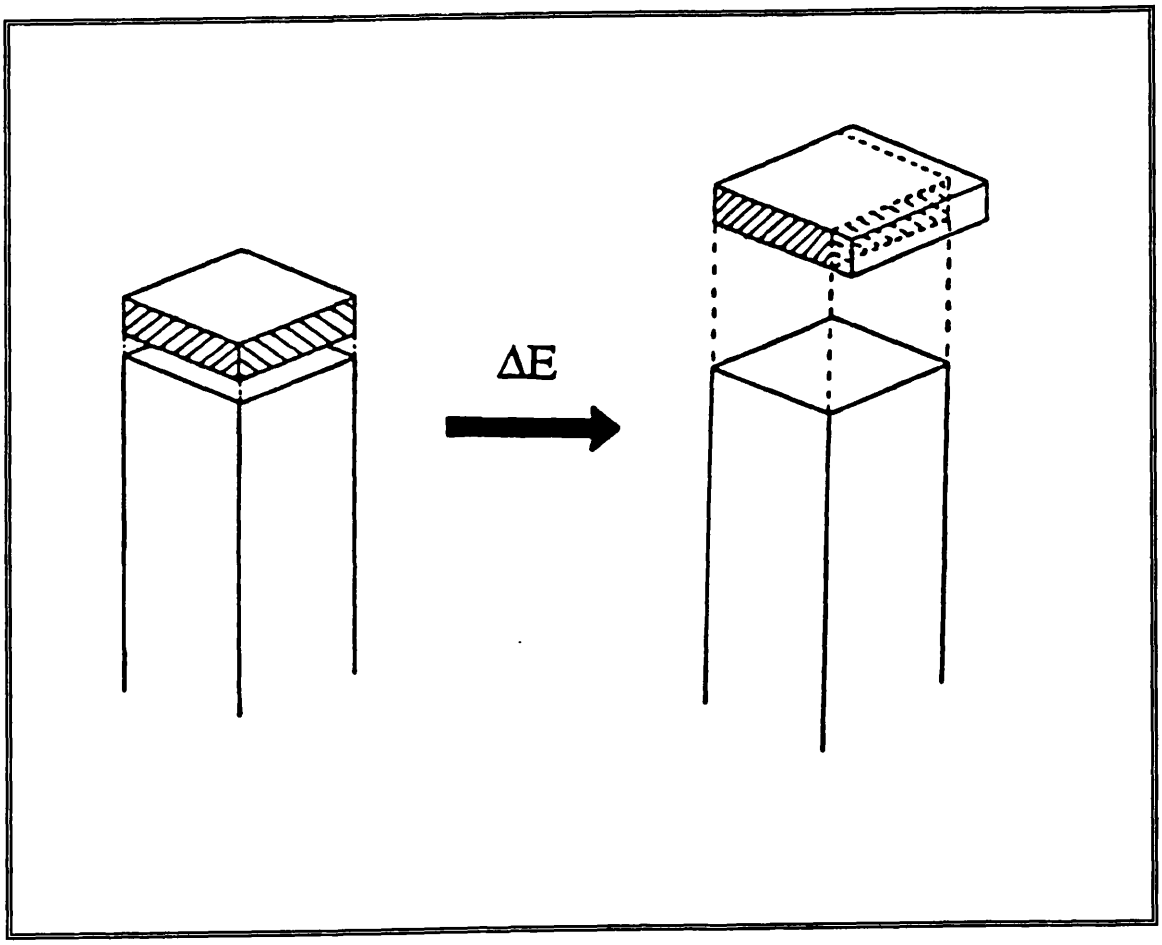

Figure 6.4 Diagrammatic representation of interfacial stability calculation

Table 6.4 Calculated stabilities after relaxation, for the $CeO_2(111)/\alpha$-Al_2O_3 (0001) interfaces predicted using a near coincidence site lattice theory for one to six CeO_2 layers on the Al_2O_3 substrate.

$\Sigma p_{CeO2}/\Sigma p_{Al2O3}$		θ /°	Interfacial Stability for n CeO_2 layers (J/m^2) **n = 1**	 **n = 2**	 **n = 3**	 **n = 6**
21/13	α	3°	1.453	1.419	1.244	1.560
	α	35.2°	1.246			
12/ 7	β	10.9°	1.794			
7/ 4	β	19.1°	1.574			
16/ 9	β	0.0°	1.954			

6.4.3 Factors influence the stability of interfaces

The calculated interfacial stabilities based on the relaxed structures of the interfaces given in table 6.3 for one to six CeO_2 overlayers, are presented in table 6.4 (the percent misfit is accommodated entirely by the ceria overlayer). The interfacial stability energy, ΔE, is defined as the energy per unit interfacial area required to cleave the interface to form an Al_2O_3 surface and a CeO_2 thin film each with its energy minimised lattice parameter (figure 6.4).

$$\Delta E = \frac{\left(E_{\text{overlayer}} + E_{\text{substrate}}\right) - E_{\text{interface}}}{\text{Area}_{\text{interface}}} \tag{6.6}$$

Only the interfaces which are believed to be reasonably stable based on those factors identified from the cubic system in previous work by Sayle et al. 1993, (i.e. low percentage mismatch, high planar density of coincidence lattice sites across the interface and low rotational angle), are considered here for CeO_2 thin films on an α-Al_2O_3 (0001) substrate. Also, as the size of the primitive unit cell of hexagonal systems is bigger than that for the cubic system, the high values of Σp can not be accommodated by the available computational resources.

High positive values of the energies indicate that all the interfaces considered are stable with respect to the isolated CeO_2 'thin film' and Al_2O_3 surface. This is attributed to the favourable attractive interactions between terminating ceria anions and aluminium cations at the interface.

For one layer of ceria, it is expected that the interfacial stability increases with decreasing mismatch as the strain energy required to accommodate the mismatch will destabilise the interface resulting in a maximum stability at the lowest value for the mismatch. This is observed in cases when ceria must be expanded (positive misfit) to accommodate the mismatch. However, when the ceria overlayer must be compressed (negative misfit), the interfacial stability increases with increasing mismatch. Indeed, the $\Sigma^p{}_{CeO_2}/\Sigma^p{}_{Al_2O_3} = 16/9\ \beta$ (0°) is constrained to accommodate a -0.9% mismatch, yet the interfacial stability after relaxation indicates this interface is the most stable for monolayer coverage with a stability of 1.954 J/m^2. This unexpected result can be explained by considering the effect of the relaxation of the interface which tries to reduce the strain energy in the system by allowing the ceria to relax in the direction perpendicular to the interface. The CeO_2 has initially been compressed to accommodate the mismatch and the 'excess' CeO_2 relaxes outwards to form a 'partial' second layer of oxygens on top of the surface. This type of behaviour is very pronounced for one ceria layer on the substrate, but for higher layer coverage, the reduced freedom of relaxational movement will prevent the overlayer from relaxing out of the interface region because of the layers above.

For the interfaces with $\Sigma^p{}_{CeO_2}/\Sigma^p{}_{Al_2O_3} = 21/13$ (3°), as the number of ceria overlayers increases, the freedom of ionic relaxation at the interface decreases which results in a decrease in the interfacial energy despite a decrease in misfit. A high interfacial stability is calculated for six layers of ceria on alumina because of a low misfit, whereas for the lower number of layers, the interface is stabilised by relaxation.

The results also show that for the $\Sigma^p_{CeO_2}/\Sigma^p_{Al_2O_3} = 21/13$ interfaces, the lower angle NCSL results in a more stable interface. This is consistent with the results found for cubic heteroepitaxial interfaces by Sayle et al. (1993). The results of Mykura et al. (1980) for CdO on MgO suggest that the frequency of occurrence of a NCSL with two associated angles is higher for the higher angle NCSL in contrast to our predictions. The resolution of the experimental results, however, may prevent two similar angle NCSL's from being adequately resolved and therefore attributing a higher frequency to an incorrectly assigned NCSL.

In summary, the interfacial energy cannot be determined purely by considering the percent misfit as other factors have been shown to contribute, including ionic relaxations at the interface and the rotational angle. In addition, as suggested by Sutton (1987) the higher planar density of coincidence sites (smaller Σ number) which results in the high density of favourable interactions across the interface is responsible for the increased interfacial stability. Experimentally, random deposition of thin film overlayers onto a substrate leads to the rotation of one material with respect to the other. This is due to the drive to minimise the interfacial energy with respect to the orientation of the film.

6.4.4 Relaxed structures of the interfaces

We now investigate the detailed relaxed structure of the interfaces between ceria and alumina detail of which are given in table 6.4. In all cases, the full number of ceria overlayers is shown, but only a few layers of the alumina substrate are displayed for clarity; also ionic relaxations are only appreciable within a few layers of the interface for the alumina crystal. Ion sizes are scaled to optimise the display, but their relative values remain constant.

Figure 6.5 shows the relaxed structure of the $\Sigma^{p}_{CeO_2}/\Sigma^{p}_{Al_2O_3} = 7/4$ ($\theta = 19.1°$) interface. The upper figure gives a projection across the interface whereas the lower one views the ceria overlayer with alumina underneath. It can clearly be seen that there is substantial relaxation of ions at the interface. Such relaxations reduce the strain introduced into the system when ceria is constrained to accommodate the misfit (-0.06%). After relaxation, the hexagonal symmetry of ceria oxygens within the primitive unit cell is retained (lower figure). But within each, the central oxygen relaxes outwards to form a partial layer on the surface (upper figure).

Figure 6.6 shows both the unrelaxed structure a) and relaxed structures b) and c) of the $\Sigma^{p}_{CeO_2}/\Sigma^{p}_{Al_2O_3} = 16/9$ ($\theta = 0°$) interface. Figures a) and b) view across the interface and c) views onto the ceria overlayer with alumina underneath. By comparing a) and b), we can see that due to the 0.9% compression of ceria initially to match the substrate, both ceriums and oxygens of ceria appear to relax outwards to form a partial layer, and those ions in the centre of the primitive unit cell are observed to relax more. This behaviour is predicted for interfaces with high negative misfit as ions within the unit cell will tend to relax away from each other and out of the surface to reduce the strain created by a high compressional mismatch. The ceria overlayer relaxes to form a regular array of triangles which in turn rearrange themselves to form hexagons (figure c).

Figure 6.7 shows the relaxed structure of the $\Sigma^p{}_{CeO_2}/\Sigma^p{}_{Al_2O_3}$ = 12/7 (θ=10.9°) interface. Again, the triangular arrangement of the relaxed ions is observed, but no hexagonal pattern is seen. The pattern of the relaxed ion positions in the $\Sigma^p{}_{CeO_2}/\Sigma^p{}_{Al_2O_3}$ = 16/9 and the $\Sigma^p{}_{CeO_2}/\Sigma^p{}_{Al_2O_3}$ = 12/7 structures bear some similarities to each other. However, they depend on sign of the misfits, the size of unit cell and also angles of rotation as illustrated in figure 6.8 for the $\Sigma^p{}_{CeO_2}/\Sigma^p{}_{Al_2O_3}$ = 21/13 structure.

Figure 6.8 shows the relaxed structures of the $\Sigma^p{}_{CeO_2}/\Sigma^p{}_{Al_2O_3}$ = 21/13 with two different associated angles θ = 3° (upper) and θ = 35.2° (lower). The figure shows a projection across the interfaces with a CeO_2 monolayer on an Al_2O_3 substrate. Despite the fact that both interfaces have the same misfit, the resulting relaxed structures bear some differences from each other. For the higher angle interface, the ceria overlayer appears to form small isolated clusters within the primitive unit cell size. This is generally a consequence of high positive mismatch between ceria and alumina.

Figure 6.9 shows the relaxed structures of the $\Sigma^p{}_{CeO_2}/\Sigma^p{}_{Al_2O_3}$ = 21/13 α (θ=3°) interface. The figure shows a projection across the interface of (a) three overlayers (b) two overlayers and (c) six overlayers of CeO_2 on Al_2O_3. After relaxation, a wave like pattern of both oxygens and ceriums is clearly seen from all three interfaces. The amplitude of the wave appears to diminish on moving from the interface to the surface of ceria suggesting that the wave like pattern is a result of the minimisation optimising the favourable interactions across the interface as opposed to reducing the strain in the system. For all interfaces considered, the figures show that relaxation falls off rapidly away from the interface.

Figure 6.5 Structural representation of the $\Sigma^{p}_{CeO2}/\Sigma^{p}_{Al2O3} = 7/4$ (θ=19.1°) interface after relaxation of CeO_2 (111) monolayer on α-Al_2O_3 (0001) substrate. Oxygen anions of ceria and alumina are coloured red and yellow respectively, ceriums are white and aluminium cations are blue. The upper figure shows a projection viewing across the interface whereas the lower views the ceria overlayer with alumina underneath.

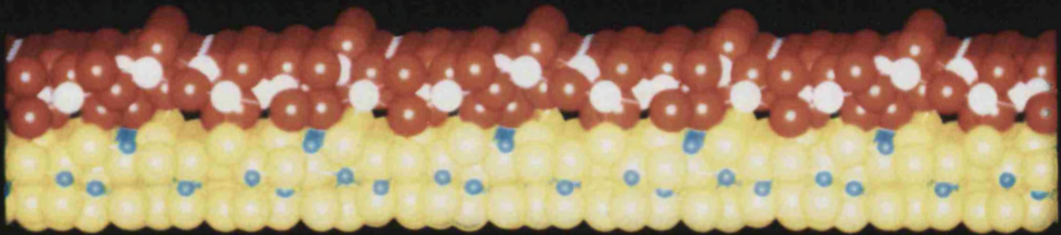

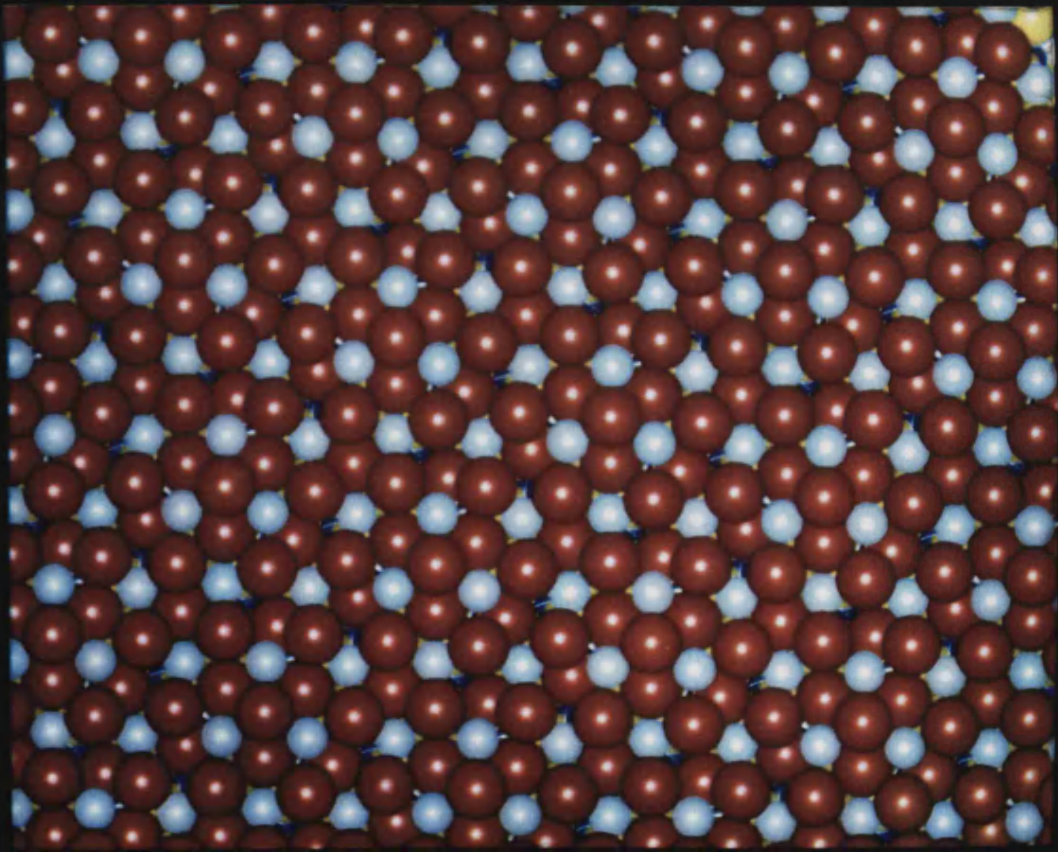

Figure 6.6 Diagrammatic representation of the unrelaxed a) and relaxed b) and c) structures of $\Sigma^p{}_{CeO_2}/\Sigma^p{}_{Al_2O_3}$ = 16/9 (θ=0°) interface, a) and b) viewing across the interface and c) viewing from the CeO_2 (111) monolayer on top of the α-Al_2O_3 (0001) substrate. Oxygens are big circles, ceriums are small light circles and aluminums are small dark circles.

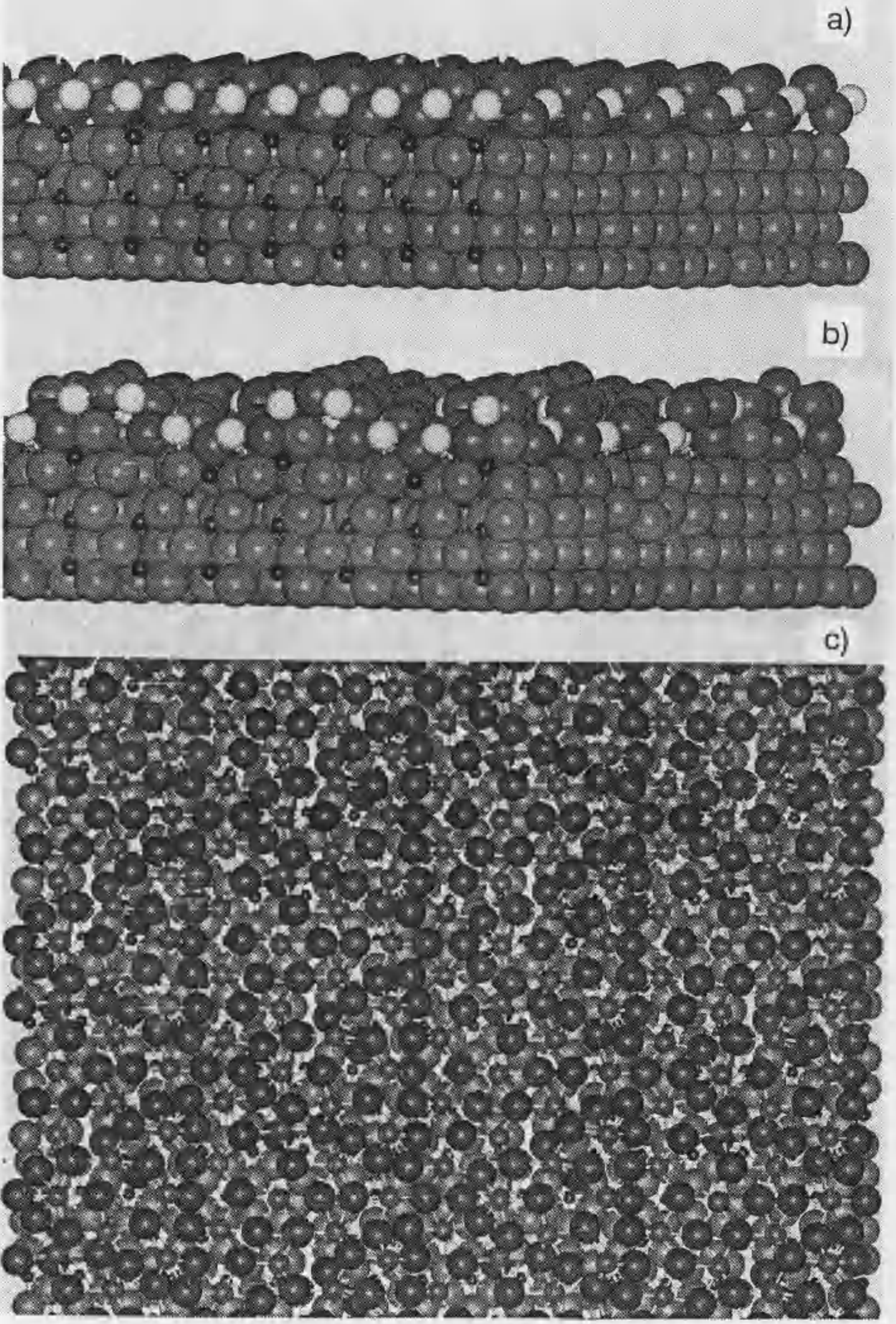
a)
b)
c)

Figure 6.7 Diagrammatic representation of the relaxed structure of $\Sigma^p{CeO_2}/\Sigma^p{Al_2O_3}$ = 12/7 (θ=10.9°) interface, viewing from the CeO_2 (111) monolayer on top of the α-Al_2O_3 (0001) substrate. Oxygen anions of ceria and alumina are coloured red and yellow respectively; ceriums are white and aluminium cations are blue.

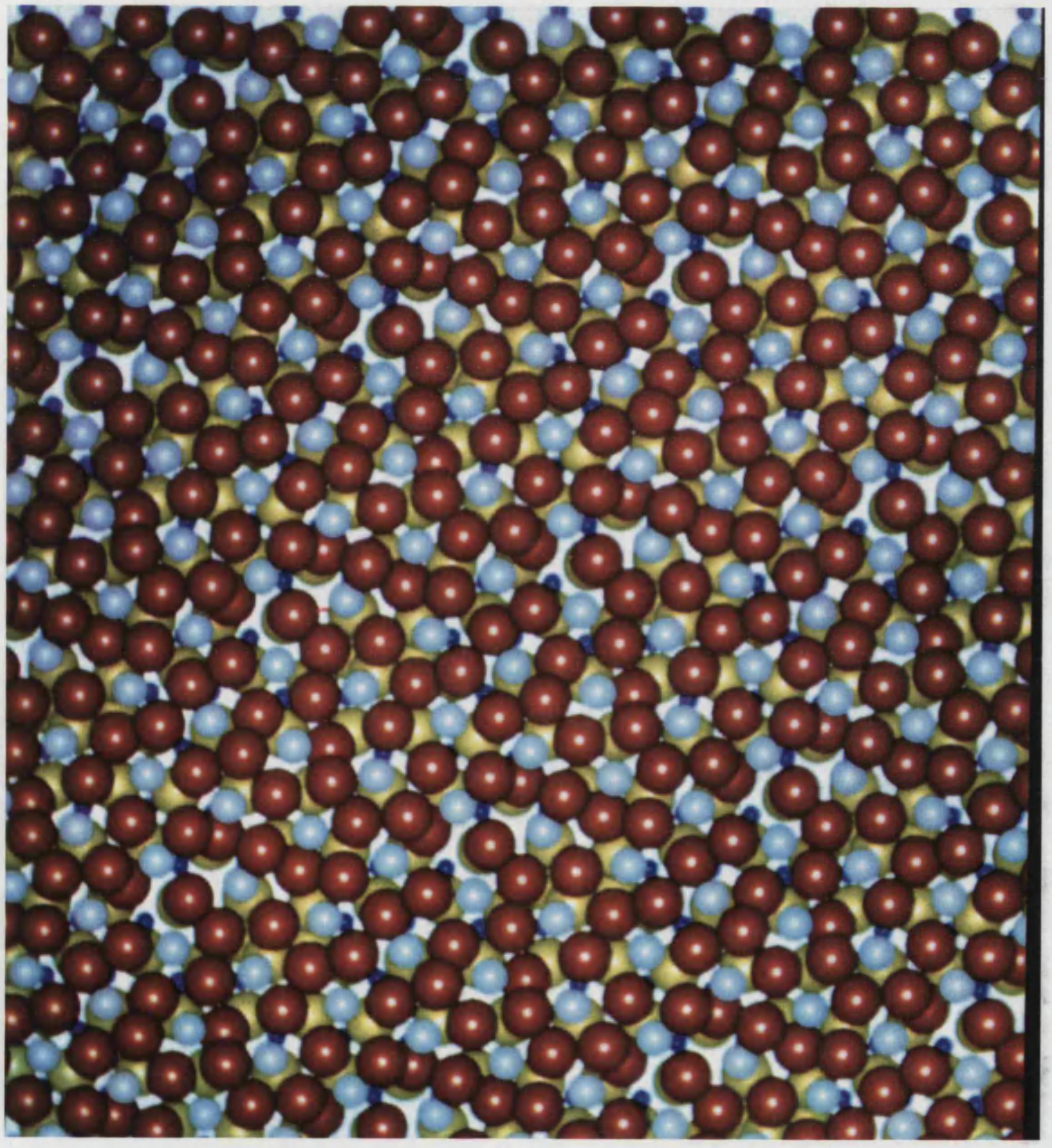

Figure 6.8 Structural representation of the $\Sigma^{p}{}_{CeO2}/\Sigma^{p}{}_{Al2O3} = 21/13$ interface after relaxation of CeO_2 (111) monolayer on α-Al_2O_3 (0001) substrate. Oxygen anions of ceria and alumina are coloured red and yellow respectively, ceriums are white and aluminium cations are blue. The upper figure shows a projection across the interface associated with a rotational angle of ($\theta=3°$) and the lower figure associated with a rotational angle of ($\theta=35.2°$).

Figure 6.9 Structural representation of the $\Sigma^p{}_{CeO_2}/\Sigma^p{}_{Al_2O_3} = 21/13$ ($\theta=3°$) interface after relaxation, viewing across the interface of a) Three layers, b) Two layers and c) six layers of CeO_2 (111) on an α-Al_2O_3 (0001) substrate. Oxygen anions of ceria and alumina are coloured red and yellow respectively, ceriums are white and aluminium cations are blue.

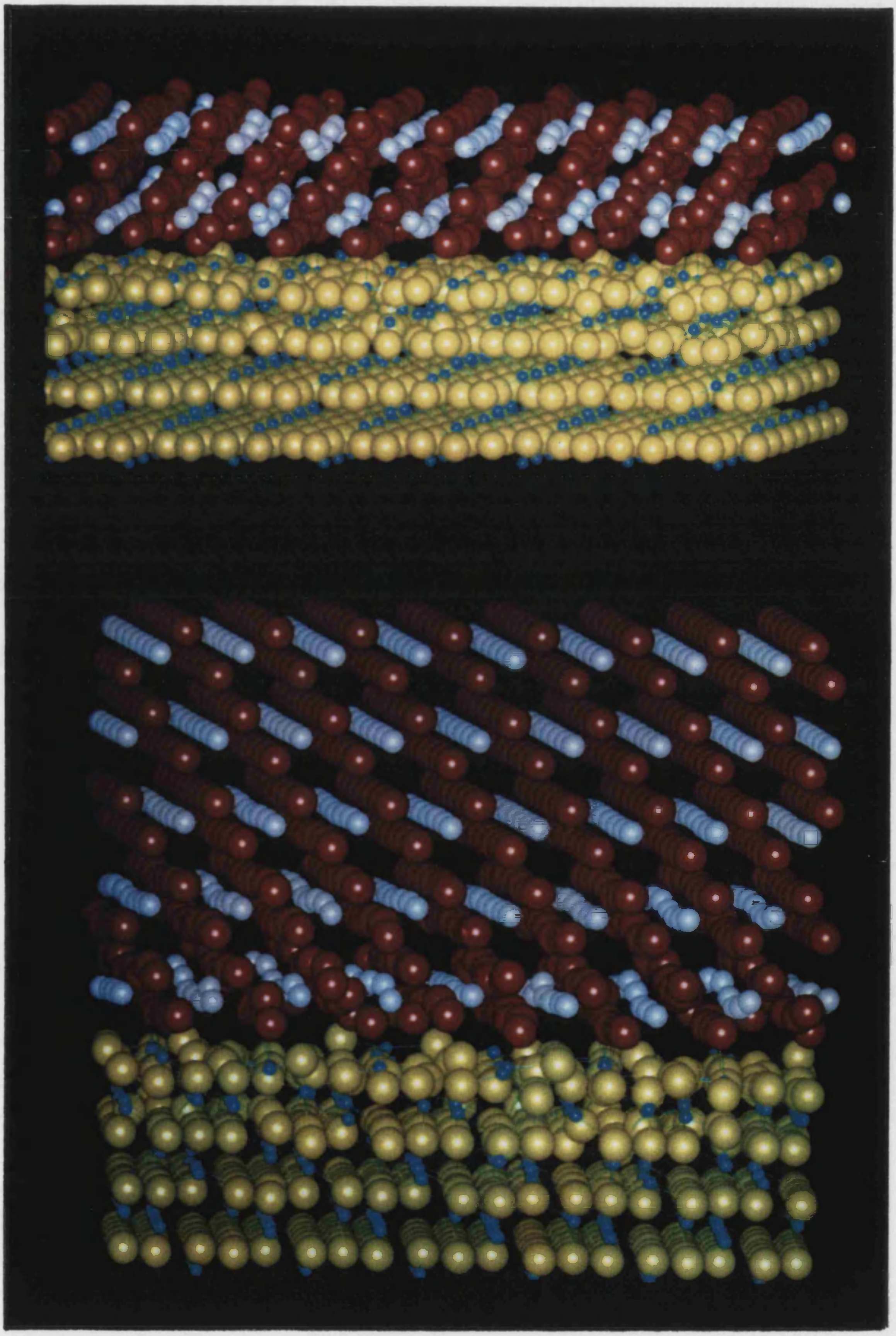

6.5 The Effect of Defect Formation at the Interface

The inclusion of defects is sometimes essential to stabilise an interface such as those between NiO and BaO (Tasker and Stoneham 1987) which include cation vacancies. The present work has shown that the interface between ceria and alumina is very stable, (interfacial stability energies > 1.2 J/m^2). The catalytic activity for oxidation reactions is however dependent on the oxygen activity which is controlled by the oxygen vacancy formation energy.

There is experimental evidence for oxygen migration from ceria to precious metals such as Rh at low temperature found by Zafiris and Gorte (1993). In the study of CO adsorption on Rh/CeO_2 by temperature programmed desorption (TPD), the formation of CO_2 was not affected substantially by the decrease in Rh coverage from five layers to a quarter of monolayer. This suggests that oxygens must migrate from ceria to the Rh surface. Furthermore, the Rh may be partially oxidised. The reduction by Rh of NO which leads to dissociation and N_2 desorption has also been shown to be significantly modified. Zafiris and Gorte (1992) have also found that the interactions between Pt and ceria are relatively weaker. The driving force for migration of oxygen is therefore not a property of ceria alone but is related to the specific metal which is being supported. A comparison can be made with the studies on the desorption of NO on Rh (Altman and Gorte 1988a) and CO on Pt or Rh (Altman and Gorte 1988b) supported on α-Al_2O_3 (0001) without ceria.

Ceria strongly modifies the catalytic properties of these supported catalysts, especially for the $CO + \frac{1}{2} O_2 \rightarrow CO_2$ and $NO + CO \rightarrow \frac{1}{2} N_2 + CO_2$ reactions. These effects were studied for Pt, Rh, (Pt and Rh) supported on CeO_2, Al_2O_3,

(Al_2O_3 and CeO_2), which are shown to be associated with the interaction of highly dispersed noble metals with oxygen vacancies in the reduced ceria support (Lööf et al. 1991 and Oh 1990).

The existence of the interface between ceria and alumina destabilises the ions near the interface region as a result of the unfavourable interactions of like charged ions in near proximity to the two materials. The ceria overlayer therefore becomes a more active surface and possibly a better support for catalytic reactions. Oxygen vacancy formation and migration in ceria play important roles in catalytic reactions. The difference in the oxygen vacancy formation energy in a pure CeO_2 surface compared to a CeO_2 thin film on an Al_2O_3 support may be an indication of the change in catalytic activity resulting from the Al_2O_3 support.

Recently, platinum and palladium were found to form stable interfaces with both aluminium and oxygen faces terminating α-Al_2O_3 (0001) whereas only the aluminium interface is stable with rhodium (Ward 1993). Thus, we only investigate the formation energy of the oxygen vacancy at the interface of the two systems, a) where the charge created by vacancy formation is partially balanced by the reduction of cerium (IV) to cerium (III) and b) by the substitution of cerium (IV) by rhodium (III). The oxygen vacancy is formed first at an interface of a monolayer of ceria (on alumina substrate) which consists of two planes of oxygens, surface plane (1) and interface plane (2); and second, at an interface between three layers of ceria on alumina substrate consist of 6 planes of ceria oxygens, surface plane (1) and interface plane (6) (figure 6.9.a). MIDAS is used to calculate the formation energies of $\approx$14.3% coverage of oxygen vacancies at the interface (E_1) and at the pure/free ceria surface (E_2).

The concentration of the rhodium substitutions at the interface is ≈28.6% of monolayer coverage. The difference between E_1 and E_2 shows the change in the vacancy formation energy due to the interface (figure 6.10). Negative value of (E_1 - E_2) indicates that it is easier to form an oxygen vacancy at the interface with the ceria support.

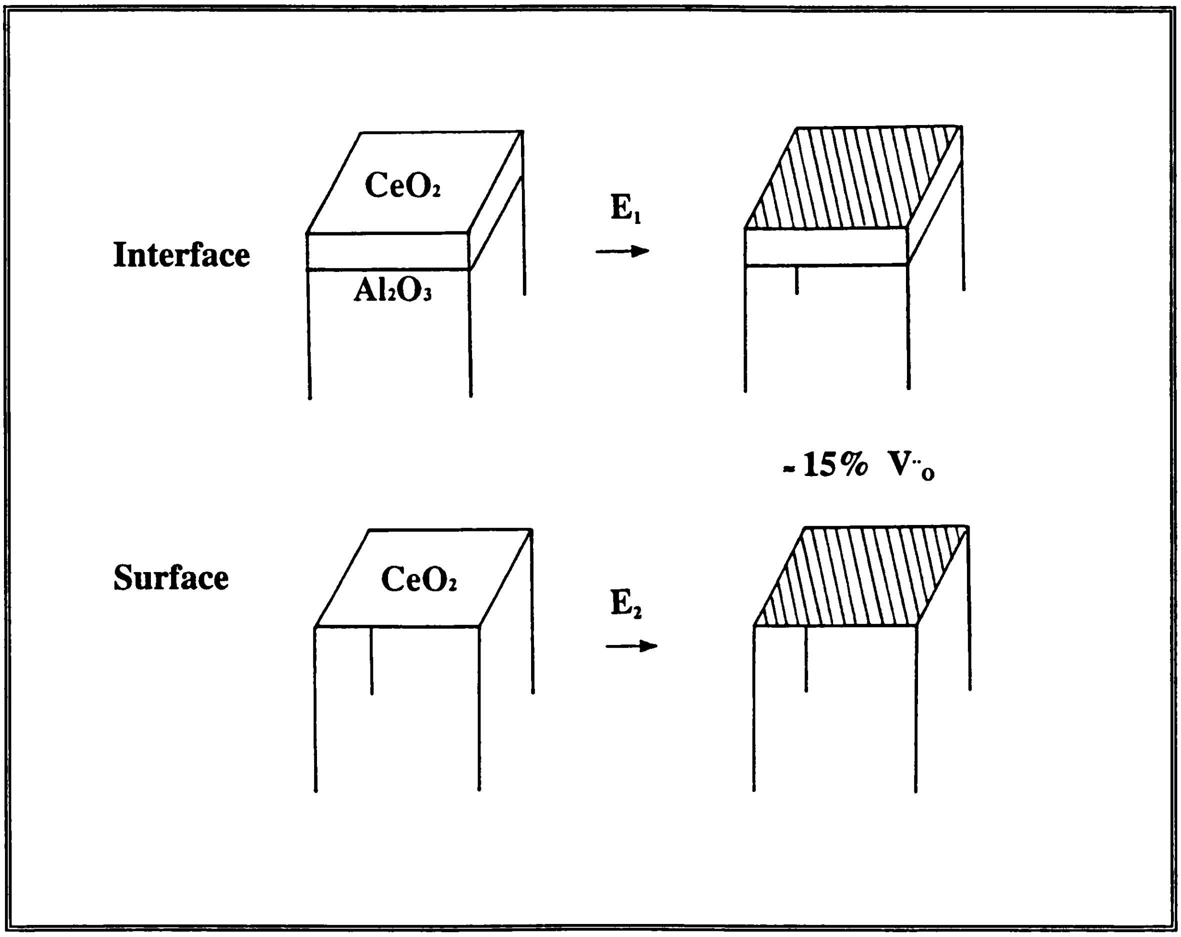

Figure 6.10 Diagrammatic representation of defect formation at the interface of ceria (E_1) compared to those at the pure ceria surface (E_2).

Because of the limited computer resources, only the $\Sigma^{p}{}_{CeO_2}/\Sigma^{p}{}_{Al_2O_3} = 7/4$ (θ= 19.1°) interface with the lowest misfit of -0.06% and smallest primitive unit cell is considered for the study of defects. As noted earlier, the shell model is used to describe the polarisability and the results are presented in table 6.5.

Table 6.5 Defect formation energies (eV) per oxygen vacancy at the interface of ceria supported on alumina (E_1) compared to those at the free/pure surface of ceria (E_2).

Oxygen plane		$[2Ce'_{Ce}\text{-}V^{\bullet\bullet}_{O}]$		$[2Rh'_{Ce}\text{-}V^{\bullet\bullet}_{O}]$		
		E_1	$(E_1 - E_2)$	E_1	$(E_1 - E_2)$	
Surface plane	(1)	83.16	**- 3.34**	80.99	**- 1.73**	1 Layer
Interface plane	(2)	87.97	**+ 1.47**	82.45	**- 0.27**	of Ceria
Surface plane	(1)	86.20	**- 0.30**	81.12	**- 1.60**	3 Layers
Interface plane	(6)	82.37	**- 4.13**	79.26	**- 3.45**	of Ceria
E_2 (pure ceria)		86.50		82.72		

The lattice spacing of ceria varies with the number of layers considered. The oxygen vacancy formation energies will therefore vary with the thickness of the thin ceria films. The values for the oxygen vacancy formation energies are therefore corrected to take account of this. The correction is obtained from the difference in the energies for defect formation at the pure ceria surface using bulk equilibrium and compressed lattice parameters. This correction value also varies for different numbers of ceria overlayers.

There are two main driving forces for defect formation at the interfaces: first, the image charge (Jennings and Jones 1988) will stabilise a charged defects near an interface of higher dielectric constant, (20 for ceria as compared to 11 for alumina), second, the epitaxial constraints may require the formation of vacancies at the interface to obtain a good charge matching and reduce unfavourable interactions e.g. like charge repulsion of ions in near proximity (Tasker et al. 1985). The latter is important for our system whereas the former is not as the overall charge is neutral.

For most systems considered in table 6.5, oxygen formation energies are lower at the interface (E_1) than at the pure ceria surface (E_2), i.e. (E_1-E_2) is negative. This indicates that the interfacial oxygens are far less stable than the pure surface oxygens. The interface between ceria and alumina therefore enhances the formation of the oxygen vacancy making ceria a better oxygen donor source.

For a monolayer of ceria on alumina, the oxygen vacancies are more stable at the surface than at the interface, because oxygens from both layers of the ceria monolayer are more affected by the ionic interactions at the interface. Those at the surface are, however, more accessible than those at the interface. And as discussed earlier, due to a small percentage contraction of ceria to match with alumina substrate initially, after relaxation some oxygens at the surface layer (plane 1) relax outwards to form a partial layer at the surface, which makes the surface oxygens become even more weakly bound than those below.

In contrast, for three layers of the ceria overlayer, oxygen ions at the interfaces (plane 6) are more unstable as a results of possible unfavourable interactions between the two materials. The highly negative values of (E_1-E_2) for the interface plane also indicates that there is a high possibility for oxygen migration to the surface layer during an oxidation reaction in a catalytic process. The surface oxygens in this case are however, far away from the interface and behave similar to those at the pure ceria surface, the energy difference between E_1 and E_2 are therefore smaller for the interface plane.

The reduction of cerium (IV) to cerium (III) has been shown to stabilise the surface oxygen vacancy more effectively than rhodium for a monolayer of ceria, whereas rhodium (III) will enhance the formation of surface oxygens which is independent of the ceria thickness. In summary, the results show that the existence of the interface between ceria and α-alumina increases the stability of surface oxygen vacancies which may make ceria a better oxygen source to oxidation reactions in automobile exhaust catalysts.

6.6 Summary

The work in this chapter has shown that a simple geometrical argument i.e. near coincidence site lattice theory together with the resulting misfit to accommodate epitaxial matching can predict whether an interface is likely to be stable, but the method has very little quantitative predictive power. However, when coupled with the computer simulations, the method has yielded good quantitative information about the interfacial energy, structure and the mechanisms by which the interface is stabilised or destabilised. In particular, we have found that the interfacial stability is heavily dependent on the percentage mismatch. Other factors like the high planar density of coincidence lattice sites across the interface, the associated angle of rotation and ionic relaxation also contribute to the interfacial energy. The relaxational behaviour of the thin film overlayer enables this strain energy to be significantly reduced resulting in a stable interface. For several overlayers on an substrate, however the resulting strain energy from each overlayer will destabilise the interface and the resulting stabilising relaxation is inhibited.

It has been suggested by Balluffi et. al. (1982) that the misfit at the interface is accommodated by the presence of defects or misfit dislocations. Indeed, the defects such as the oxygen vacancy whose formation is accompanied by the reduction of cerium IV to cerium III (or substitutions of metal ions with lower oxidation states) have been shown to stabilise the interface which may assist the oxidation reaction in automobile exhaust catalysis. Further work may elucidate which interfaces (i.e. different alumina planes or indeed different substrates) will enhance or inhibit catalytic activity.

A useful extension to this work would be the examination of the interfaces between a more reactive substrate γ-alumina with the less stable surfaces such as the (110) surface and (310) step surface of ceria which have been shown to be less stable and therefore may stabilise the interfaces even more and hence enhance further the activities of catalysts.

CONCLUSIONS

CONCLUSIONS

Surface and bulk computer simulation techniques have been employed successfully in this thesis to study the crystal properties of ceria, the effects of metal defect inclusion and oxygen vacancy formation and their importance in the reactions in exhaust control catalysis.

The investigation of the pure and defect properties (reported in chapter 4) for both bulk and surfaces of ceria, emphasises the importance of surface oxygen vacancies in ceria. Defect simulations reported in chapter 5 clearly demonstrated that the precious metal ions are extensively segregated to the surfaces of ceria both as isolated ions and neutral clusters. The calculations also predict the formation of coherent second order phases at the (111) surface for palladium and platinum. Further calculations are required to determine the exact composition of these second phases.

The study of the adsorption of the small molecules, CO and NO is only preliminary due the limitations of classical simulation methods. The tendency of dissociation is observed for NO adsorption due to lattice relaxation. A further and more appropriate investigation of this type of work can be done using quantum mechanics.

A major success of this work has undoubtedly been the study of oxygen vacancy formation in pure ceria and at its interface with α-alumina (chapter 4 and 6). Here, the formation energies of the surface oxygen vacancy together with the reduction of cerium has been shown to favour energetically the oxidation of carbon monoxide, which is also evident from experimental work. Further more, when ceria is interfaced with α-alumina, the oxygen vacancy is even more stable and therefore may assist the oxidation reaction in automobile exhaust catalysis more effectively. Chapter 6 also demonstrated that with a simple geometrical argument of near coincidence lattice site theory together with a resulting misfit to accommodate the epitaxial matching, it is possible to predict interface stabilities, structures and the mechanisms by which the interface is stabilised.

To conclude, the work in this thesis has successfully demonstrated that computer simulation techniques can be applied to study structural and defect properties of oxides and their interfaces. Furthermore, the study of interfacial stability between ceria and alumina has opened a door to the investigation of defect properties at the interface between two oxide materials. Future work therefore could be extended to investigate defect properties and the interactions between metals-ceria and γ-aluminium oxide support. Quantum mechanical studies of reaction mechanisms on CeO_2/precious metal surfaces would also be desirable.

REFERENCES

Allan, N.N., Cooper, D.L. and Mackrodt, W.C., Molecular simulation **4**, 269 (1990)

Allas, L.M., J. Phys.Chem. Solids **29**, 91 Pergamon Press (1968)

Altman, E.I. and Gorte, R.J., Surf. Sci. **195**, 392 (1988a)

Altman, E.I. and Gorte, R.J., J. Catal. **113**, 185 (1988b)

Baik, S., Fowler, D.E., Blakely, M and Raj, R., J. Am. Ceram. Soc., **68**, 281 (1985)

Balluffi, R.W., Brokmann, A. and King, A.H., Acta. Metall. **30**, 1453 (1982)

Bertaut, F., Compt. Rendu. **246**, 3447 (1958)

Binet, C., Jadi, A., Lavalley, J.C. and Boutonnet-Kizling, M., J. Chem. Soc. Faraday Trans. **88**, 2079 (1992)

Blochl, P., Das, G.P., Fischmeister, H.F. and Schönberger, U., 'Metal-Ceramic Interfaces', Ed. M. Ruhle, A.G. Evans, M.F. Ashby and J.P. Hirth), Oxford, Pergamon press p9 (1989)

Bollmann, W., Springer, Berlin (1970)

Bondi, A., J. Phys. Chem. **68**, 441 (1964)

Born, M. and Mayer, J.E., J. Chem Phys. **1**, 270 (1933a)

Born, M. and Mayer, J.E., Phys. Rev. **43**, 605 (1933b)

Born, M. and Huang, K., 'Dynamical theory of crystal lattice', Clarendon Press, Oxford (1954)

Boswarva, I.M. and Lidiard, A.B., Phil. Mag. 16, 805 (1967)

Brandon, D.G., Ralph, B., Rangannathan, and Wald, M.S., Acta. Metall. **12**, 813 (1964)

Brauer, G., Gingerich, K.A. and Holtschmidt, U., J. Inorg. Nucl. Chem. **16**, 77 (1960)

Butler, V., Catlow, C.R.A., Fender, B.E.F. and Harding, J.H., Solid state ionics **8**, 109 (1983)

Busing, W.R., Acta. Crystallogr. A **28**, 252 (1970)

Campserveux, J. and Gerdanian, P., J. Chem. Thermodynamics **6**, 795 (1974)

Catlow, C.R.A. and Norgett, M.J., J. Phys. C **6**, 1325 (1973)

Catlow, C.R.A., Proc. Roy. Soc. A **364**, 473 (1977)

Catlow, C.R.A., Norgett, M.J. and Ross, T.A., J. Phys. C **10**, 1627 (1977)

Catlow, C.R.A. and Mackrodt, W.C., 'Computer Simulation of Solids', Ed. C.R.A. Catlow and W.C. Mackrodt, Lecture notes in Physics **166**, 130 (1982)

Catlow, C.R.A,. James, R., Mackrodt, W.C. and Stewart, R.F., Phys. Rev. B, **25**, 1006 (1982)

Catlow, C.R.A., Annual Review, Material Science **16**, 517 (1986)

Catlow, C.R.A., Freeman, C.M., Vessal, B., Tomlinson, S. M. and Leslie, M., J. Chem. Soc. Faraday Transactions **81**, 1947 (1991)

Causa, M., Dovesi, R., Pisani, C and Roetti, C., Surf. Sci. **175**, 551 (1986)

Chang, E.K. and Blumenthal, R.N., J. Solid State Chem. **72**, 330 (1988)

Clementi, E. and Roetti, C., Atomic nuclear data tables, **14**, Nos 3-4 (1974)

Clugston, M.J., Advances in Physics **27**, 893 (1978)

Cohen, A.J. and Gordon, R.G., Phys. Rev. B **12**, 3228 (1975)

Cohen, A.J. and Gordon, R.G., Phys. Rev. B, **14**, 4593 (1976)

Colbourn, E.A. and Mackrodt, W.C., Physica **131** B, 41 (1985)

Cormack, A.N., Catlow, C.R.A. and Nowick, A.S., J. Phys. Chem. Solids **50**, 177 (1989)

Cotter, M., Campbell, S., Egdell, R.G. and Mackrodt, W.C., Surf. Sci. **197**, 208 (1988)

Cowan, R.D. and Griffin, D.C., Optical Soc. Amer. **66**, 1010 (1976)

Davidon, W.C., AEC Report, ANL-5990 (Rev) (1959)

Dick, B.G. and Overhauser, A.W., Phys. Rev. **112**, 90 (1958)

Duffy, D.M. and Tasker, P.W., Harwell Report, AERE-TP953 (1982)

Duffy, D.M. and Stoneham, A.M., J. Phys. C **16,** 4087 (1983)

Duffy, D.M. and Tasker, P.W., Harwell Report, AERE-R11059 (1983a)

Duffy, D.M. and Tasker, P.W., Phil. Mag. A. **47**, 817 (1983b)

Duffy, D.M., Hoare, J.P. and Tasker, P.W., J. Phys. C: Solid State Phys. **17**, L195 (1984)

Duffy, D.M., J. Phys. C: Solid State Phys. **19**, 4393 (1986)

Duffy D.M., Harding J.H. and Stoneham A.M., Acta. Metallurgica et Materiala **40** S, 11 (1992)

Duplan, J.L. and Praliaud, H., Appl. Catal. **67**, 325 (1991)

Dwivedi, A. and Cormack, A.N., J. Solid State Chem. **79**, 218 (1989)

Dwivedi, A. and Cormack, A.N., Phil. Mag. A **61**,1 (1990)

East, W., Hand book of Chemistry and Physics, 61st ed. (1985)

Engler, B., Koberstein, E. and Schubert, P., Appl. Catal. **48**, 71 (1989)

Ewald, P.P., Ann. Physik **64**, 253 (1921)

Finnis, M.W., Surface Science **241**, 61 (1991)

Finnis, M.W., Acta. Met. (1992)

Fletcher, R. and Powell, M.J.D., Computer J., **6**, 16 (1963)

Fowler, P.W., Knowles, P.J. and Pyper, N.C., Molecular Physics **56**, 83 (1985)

Fowler, P.W. and Tole, P., Surf. Sci. **197**, 457 (1988)

Freeman, A.J., Li, C. and Fu, C.L., 'Metal-Ceramic Interfaces', Ed. M Ruhle, A.G. Evans, M.F. Ashby and J.P. Hirth, Oxford, Pergamon press p2 (1989)

Gandhi, H.S., Piken, A.G., Shelef, M. and Delosh, R.G., SAE Paper No. 760201, Warrendale, PA (1976)

Gandhi, H.S. and Shelef, M., Studies in Surface Science and Catalysis **30**, 199 (1987)

Gao, Y., Shewmon, P. and Dregia, S.A., Scripta Metallurgica **22**, 1521 (1988)

Geller, S. and Raccah, P.M., Phys. Rev. B **2**, 1167 (1970)

Gillan, M.J. and Dixon, M.J., J. Phys. C **13**, 1901 (1980)

Gordon, R.G. and Kim, Y.S., J. Chem. Phys. **56**, 6, 3122 (1972)

Grimes, R.W., PhD. thesis, University of Keele (1988)

Grimes, R.W., Catlow, C.R.A. and Stoneham, A.M., J. Phys. Condens Matter **1**, 7367 (1989)

Grimes, R.W., Molecular simulation **5**, 9 (1990)

Grimes, R.W. and Catlow, C.R.A., Phil. Trans. R. Soc. Lond. A **335**, 609 (1991)

Grimmer, H., Bollmann, W. and Warrington, D.H., Acta. Cryst. A **30**, 197 (1974)

Hall, R.O.A., Mortimer, M.J. and Mortimer, D.A., Report AERE.-R 11774 (1985)

Harding, J.H., Rep. Prog. Phys. **53**, 1403 (1990)

Harding, J.H. and Harker, A.H., AERE Harwell R10425 (1982)

Harding, J.H. and Harker, A.H., Phyl. Mag. B **51**, 119 (1985)

Harker, A., PhD. thesis, Oxford University (1974)

Harrison, B., Diwell, A.F. and Hallett, C., Platinum Metals Rev. **32**, 73 (1988)

Harrison, W.A. and Sokel, R., J. Chem Phys. **65**, 379 (1976)

Henrich, V.E., Rep. Prog. Phys. **48**, 1481 (1985)

Herman, F. and Skillman, S., Atomic Structure calculations, New Jersy:Prentice - Hall, (1963)

Herrmann, J.M., J. Catal. **89**, 404 (1984)

Herzberg, G., Molecular Spectra, Molecular Structure, Vol 1, 1950

Heyes, D.M., Barber, M. and Clarke, J.H.R., J. Chem Soc., Farad. Trans. II **10**, 1485 (1977)

Hicks, R.F., Rigano, C. and Pang, B., Catalysis letters **6**, 271 (1990)

Hirshfelder, J.O., Cuttiss, C.F. and Bird, R.B., 'Molecular Theory of Gases and Liquids', John Wiley and Sons, New York; Chapman and Hall, London (1954)

Horsley J.A., J. Amer Chem. Soc. **101**, 2870 (1979)

Hwang, D.M., Ravi, T.S., Ramesh, R., Chan, S.-W., Chen, C.Y., Nazar, L., Wu, X.D., Inam, A. and Venkatesan, T., Appl. Phys. Lett. **57**, 1690 (1990)

Islam. M.S. and Ananthamoham, C., Phys. Rev. B **44**, 9492 (1991)

Jennings, P.W. and Jones, R.O., Advances in Physics **37**, 341 (1988)

Jin, T., Okuhara, T., Mains, G.J. and White, J.M., J. Phys. Chem. **91**, 3310 (1987)

Keeton, S.C. and Wilson, W.D., Phys. Rev. B **7**, 834 (1973)

Kenway, P.R., Parker, S.C. and Marckrodt, W.C., Molecular simulation **4**, 175 (1989)

Kenway, P.R., Oliver, O.M., Parker, S.C., Sayle, D.C., Sayle, T.X.T. and Titiloye, J.O., Molecular Simulation **9**, 83 (1992)

Kieselev, A.V., Lopatkin, A.A. and Slulga, A.A., Laboratory of Adsorption and Chromatography, Chemical Department of the Moscow Lomonosov State University, Moscow, USSR (1984)

Kim, Y.S. and Gordon, R.G., Phys. Rev. B **9**, 3548 (1974)

King, D.A., Department of Chemistry, University of Cambridge, 'Polar solids meeting', (1993)

Kummer, J.T. and Yao, Y.Y., Can J. Chem. **45**, 421 (1967)

La, H.B., J. Phys. C:Solid St. Phys. **13**, 3969, (1980)

Lawrence, P.J., PhD. thesis, Bath university (1988)

Leslie, M., SERC Daresbury Report, DL/SCI/TM31T, SERC Daresbury Laboratory (1982)

Levin, J.D. and Mark,P., Phys. Rev., **144**, 751 (1966)

Lewis, G.V. and Catlow, C.R.A., J. Phys. C, Solid state phys. **18**, 1149 (1985)

Li, C., Arai, T., Domen, K., Maruya, K. and Onishi, T., J. Chem. Soc., Chem. Commun., 410 (1991)

Lidiard, A.B. and Norgett, M.J., 'Computational Solid State Physics', Eds. Hermann, F., Dalton, N.W. , and Koehler, T.R. (Plenu) NewYork, 385 (1972)

Lööf, P., Kasemo, B. Andersson, S. and Frestad, A., J. Catal. **130**, 181 (1991)

Mackrodt, W.C., Adv. Ceram. **23**, 293, Eds. Catlow and Mackrodt, The American Ceramic Society, Columbus, Ohio, (1987)

Mackrodt, W.C. Davey, R.J., Black, S.N. and Docherty, R., J. of Crystal Growth **80**, 441 (1987)

Mackrodt, W.C. and Stewart, R.F., J. Phys. C: Solid State Phys. **10**, 1431 (1977)

Mackrodt, W.C. and Stewart, R.F., J. Phys. C: Solid State Phys. **12**, 431 (1979)

Mackrodt, W.C. and Tasker, P.W., Mat. Res. Symp. Proc. **60**, 291 (1986)

Mackrodt, W.C. and Tasker, P.W., J. Am. Ceram. Soc. **72**, 1576 (1989)

Masri, P., Tasker, P.W., Hoare, J.P. and Harding, J.H., Surf.Sci. **173**, 439 (1986)

Metcalfe, I.S and Sundaresan, S., Chem. Eng. Sci. **41**, 1109 (1986)

Mott, N.F. and Littleton, M.J., Trans. Faraday Soc. **34**, 485 (1938)

Mykura, H., Bansal, P.S. and Lewis, M.H., Phil. Mag. A **42**, 225 (1980)

Normand, F., Hilaire, L., Kili, K., Krill, G. and Maire, G., J. Phys. Chem. **92**, 2561 (1988)

Norgett, M.J., Harwell Report AERE-R7015 (1972)

Norgett, M.J., Harwell Report AERE-R7650 (1974)

Oh, Se H., J. Catal. **124**, 477 (1990)

Oh, Se H. and Eickel C.C., J Catal. **112**, 543 (1988)

Parker, S.C. and Price, G.D., NATO A.S.I. Series C, 225, 591, Ed. E.K.H. Salje, D. Reidel Publ. Company, Dordrecht (1988)

Parry, D.E, Surf. Sci. **49**, 433 (1975a)

Parry, D.E, Surf. Sci. **54**, 195 (1975b)

Pauling, L., 'General Chemistry', San Francisco, Freemen and Co. (1958)

Resasco, D.E. and Haller, G.L., J. Catal. **82**, 279 (1983)

Samsonov, G.V. , Oxide handbook, IFI/PLENUM, NY (1982)

Sanders, M.J, Leslie, M. and Catlow, C.R.A., J. Chem. Soc., Chem. Comm., 1273 (1984)

Sanchez, M.G. and Garquez, J.L., J. Catal. **104**, 120 (1987)

Sayle, D.C., Ph.D. Thesis, Bath University 1992

Sayle, T.X.T., Catlow C.R.A., Sayle, D.C., Parker, S.C. and Harding J.H., Phil. Mag. A, in press (1993)

Schonberger, U., Andersen, O.K. and Methfessel, M., Acta Met. 40 S, 1 (1992)

Shyu, J.Z., Webber, W.H. and Gandhi, H.S., J.Phys. Chem. **92**, 4964 (1988a)

Shyu, J.Z., Otto, K., Watkins, W.L.H., Graham, G.W., Belitz, R.K. and Gandhi, H.S., J. Catal. **114**, 23 (1988b)

Shyu, J.Z. and Otto, K., J. Catal. **115**, 16 (1989)

Slater, J.C. and Kirkwood, J.G., Phys. Rev. **37**, 682 (1931)

Smith, D.A. and Pond, R.C., Int. Metall. Rev. **205**, 61 (1976)

Stoneham, A.M. and Tasker, P.W., Phil. Mag. B **55** 237 (1987)

Su, E.C., Montreuil, C.N. and Rothschild, W.G., Appl. Catal. **17**, 75 (1985)

Su, E.C. and Rothschild, W.G., J. Catal. **99**, 506 (1986)

Su, H.T., Wang, R., Fuchs, H., Gardner, J.A., Evenson, W.E. and Sommers, J.A., J. Am. Ceram. Soc. **73**, 3215 (1990)

Summers, J.C. and Ausen, S.A., J. Catal. **58**, 131 (1979)

Sun, C.P. and Balluffi, R.W., Phil. Mag. A **46**, 49 (1982)

Sun, C.P. and Balluffi, R.W., Phil. Mag. A **46**, 63 (1982)

Sutton, A.P. and Balluffi, R.W., Acta. Metall. **35**, 2177 (1987)

Tasker, P.W., Harwell Report, AERE-R9130 (1978)

Tasker, P.W., Phil. Mag. A **39**, 119 (1979a)

Tasker, P.W., J. Phys. C: Solid State Phys. **12**, 4977 (1979b)

Tasker, P.W., Colbourn, E.A. and Mackrodt, W.C., J. Am. Ceram. Soc. **68**, 74 (1985)

Tasker, P.W. and Stoneham, A.M., Journal de Chimie Physique **84**, 149 (1987)

Tétot, R., Picard, C., Boureau, G. and Gerdanian, P., 'Nonstoichiometric compounds', Advance in Ceramics **23**, 457, ed. by C.R.A. Catlow and W.C. Mackrodt (1987)

Titiloye, J.O., Parker, S.C., Sayle, D.C. and Stone F.S., Studies in Surface Science and Catalysis **52**, 271 (1989)

Trovarelli, A., Dolcetti, G., Carla de Leitenburg, Kaspar, J., Finetti, P. and Santoni, A., J. Chem Soc. Faraday Trans. **88**, 1311 (1992)

Tschaufeser, P, PhD. Thesis, University of Bath (1988)

Wang, S.Y., Moon, S.H. and Vannice, M.A., J.Catal. **71**, 167 (1981)

Ward, T.R., Pere Alemany and Roald Hoffmann, Department of Chemistry and Materials Science Center, Cornell University, Ithaca NY 14853-1301, Abstract, Division of Catalysis and Surface Science Secretariat (1993)

Watson, G.W., Parker, S.C. and Wall, A., J. Phys. Condensed Matter **4**, 2097 (1992)

Vereshtshagin, A.N., 'Paljarizuemost molecul', Moscow, Nauka (1980)

Wedepohl, P.T., Proc. Phys. Soc., London **92**, 79 (1967)

Wedepohl, P.T., J. Phys. C **10**, 1855 (1977a)

Wedepohl, P.T., J. Phys. C **10**, 1865 (1977b)

Wolf, D. and Benedek, R., Adv. Ceram., 1, 107 (1981)

Wolf, D., J. Physica **131** B, 53 (1982)

Woods, A.B., Cochran, W. and Brockhouse, B.N., Phys. Rev. B **119**, 980 (1960)

Wood C.P. and Pyper N.C., Molec. Phys. **43**, 1376 (1981)

Wyckoff, R.W.G., 'Crystal structure' 2nd ed., Vol 2 (1967)

Yao, H.C., Japar, S. and Shelef, M., J. Catal. **50**, 407 (1977)

Yao, H.C. and Yu Yao, Y.F., J Catal. **86,** 254 (1984)

Yu Yao, Y.F., J. Catal. **87** 152 (1984)

Yu Yao, Y.F. and Kummer, J.T., J. Catal. **106**, 307 (1987)

Zafiris, G.S. and Gorte, R.J., Surf. Sci. **276**, 86 (1992)

Zafiris, G.S. and Gorte, R.J., J. Catal. **139**, 561 (1993)

APPENDIX

Appendix 1

A1.1 Ewald method - Summation of the 3-Dimensional Coulombic Terms

As noted in section 2.5, the calculation of the lattice energies of the systems investigated in this thesis include contributions from pair potential energy terms only. The total potential energy of the lattice $U(r_{ij})$ is given by:

$$U(r_{ij}) = \sum_{i,j=1}^{N} \frac{q_i\, q_j}{4\pi\varepsilon_o r_{ij}} + \sum_{i,j=1}^{N} \Phi(r_{ij}) \qquad \text{(A1.1)}$$

The first term in equation (A1.1) is the long range Coulombic interaction which accounts for about 80% of the lattice energy. The summation o the $1/r$ term is very slowly converging in real space. However, its convergence acn be greatly accelerated by using the Ewald summation technique (Ewald 1921), the basis of which is the fact that $^1/r$ can be expressed in integral form:

$$\frac{1}{r} = \frac{2}{\pi^{1/2}}\left\{\int_0^{\eta} \exp(-r^2t^2)dt + \int_{\eta}^{\infty} \exp(-r^2t^2)dt\right\} \quad , \qquad \text{(A1.2)}$$

where t and η are variables, chosen to optimise the speed of convergence of the system. The first integral term (I_1) of equation (A1.2) can be transformed into reciprocal space by Fourier analysis:

$$I_1 = \frac{2}{\pi^{1/2}} \int_0^{\eta} \exp(-r^2t^2)dt = \frac{4\pi}{V} \sum_{\underline{G}} \frac{1}{G^2} \exp\left(\frac{-G^2}{4\eta}\right) . \exp(-i\,\underline{G}.\underline{r}) \qquad \text{(A1.3)}$$

where G is the reciprocal lattice vector and V, the volume of the unit cell. The second integral term in equation (A1.2) can be evaluated in real space:

$$I_2 = \frac{2}{\pi^{1/2}} \int_{\eta}^{\infty} \exp(-r^2 t^2) dt = \frac{1}{r} \operatorname{erfc}(\eta r) \qquad \text{(A1.4)}$$

where erfc(r) is the complimentary error function and is related to the standard error function by:

$$\operatorname{erfc}(\underline{r}) = 1 - \operatorname{erf}(\underline{r}) \qquad \text{(A1.5)}$$

The total Coulombic contribution to the lattice energy therefore becomes:

$$\sum_{ij} \frac{q_i q_j}{r_{ij}} = \frac{4r}{V} \sum_{\underline{G}} \frac{\exp\left(\frac{-G^2}{4\eta}\right)}{G^2} \sum_{ij} q_i q_j \exp(-i\underline{G}.\underline{r}_{ij}) + \sum_{ij} q_i q_j \frac{\operatorname{erfc}(r_{ij}\eta)}{r_{ij}} \qquad \text{(A1.6)}$$

The summation is now rapidly convergent with increasing G and r.

Appendix 2

Parry method - Summation of the 2-Dimensional Coulomb Terms

The treatment of the Coulombic terms in a two-dimensional lattice is calculated by an analogous method, first considered by Parry (1975a, 1975b). The identity $^1/r$ is again split into two parts - a real space summation and a reciprocal summation. The real space contribution, I_2 is given by equation (A1.4) without the self interaction term. The reciprocal space summation is different from the three-dimensional case as there remains a $\underline{G} = 0$ contribution. In the three-dimensional case, this term disappears because of the charge neutrality of the unit cell. At surfaces the contribution from the Coulombic terms are summed on each plane of the crystal and unless the planes are charge neutral, the $\underline{G} = 0$ term must be included. Furthermore the surface relaxation causes a rumpling effect in the surface ions and therefore induces a dipole perpendicular to the surfaces of crystals with charge neutral planes such as MgO (100) and CeO_2 (110). The reciprocal lattice contribution to the Coulomb energy is given by:

$$I_1 = \frac{\pi}{A}\left(-2\underline{u}_{ij}\,\mathrm{erf}(\eta\underline{u}_{ij}) - \frac{2\exp(-\eta\underline{u}_{ij})}{\eta\pi^{1/2}}\right) + \frac{\pi}{A}\sum_{\underline{G}\neq 0}\frac{1}{\underline{G}}(B+C)\exp(i\,\underline{G}.\underline{p}_{ij}) \qquad \text{(A1.7)}$$

Where A : is the area of the unit cell,

$\underline{G}$: is the reciprocal lattice vector

$$B = \exp(\underline{G}.\underline{u}_{ij})\ \mathrm{erfc}\,[(\underline{G}/2\eta) + (\eta\underline{u}_{ij})] \qquad \text{(A1.8)}$$

$$C = \exp(-\underline{G}.\underline{u}_{ij})\,\mathrm{erfc}\,[(\underline{G}/2\eta) - (\eta\underline{u}_{ij})] \qquad \text{(A1.9)}$$

$\underline{r}_{ij}$ is resolved into two components, $\underline{u}_{ij}$ perpendicular to the interface and p_{ij} in the interfacial plane. $2\eta/\pi^{1/2}$ is subtracted from equation (A1.7) to remove the self interaction term and the infinite sums are truncated when a suitable accuracy criterion is met.

Appendix 2

Table A2.1 Variation of oxygen vacancy formation energy as a function of region I size (figure 2.2.a in section 2.2.1)

Size of Region I (l.u.)	**Defect Energy** (eV)
1.5	17.050
1.9	16.955
2.9	16.870
3.2	16.550
3.4	16.510
3.9	16.505
4.5	16.500
5.0	16.495
6.0	16.490
7.0	16.490
8.0	16.490

Table A2.2

Variation of oxygen vacancy formation energy as a function of cut-off potential (figure 2.2.b in section 2.2.1)

Cut-off Potential (l.u.)	**Defect Energy** (eV)
1.0	16.461
1.5	16.485
2.0	16.513
2.5	16.533
3.0	16.537
3.5	16.540
4.0	16.542
4.5	16.544
5.5	16.545

Appendix 3

As noted in section 3.7, the parameters of the analytic Hartree-Fock wave functions for the O^{2-} ion in stabilising potential wells of various depths , V_O Hartrees, are tabulated in table A.3.1

Table A3.1

	1	n	Z	$V_O = 0.5$	$V_O = 1.0$	$V_O = 1.5$	$V_O = 2.0$
1s	0	0	7.6126	0.937176	0.937045	0.936965	0.936919
	0	0	13.3654	0.039048	0.039072	0.039082	0.039079
	0	1	3.2045	0.001712	0.001905	0.002062	0.002210
	0	1	6.2896	0.035237	0.035281	0.035296	0.035287
	0	1	1.7637	0.000653	0.000640	0.000621	0.000596
	0	1	0.5000	0.000015	0.000005	-0.000001	-0.000004
2s	0	0	7.6126	-0.215935	-0.217381	-0.218042	-0.218314
	0	0	13.3654	-0.002048	-0.000320	0.000703	0.001390
	0	1	3.2045	0.455608	0.428414	0.410342	0.396730
	0	1	6.2896	-0.094891	-0.086133	-0.080641	-0.076723
	0	1	1.7637	0.662592	0.687018	0.703721	0.716363
	0	1	0.5000	0.024465	0.013570	0.005028	-0.001543
2p	1	1	1.7424	0.442193	0.479299	0.534144	0.586367
	1	1	3.4363	0.281250	0.268794	0.251841	0.235945
	1	1	0.8565	0.432905	0.453384	0.407721	0.353612
	1	1	0.4700	-0.017573	-0.107260	-0.118883	-0.113412
	1	1	7.8070	0.012479	0.014921	0.017767	0.020356

Table A3.2 Eigenvalues of O^{2-} in stabilising wells: total energies expectation values of stabilising potential <V> in Hartree units.

V_0	State	Eigen value	< V >
0.5	1s	-20.2499	-0.5000
	2s	- 0.8974	-0.4978
	2p	- 0.1775	-0.4811
	Total	-79.3053	
1.0	1s	-20.6360	-1.0000
	2s	- 1.3228	-0.9960
	2p	- 0.6064	-0.9728
	Total	-84.2064	
1.5	1s	-21.0562	-1.5000
	2s	- 1.7726	-1.4993
	2p	- 1.0563	-1.4669
	Total	-89.1299	
2.0	1s	-21.4907	-2.0000
	2s	- 2.2318	-1.9926
	2p	- 1.5152	-1.9632
	Total	-94.0645	

Appendix 4

Table A4 The variation of oxygen vacancy formation energy as a function of distance from surfaces of ceria (figure 4.5 in section 4.3.1)

r (Å)	Defect Energy (eV) **(111)**	**(110)**
1.98		14.275
2.28	13.626	
3.14	14.513	
3.51		14.381
5.13	15.750	
5.70		15.700
6.78	16.006	
7.54		16.295
8.43	15.573	
9.52		15.798
10.01	15.647	
11.58	15.730	
13.18	15.686	
14.17	15.519	

Appendix 5

Table A5.1 Defect formation energy as a function of distance from the (111) and (110) surfaces of ceria (figure 5.2 in section 5.6)

r	**Defect Formation Energy** (eV)				
(Å)	**Ce^{3+}**	**Rh^{3+}**	**Pd^{2+}**	**Pt^{2+}**	
3.120	35.224	33.593	58.938	59.251	(111) Surface
6.239	26.784	34.310	61.487	62.674	
9.367	37.032	34.472	61.904	63.172	
12.489	37.024	34.460	61.846	63.116	
15.614	37.019	34.452	61.819	63.093	
24.988	36.992	34.427	61.714	62.986	
2.156	34.178	32.676	56.952	57.458	(110) Surface
3.528	35.808	33.337	60.101	61.221	
7.527	36.600	34.058	61.287	62.536	
9.636	36.970	34.405	61.723	62.995	
11.420	36.956	34.419	61.717	62.973	
17.234	37.007	34.439	61.762	63.037	
21.052	36.990	34.426	61.703	62.973	

Table **A5.2** Segregation energy as a function of coverage for the (111) and the (110) surfaces of ceria (figures 5.3 and 5.5 in section 5.7).

% Coverage	Segregation Energy (eV)					Surface
	Ce^{3+}	**Rh^{3+}**	**Pd^{2+}**	**Pt^{2+}**	**Ce^{3+}/Al^{3+}**	
1.00	-1.094	-0.880	-2.576	-3.702	-5.422	(111)
0.75	-1.131	-1.031	-3.790	-4.149	-5.315	
0.50	-1.273	-0.759	-4.567	-2.994	-4.830	
0.25	-1.813	-1.129	-3.680	-4.275	-4.926	
0.00	-1.934	-0.943	-2.047	-3.342	-3.825	
1.00	-1.346	-0.404	-4.791	-2.558	-6.127	(110)
0.75	-1.624	-1.175	-4.311	-5.195	-5.725	
0.50	-1.773	-1.585	-4.824	-5.598	-6.662	
0.25	-2.392	-1.750	-5.863	-5.913	-6.767	
0.00	-3.524	-2.260	-5.779	-6.514	-6.140	

Table A5.3

Calculated equilibrium surface coverage of neutral defects at the the (111) and (110) surfaces of ceria (figure 5.6 in section 5.7)

Temperature (K)	Surface Coverage (X_s)		
	Pd^{2+}	**Rh^{3+}**	
	(111)	(111)	(110)
	X_b = 200ppm	145ppm	145ppm
2500	0.636	0.675	0.168
2250	0.646	0.711	0.218
2000	0.656	0.737	0.402
1750	0.667	0.758	0.468
1500	0.677	0.777	0.508
1250	0.691	0.798	0.543
1000	0.703	0.818	0.573
900	0.708	0.826	0.583
750		0.838	0.598
650		0.847	0.611
600		0.857	0.617
500		0.863	0.628

Appendix 6

Variation of surface formation energy with lattice parameters of ceria

(figure 6.3 in section 6.4.2)

Table A6.1

Monolayer of CeO_2

r (Å)	Energy (eV)
2.4055	-102.1020
2.4500	-102.7745
2.5000	-103.2547
2.5250	-103.3976
2.5432	-103.4640
2.5770	-103.5120
2.5900	-103.5050
2.6100	-103.4690
2.6500	-103.3120
2.7055	-102.9270

Table A6.2

Bilayer of CeO_2

r (Å)	Energy (eV)
2.6000	-208.6153
2.6250	-208.7437
2.6300	-208.7815
2.6400	-208.8024
2.6480	-208.8072
2.6500	-208.8069
2.6600	-208.7954
2.6700	-208.7686
2.6850	-208.7005
2.7000	-208.6002

Table A6.3

Three layers of CeO_2

r (Å)	Energy (eV)
2.6485	-314.2964
2.6550	-314.3229
2.6600	-314.3361
2.6650	-314.3431
2.6683	-314.3442
2.6700	-314.3441
2.6750	-314.3391
2.6800	-314.3282
2.6900	-314.2891
2.7000	-314.2276

Table A6.4

Six layers of CeO_2

r (Å)	Energy (eV)
2.6800	-631.1323
2.6850	-631.1446
2.6860	-631.1456
2.6870	-631.1461
2.6875	-631.1462
2.6880	-631.1462
2.6900	-631.1449
2.6950	-631.1332
2.7000	-631.1098